

HELSINKI UNIVERSITY OF TECHNOLOGY  
Department of Electrical and Communications Engineering  
Laboratory of Electromagnetics

**Antti Lamminen**

# **Design of millimetre-wave antennas on low temperature co-fired ceramic substrates**

Master's Thesis submitted in partial fulfillment of the requirements for the degree  
of Master of Science in Technology.

Espoo, January 11, 2006

Supervisor:

Professor Keijo Nikoskinen

Instructor:

Jussi Säily, D.Sc. (Tech.).

<b>Author:</b>	Antti Lamminen	
<b>Name of the Thesis:</b>	Design of millimetre-wave antennas on low temperature co-fired ceramic substrates	
<b>Date:</b>	January 11, 2006	<b>Number of pages:</b> 94
<b>Department:</b>	Department of Electrical and Communications Engineering	
<b>Professorship:</b>	S-96 Electromagnetics	
<b>Supervisor:</b>	Prof. Keijo Nikoskinen	
<b>Instructor:</b>	Jussi Säily, D.Sc. (Tech.)	
<p>In this work, implementation possibilities of millimetre-wave antennas fabricated with low temperature co-fired ceramic (LTCC) technology are investigated. Especially, microstrip antennas operating at 60 GHz frequency band are designed, modeled, manufactured and tested.</p> <p>LTCC is a modern packaging technology which enables manufacturing of multilayer components and modules with high performance up to millimetre-wave region. Benefits of the LTCC technology are high packaging density, low dielectric and conductor losses, reliability and stability. The challenges of the LTCC technology are related to the manufacturing tolerances which become critical for operation of the antennas at 60 GHz frequency band. In the literature review, the basics of antenna theory are presented and common antenna parameters are introduced. Issues related to antenna arrays are also introduced. Then, basic characteristics of microstrip antennas are presented, followed by the introduction of the LTCC technology. Several types of microstrip antennas are designed and modeled with numerical simulation software. Two types of antennas are also modeled with simulation code implemented by the author. The functionality of fabricated antennas is validated by conducting scattering parameter and radiation pattern measurements.</p> <p>Measurement results agree quite well with the simulated ones. Small deviations between simulated and measured results are caused by the differences in designed and realised dimensions of the antennas. Return loss of -10 dB or better is easily achieved. Impedance bandwidth of the antennas is in the order of 3...6%. Maximum absolute gains vary between 3...4 dB. It is clearly seen from the results that functional antennas can be fabricated with standard LTCC process and materials even for the 60 GHz frequency band.</p>		
<b>Keywords:</b> low temperature co-fired ceramic, millimetre-waves, microstrip antennas		

<b>Tekijä:</b>	Antti Lamminen	
<b>Työn nimi:</b>	Millimetriaaltoalueella toimivien antennien suunnittelu ja toteutus monikerroskeraamitekniikalla	
<b>Päivämäärä:</b>	11.1.2006	<b>Sivuja:</b> 94
<b>Osasto:</b>	Sähkö- ja tietoliikennetekniikan osasto	
<b>Professuuri:</b>	S-96 Sähkömagnetiikka	
<b>Työn valvoja:</b>	Prof. Keijo Nikoskinen	
<b>Työn ohjaaja:</b>	TkT Jussi Säily	
<p>Tässä työssä tutkitaan millimetriaaltoalueella toimivien, LTCC- monikerroskeraamitekniikalla valmistettujen, antennien toteutusmahdollisuuksia. Erityisesti keskitytään 60 GHz taajuudella toimivien mikroliuska-antennien suunnitteluun, mallintamiseen, valmistukseen ja testaamiseen.</p> <p>LTCC-tekniikka on nykyaikainen pakkaustekniikka, jolla voidaan valmistaa laadukkaita monikerroksisia komponentteja ja moduuleja jopa millimetriaaltotaajuuksille asti. LTCC-tekniikan hyötyjä ovat suuri pakkaustiheys, matalat eriste- ja johdinhäviöt, luotettavuus ja vakaus. LTCC-tekniikan suurimpia haasteita on valmistusepätkkyys, joka muodostuu ratkaisevaksi tekijäksi 60 GHz taajuudella toimivien antennien suorituskyvylle.</p> <p>Kirjallisuuskatsauksessa esitellään antenniteorian perusteet ja yleisiä antennien ominaisuuksia. Myös antenniryhmän käsitteet esitellään. Tämän jälkeen tarkastellaan mikroliuska-antennien ominaisuuksia, jonka jälkeen perehdytään LTCC-tekniikkaan. Työssä suunnitellaan usean tyyppisiä mikroliuska-antenneja ja antennit mallinnetaan käyttäen kaupallisia ohjelmia. Antenneja simuloidaan myös käyttäen itse kirjoitettua ohjelmakoodia. Antennien toimivuus varmistetaan käytännössä suorittamalla sirontaparametri- ja säteilykuviomittaukset.</p> <p>Mittaus- ja simulointitulokset ovat melko yhteneviä. Pienet poikkeavuudet tuloksissa johtuvat antennien toteutuneiden ja suunniteltujen mittojen eroavaisuuksista. Kuitenkin, paluuvaimennuksen arvoksi saadaan helposti -10 dB tai parempi. Impedanssikaistanleveys vaihtelee välillä 3...6% ja antennien maksimivahvistus välillä 3...4 dB. Tulosten perusteella voidaan todeta, että perinteisen LTCC-tekniikan avulla voidaan toteuttaa toimivia antenneja jopa 60 GHz taajuudelle.</p>		
Avainsanat: LTCC-monikerroskeraamitekniikka, millimetriaallot, mikroliuska-antenni		

# Acknowledgements

This Master's thesis is a part of an international project funded by several sponsors. I would like to thank VTT, TEKES, Filtronic, Finnish Defence Forces, and all the industrial members of the TAFE project for giving me this opportunity to work with such an interesting and challenging task.

I want to thank my instructor, Jussi Säily, for helping me with my work and giving me valuable advices whenever I have asked them. I would also like to thank my supervisor, Professor Keijo Nikoskinen, for guidance and support during the work.

Many thanks go to Hannu Hakojärvi and Ismo Huhtinen for helping with the measurements, to Mikko Kaunisto for producing AutoCAD models of the antennas, to people at VTT Electronics for the LTCC processing, and to co-workers at VTT Information Technology for the supportive atmosphere at daily work.

Finally, I would like to thank my family and friends for the support and encouragements during my studies and especially during this work.

Otaniemi, January 11, 2006

Antti Lamminen



# Contents

<b>Abbreviations</b>	<b>vi</b>
<b>Notations</b>	<b>viii</b>
<b>List of Figures</b>	<b>xii</b>
<b>List of Tables</b>	<b>xiii</b>
<b>1 Introduction</b>	<b>1</b>
1.1 Background . . . . .	1
1.2 Research problem . . . . .	2
1.3 Structure of the work . . . . .	2
<b>2 Antenna Theory</b>	<b>3</b>
2.1 Background of Antennas . . . . .	3
2.2 Antenna radiation . . . . .	4
2.2.1 Maxwell's equations . . . . .	4
2.2.2 Radiated fields of an antenna . . . . .	5
2.2.3 Field regions . . . . .	6
2.3 Basic antenna parameters . . . . .	9
2.3.1 Radiation pattern . . . . .	9
2.3.2 Beamwidth . . . . .	10
2.3.3 Radiation lobes . . . . .	10
2.3.4 Directivity . . . . .	10
2.3.5 Gain . . . . .	11
2.3.6 Polarisation . . . . .	11
2.3.7 Friis transmissison equation . . . . .	12

2.3.8	Input impedance . . . . .	13
2.3.9	Scattering parameters . . . . .	14
2.3.10	Bandwidth . . . . .	15
2.4	Antenna arrays . . . . .	15
2.4.1	Antenna array factor . . . . .	16
2.4.2	Array factor of a linear array . . . . .	16
2.4.3	Array factor of a planar array . . . . .	18
<b>3</b>	<b>Microstrip antennas</b>	<b>21</b>
3.1	Microstrip, dipole and slot antennas . . . . .	21
3.2	Basic characteristics of microstrip antennas . . . . .	22
3.3	Feeding mechanisms of microstrip antennas . . . . .	24
3.4	Design process of microstrip antennas . . . . .	26
3.4.1	The design using the transmission-line model . . . . .	27
3.5	Full-wave modelling of the microstrip antennas . . . . .	28
3.5.1	Method of moments . . . . .	28
3.5.2	Finite element method . . . . .	29
3.5.3	Finite-difference time-domain method . . . . .	30
3.5.4	Comparison between MoM, FEM and FDTD software . . . . .	31
<b>4</b>	<b>LTCC technology</b>	<b>33</b>
4.1	LTCC-what is it? . . . . .	33
4.2	LTCC fabrication process . . . . .	33
4.3	LTCC materials . . . . .	35
4.4	Conductor patterning in LTCC . . . . .	35
4.5	Layer-to-layer alignment, vias and cavities . . . . .	38
4.6	Microstrip antennas on LTCC . . . . .	39
<b>5</b>	<b>Antenna design</b>	<b>42</b>
5.1	Microstrip antenna element . . . . .	42
5.2	Aperture-coupled microstrip patch antenna . . . . .	43
5.2.1	Microstrip line parameters . . . . .	45
5.2.2	Location, size and shape of an aperture . . . . .	47
5.3	Slot-coupled microstrip patch antenna . . . . .	52

5.3.1	Coplanar waveguide parameters . . . . .	53
5.3.2	Location, size and shape of the slot . . . . .	57
5.4	Proximity-coupled microstrip patch antenna . . . . .	60
5.5	Antenna modifications . . . . .	60
5.5.1	Antennas connected to the test fixture . . . . .	60
5.5.2	Calibration standards . . . . .	65
<b>6</b>	<b>Simulations and measurements</b>	<b>67</b>
6.1	Simulations . . . . .	67
6.1.1	IE3D (MoM) . . . . .	67
6.1.2	HFSS (FEM) . . . . .	68
6.1.3	MATLAB code (FDTD) . . . . .	69
6.2	Measurements . . . . .	71
6.2.1	Realised antenna parameters . . . . .	71
6.2.2	S-parameter measurements . . . . .	74
6.2.3	Radiation pattern measurements . . . . .	75
6.3	Results . . . . .	76
6.3.1	S-parameter results . . . . .	78
6.3.2	Radiation pattern results . . . . .	85
<b>7</b>	<b>Conclusions</b>	<b>89</b>
	<b>REFERENCES</b>	<b>92</b>
<b>A</b>	<b>Matlab FDTD code</b>	<b>96</b>

# Abbreviations

ABC	Absorbing boundary condition
AC	Aperture-coupling
ACMPA	Aperture-coupled microstrip line-fed microstrip antenna
AEC	Automatic edge cell
BWRC	Berkeley Wireless Research Center
CMOS	Complementary metal oxide semiconductor
CPU	Central processing unit
CPW	Coplanar waveguide
DE	Differential equation
DFT	Discrete Fourier Transform
EHF	Extreme high frequencies
FDTD	Finite-difference time-domain method
FEM	Finite element method
HUT	Helsinki University of Technology
IE	Integral equation
LHCP	Left-handed circular polarisation
LTCC	Low temperature co-fired ceramic
MoM	Method of Moments

PEC	Perfect electric conductor
PC	Proximity-coupling
PCMPA	Proximity-coupled microstrip line-fed microstrip antenna
PML	Perfectly matched layer
QCBP	Quasi-cavity-backed patch
RCW	Rectangular coaxial waveguide
RHCP	Right-handed circular polarisation
SC	Slot-coupling
SCMPA	Slot-coupled coplanar waveguide-fed microstrip antenna
SCGMPA	Slot-coupled grounded coplanar waveguide-fed microstrip antenna
SCEMPA	Slot-coupled embedded coplanar waveguide-fed microstrip antenna
VTT	Technical Research Centre of Finland
WLAN	Wireless local area network
1D	One-dimensional
3D	Three-dimensional

# Notations

$A_{er}$	Effective area	[m <sup>2</sup> ]
$\mathbf{B}(\mathbf{r})$	Magnetic flux density	[T, Vs/m <sup>2</sup> ]
$BW_{imp}$	Impedance bandwidth	[%]
$bw_{-3dB}$	-3 dB beam width	[°]
$bl$	Backlobe level	[dB]
$\mathbf{D}(\mathbf{r})$	Electric flux density	[As/m <sup>2</sup> ]
$D(\mathbf{u}_r)$	Directivity	
$D_t$	Directivity of the transmitting antenna	
$d$	Distance between transmitting and receiving antennas	[m]
$\mathbf{E}(\mathbf{r})$	Electric field strength	[V/m]
$\mathbf{E}(t)$	Real, time-dependent electric field strength	[V/m]
$\mathbf{E}_i$	Imaginary part of the electric field strength	[V/m]
$\mathbf{E}_r$	Real part of the electric field strength	[V/m]
$f$	Frequency	[Hz, 1/s]
$f_r$	Antenna resonance frequency	[Hz, 1/s]
$f_{op}$	Antenna operating frequency	[Hz, 1/s]
$\overline{\overline{\mathbf{G}}}(\mathbf{r} - \mathbf{r}')$	Green's dyadic	[1/m]
$G(\mathbf{r} - \mathbf{r}')$	Scalar Green's function	[1/m]

$G$	Gain	
$G_t$	Gain of the transmitting antenna	
$G_r$	Gain of the receiving antenna	
$\mathbf{H}(\mathbf{r})$	Magnetic field strength	[A/m]
$h_{cpw}$	Substrate thickness of a coplanar waveguide	[m]
$h_{ms}$	Substrate thickness of a microstrip line	[m]
$h_p$	Substrate thickness of a patch element	[m]
$\bar{\bar{I}}$	Unit dyadic	
$\mathbf{J}(\mathbf{r})$	Electric current density	[A/m <sup>2</sup> ]
$\mathbf{J}_c(\mathbf{r})$	Conducting electric current density	[A/m <sup>2</sup> ]
$\mathbf{J}_s(\mathbf{r})$	Electric current source density	[A/m <sup>2</sup> ]
$\mathbf{J}_{s,m}(\mathbf{r})$	Magnetic current source density	[V/m <sup>2</sup> ]
$k$	Wave number	[rad/m]
$L$	Longest dimension of an antenna element	[m]
$l_{ap}$	Length of an aperture	[m]
$l_{line}$	Length of <i>line</i> calibration standard	[m]
$l_p$	Length of a patch element	[m]
$l_{ref}$	Length of <i>reflect</i> calibration standard	[m]
$l_s$	Length of a matching stub in ACMPA or PCMPA	[m]
$l_{sl}$	Length of a slot	[m]
$l_{st}$	Length of a matching stub in SCMPA, SCGMPA or SCEMPA	[m]
$l_{thru}$	Length of <i>thru</i> calibration standard	[m]
$\mathbf{n}$	Normal unit vector	
$P_t$	Power transmitted from an antenna	[W]

$P_r$	Power received by an antenna	[W]
$\mathbf{r}$	Vector representing field point	
$\mathbf{r}'$	Vector representing source point	
$R_a$	Antenna input resistance	[ $\Omega$ ]
$R_r$	Antenna radiating resistance	[ $\Omega$ ]
$R_l$	Antenna loss resistance	[ $\Omega$ ]
$R_1$	Distance from an antenna at reactive near-field region	[m]
$R_2$	Distance from an antenna at Fresnel region	[m]
$R_3$	Distance from an antenna at Fraunhofer region	[m]
$c_0$	Speed of light in vacuum, $2.998 \cdot 10^8$	[m/s]
$S_{isotr}$	Power density caused by an isotropic radiator	[W/m <sup>2</sup> ]
$S_t$	Power density caused by a transmitting antenna	[W/m <sup>2</sup> ]
$t$	Metallization thickness	[m]
$\tan \delta$	Dielectric loss tangent	
$w(\mathbf{u}_r)$	Radiation density	[W/m <sup>2</sup> ]
$w_{ap}$	Width of an aperture	[m]
$w_g$	Width of a ground plane in ACMPA or PCMPA	[m]
$w_{ms}$	Width of a microstrip line	[m]
$w_p$	Width of a patch element	[m]
$w_{sl}$	Width of a slot	[m]
$w_1$	Width of a coplanar waveguide center strip	[m]
$w_2$	Width of a coplanar waveguide ground strip	[m]
$X_a$	Antenna input reactance	[ $\Omega$ ]
$Z_a$	Antenna input impedance	[ $\Omega$ ]



$\alpha_{cms}$	Conductor loss of a microstrip line	[dB/m]
$\alpha_{dms}$	Dielectric loss factor of a microstrip line	[1/m]
$\alpha_{ccpw}$	Conductor loss of a coplanar waveguide	[dB/m]
$\epsilon$	Permittivity	[As/Vm]
$\epsilon_0$	Permittivity of free space, $8.854 \cdot 10^{-12}$	[As/Vm]
$\epsilon'$	Real part of the permittivity	
$\epsilon_r$	Relative permittivity	
$\eta$	Wave impedance	[ $\Omega$ ]
$\eta_r$	Radiation efficiency	
$\theta$	Elevation angle in spherical coordinates	
$\lambda$	Wavelength	[m]
$\lambda_0$	Wavelength in free space	[m]
$\lambda_d$	Wavelength in a dielectric	[m]
$\mu$	Permeability	[Vs/Am]
$\mu_0$	Permeability of free space, $4\pi \cdot 10^{-7}$	[Vs/Am]
$\mu_r$	Relative permeability	
$\sigma$	Conductivity	[S/m, 1/ $\Omega$ m]
$\phi$	Azimuth angle in spherical coordinates	
$\omega$	Angular frequency	[rad/s]
$\Omega$	Solid angle	
$\nabla$	Gradient operator, "nabla"	

# List of Figures

2.1	Field regions . . . . .	7
2.2	Standard spherical coordinate system . . . . .	9
2.3	Wave polarisations . . . . .	11
2.4	Radio link . . . . .	12
2.5	Linear and planar arrays . . . . .	19
2.6	Array factors for the linear and planar arrays . . . . .	20
3.1	The equivalent source of a microstrip antenna . . . . .	23
3.2	Radiation of a microstrip antenna . . . . .	23
3.3	The feeding mechanisms of the microstrip antennas . . . . .	25
3.4	The effective length of a microstrip antenna . . . . .	28
4.1	The LTCC manufacturing process . . . . .	34
4.2	Screen-printing technique . . . . .	36
4.3	Trampoline screen . . . . .	37
4.4	A cooling channel in the LTCC substrate . . . . .	39
5.1	The effect of patch length on the antenna input impedance . . . . .	44
5.2	The effect of patch width on the antenna input impedance . . . . .	44
5.3	Aperture-coupled microstrip patch antenna . . . . .	45
5.4	Microstrip line . . . . .	46
5.5	Characteristic impedance of a microstrip line . . . . .	46
5.6	Conductor loss of a microstrip line . . . . .	48

5.7	Effect of feed line position on the ACMPA input impedance . . . . .	48
5.8	Transversal electric field distribution of a microstrip line . . . . .	49
5.9	Apertures of various shapes . . . . .	50
5.10	Effect of aperture length on the ACMPA input impedance . . . . .	51
5.11	Effect of stub length on the ACMPA input impedance . . . . .	51
5.12	Slot-coupled microstrip patch antenna . . . . .	53
5.13	Coplanar waveguide . . . . .	53
5.14	Effect of patch position on the SCMPA input impedance . . . . .	54
5.15	QTEM modes of the CPW . . . . .	55
5.16	Theoretical characteristic impedance of the CPW . . . . .	56
5.17	CPW conductor loss . . . . .	57
5.18	Transversal electric field of the symmetrical QTEM mode in the CPW	58
5.19	Effect of slot length on the SCMPA input impedance . . . . .	59
5.20	Effect of stub length on the SCMPA input impedance . . . . .	59
5.21	Effect of aperture width on the PCMPA input impedance . . . . .	61
5.22	Test fixture used in radiation pattern measurements . . . . .	62
5.23	HFSS simulations models of the SCGMPA and SCEMPA . . . . .	64
5.24	HFSS simulation model for PCMPA . . . . .	64
5.25	TRL calibration . . . . .	65
6.1	Magnitudes of the field components of the ACMPA . . . . .	72
6.2	Photograph of SCMPA . . . . .	73
6.3	Photograph of ACMPA . . . . .	73
6.4	S-parameter measurements with the probe station . . . . .	75
6.5	S-parameter measurements for SCGMPA . . . . .	76
6.6	The radiation pattern measurement arrangement . . . . .	77
6.7	E- and H-planes of the microstrip antenna . . . . .	77
6.8	Simulated S-parameter results for ACMPA1 . . . . .	79
6.9	Simulated S-parameter results for the SCMPA1 . . . . .	79

6.10 S-parameter results for the SCMPA1 . . . . .	80
6.11 S-parameter results for the SCMPA2 . . . . .	81
6.12 S-parameter results for the SCMPA3 . . . . .	81
6.13 S-parameter results for the ACMPA1 . . . . .	82
6.14 S-parameter results for the ACMPA2 . . . . .	83
6.15 S-parameter results for the ACMPA3 . . . . .	83
6.16 S-parameter results for the SCGMPA1 . . . . .	84
6.17 Simulated H-plane gain . . . . .	85
6.18 SCGMPA1 E-plane normalised gain . . . . .	87
6.19 SCGMPA1 H-plane normalised gain . . . . .	87

# List of Tables

4.1	Shrinking in the LTCC sintering process. . . . .	35
4.2	Commercial LTCC material data. . . . .	36
4.3	Current status and future trends of LTCC at VTT. . . . .	40
5.1	ACMPA design parameters. . . . .	52
5.2	SCMPA design parameters. . . . .	58
5.3	PCMPA design parameters. . . . .	61
5.4	Design parameters of the SCGMPA and SCEMPA. . . . .	64
5.5	Line lengths of TRL calibration standards . . . . .	66
6.1	Parameters used in FDTD simulations. . . . .	71
6.2	Realised SCMPA parameters. . . . .	74
6.3	Realised ACMPA parameters. . . . .	74
6.4	Impedance characteristics of SCMPA antennas. . . . .	82
6.5	Impedance characteristics of ACMPA antennas. . . . .	84
6.6	Impedance characteristics of the SCGMPA. . . . .	85
6.7	H-plane radiation characteristics. . . . .	86

# Chapter 1

## Introduction

### 1.1 Background

Wide unlicensed frequency band around 60 GHz enables short range communications with high data rates. Recent developments in low temperature co-fired ceramic (LTCC) and complementary metal oxide semiconductor (CMOS) technologies enable cost-effective applications to emerge. This work is a part of the TAFE project in which radio transceiver technology is being studied by VTT in collaboration with Berkeley Wireless Research Center (BRWC). The goal of the project is to develop wireless local area network (WLAN) technology operating at 60 GHz with data speed of 1 Gbit/s.

Recently, there has been a growing interest in exploiting the millimetre-wave frequencies and develop applications for them. The feasibility of a CMOS wireless transceiver capable of 60 GHz operation has been studied by (Doan *et al.*, 2004). In Japan, LTCC technology has been used utilised in development of wireless ethernet link at 60 GHz frequency band operating with data speed 1.25 Gbit/s (Ohata *et al.*, 2002). A LTCC transmitter and receiver for the 60 GHz video transmission system has also been developed (Yamada *et al.*, 2000). A radar module operating even at 77 GHz has been reported (Venot & Wiesbeck, 2003).

A wireless radio link needs antennas for transmitting and receiving electromagnetic waves. Due to poor gain of single antenna elements and high path loss at 60 GHz, antennas have to be placed in a steerable-beam array. In this work, single antennas operating at 60 GHz frequency band are studied. Research will be continued with antenna arrays in near future.

The LTCC technology is well-suited for the planar antenna structures such as slot antennas (Sierra-Garcia & Laurin, 1999), (Bhobe *et al.*, 2004). Microstrip antennas

have also been used in many LTCC applications (Sturzebecher *et al.* , 1996), (Seki *et al.* , 2005), (Huang *et al.* , 2005). The choice of the antenna topology depends on, for example, the antenna environment and integrability to other circuitry.

## 1.2 Research problem

The research problem of this work is to design antennas that can be fabricated using LTCC technology for the 60 GHz frequency band. Antennas are designed in order to have adequate impedance and radiation characteristics at 60 GHz taking into account LTCC manufacturing tolerances and measurement facilities used in testing the functionality of the antennas.

First, the appropriate antenna topology is selected. The choice is based on the possibilities and limitations due to LTCC technology, operating environment of the antenna, and the integrability of the antenna to the active circuits. Then, optimal design parameters are sought using modern commercial numerical modeling tools. For comparison, a code based on finite-difference time-domain method (FDTD) is written by the author. For validation of the design, impedance and radiation characteristics of the antennas are tested in the far-field conditions.

## 1.3 Structure of the work

The Chapter 2 concentrates on the basic antenna theory. Also, the terms used in describing the impedance and radiation characteristics of the antenna are introduced. In Chapter 3, a suitable antenna topology is selected and features of the microstrip antennas are described. The basics of the LTCC technology are introduced in Chapter 4. Detailed description of the design process and parameter study are presented in Chapter 5. In Chapter 6, practical issues related to simulations are brought up. In addition, the FDTD code implemented by the author is depicted and measurement arrangements are shown. The end of Chapter 6 concentrates on the results. Conclusions and considerations about the future work are presented in Chapter 7.

## Chapter 2

# Antenna Theory

Time-harmonic electromagnetic radiation is transversal wave motion which propagates straightforwardly with the speed of light in vacuum. Electromagnetic radiation is called radio waves, visible light, ultraviolet light, X-ray radiation and gamma radiation depending on frequency. Radio waves are subdivided into frequency bands ranging from 3 kHz up to 300 GHz (Räisänen & Lehto, 2001). Millimetre-wave band, also called EHF band, ranges from 30 GHz to 300 GHz. In this work, millimetre-wave antennas operating at 60 GHz frequency are of interest.

### 2.1 Background of Antennas

Electromagnetic waves are usually transferred from one place to another with waveguides or by wireless radio link. Radio link requires antennas. Antenna is defined as "that part of a transmitting or receiving system which is designed to radiate or to receive electromagnetic waves" (IEEE, 1993). Antenna can also be defined as the structure associated with the region of transition between a guided wave and a free-space wave (Kraus, 2002). Antenna is designed to radiate and receive electromagnetic waves in appropriate manner while radiation and receiving phenomenon of other equipment is undesirable.

Antennas can be divided into many categories such as aperture, wire, slot, patch, reflector, lens and traveling-wave antennas (Lindell & Nikoskinen, 1995). Regardless of the shape or the size of the antenna, they are all based on the basic principle that electromagnetic radiation is produced by accelerated or decelerated electric charges. Thus, any alternating current leads to electromagnetic radiation (Sihvola & Lindell, 1996).

First antennas were built by the German Heinrich Hertz in 1886. He built an



end-loaded dipole antenna and a resonant square-loop antenna operating at meter wavelengths. Guglielmo Marconi built a big square conical antenna operating at wavelengths of thousands of meters and he was the first to send a radio signal over the Atlantic in 1901. The advent of radar technology brought the centimetre wavelengths to wide use during World War II and the sizes of the antennas reduced as operating frequency increased. Nowadays antennas are used in satellites, telecommunication, wireless networks, industrial sensors, medical technology and so on.

## 2.2 Antenna radiation

James Clerk Maxwell (1831-1879) presented interactions between electric and magnetic fields in his book *A Treatise on Electricity and Magnetism* (1873). Maxwell's equations predicted the existence of electromagnetic waves before Hertz did his experiments in 1886. Gibbs and Heaviside modified Maxwell's equations later into vector form (Sihvola & Lindell, 1996). Maxwell's equations are compact mathematical expressions of electromagnetic interactions of physical nature.

### 2.2.1 Maxwell's equations

Equations (2.1) and (2.2) represent Maxwell's equations. The first expresses the interaction between electric field strength,  $\mathbf{E}(\mathbf{r}, t)$ , and magnetic flux density,  $\mathbf{B}(\mathbf{r}, t)$ . Interaction between electric current density,  $\mathbf{J}(\mathbf{r}, t)$ , electric flux density,  $\mathbf{D}(\mathbf{r}, t)$ , and magnetic field strength,  $\mathbf{H}(\mathbf{r}, t)$ , is presented in the second equation

$$\nabla \times \mathbf{E}(\mathbf{r}, t) = -\frac{\partial \mathbf{B}(\mathbf{r}, t)}{\partial t}, \quad (2.1)$$

$$\nabla \times \mathbf{H}(\mathbf{r}, t) = \frac{\partial \mathbf{D}(\mathbf{r}, t)}{\partial t} + \mathbf{J}(\mathbf{r}, t). \quad (2.2)$$

The upside-down capital delta symbol,  $\nabla$ , is a gradient operator, "nabla". From now on the current densities are referred to simply as currents. Electric current can be divided into conducting electric current and electric current source  $\mathbf{J}(\mathbf{r}, t) = \mathbf{J}_c(\mathbf{r}, t) + \mathbf{J}_s(\mathbf{r}, t) = \sigma \mathbf{E}(\mathbf{r}, t) + \mathbf{J}_s(\mathbf{r}, t)$ ,  $\sigma$  representing electric conductivity of a medium. Electric and magnetic field strengths depend on the medium with relations  $\mathbf{D}(\mathbf{r}, t) = \epsilon \mathbf{E}(\mathbf{r}, t)$  and  $\mathbf{B}(\mathbf{r}, t) = \mu \mathbf{H}(\mathbf{r}, t)$ , where  $\mu$  represents permeability. Usually the electric and magnetic fields can be regarded as time harmonic i.e. having a sinusoidal time dependence  $e^{j\omega t}$ , where  $\omega = 2\pi f$ ,  $f$  and  $t$  representing the frequency and time instant, respectively. Let us define permittivity,  $\epsilon$ , as complex,  $\epsilon = \epsilon' + \sigma/j\omega$ , where  $\epsilon'$  denotes real part of permittivity and imaginary part is

inversely proportional to angular frequency. To obtain symmetry for the equations (2.1) and (2.2) a magnetic current source,  $\mathbf{J}_{ms}(\mathbf{r}, t)$ , is added into equation (2.1). Magnetic current source is artificial and but it is often useful in calculations. With previous assumptions, equations (2.1) and (2.2) yield

$$\nabla \times \mathbf{E}(\mathbf{r}) = -j\omega\mu\mathbf{H}(\mathbf{r}) - \mathbf{J}_{ms}(\mathbf{r}), \quad (2.3)$$

$$\nabla \times \mathbf{H}(\mathbf{r}) = j\omega\epsilon\mathbf{E}(\mathbf{r}) + \mathbf{J}_s(\mathbf{r}). \quad (2.4)$$

Both  $\mathbf{E}(\mathbf{r})$  and  $\mathbf{H}(\mathbf{r})$  can be complex. Real, time-dependent fields are achieved by multiplying  $\mathbf{E}(\mathbf{r})$  and  $\mathbf{H}(\mathbf{r})$  with  $e^{j\omega t}$  and taking the real part of the complex vectors. For example, for the electric field

$$\mathbf{E}(\mathbf{r}, t) = \Re\{(\mathbf{E}_r(\mathbf{r}) + j\mathbf{E}_i(\mathbf{r}))e^{j\omega t}\} = \mathbf{E}_r(\mathbf{r}) \cos \omega t - \mathbf{E}_i(\mathbf{r}) \sin \omega t, \quad (2.5)$$

where subindices  $r$  and  $i$  denote the real and imaginary parts of the field, respectively. Solving  $\mathbf{E}(\mathbf{r})$  and  $\mathbf{H}(\mathbf{r})$  from equations (2.3) and (2.4), the radiated electromagnetic field produced by  $\mathbf{J}_{ms}(\mathbf{r})$  or  $\mathbf{J}_s(\mathbf{r})$  is found. Radiation analysis of all kinds of antennas is based on equations (2.3) and (2.4).

### 2.2.2 Radiated fields of an antenna

Calculation of the radiated field produced by an electric current source in a free space can be regarded as a basic antenna problem. Antenna can be replaced with a current source,  $\mathbf{J}_{ms}(\mathbf{r})$  or  $\mathbf{J}_s(\mathbf{r})$ , in air if the current distribution in the antenna element is known. However, in many cases the currents are not known and other design methods have to be used. Approximations or numerical simulations can be accomplished in order to obtain the radiated fields produced by an antenna.

Electric current source amplitude depending on its location is abbreviated as  $\mathbf{J}_s(\mathbf{r}')$ . Point at which the field is calculated is expressed with vector  $\mathbf{r}$ . Electric field at point  $\mathbf{r}$  produced by the electric current source,  $\mathbf{J}_s(\mathbf{r}')$ , can be calculated by integrating the electric field produced by infinitesimal electric current sources (Lindell & Nikoskinen, 1995) as

$$\mathbf{E}(\mathbf{r}) = -j\omega\mu \int_V \overline{\overline{\mathbf{G}}}(\mathbf{r} - \mathbf{r}') \cdot \mathbf{J}_s(\mathbf{r}') dV'. \quad (2.6)$$

Green's dyadic,  $\overline{\overline{\mathbf{G}}}(\mathbf{r} - \mathbf{r}')$ , represents a field at point  $\mathbf{r}$  outside the source region produced by unit point source at point  $\mathbf{r}'$ . Green's dyadic can be expressed with

the scalar Green's function,  $G(\mathbf{r} - \mathbf{r}')$ , as

$$\overline{\overline{G}}(\mathbf{r} - \mathbf{r}') = (\overline{\overline{I}} + \frac{1}{k^2} \nabla \nabla) G(\mathbf{r} - \mathbf{r}'), \quad (2.7)$$

where  $\overline{\overline{I}} = \mathbf{u}_r \mathbf{u}_r + \mathbf{u}_\theta \mathbf{u}_\theta + \mathbf{u}_\phi \mathbf{u}_\phi$  is a unit dyadic in spherical coordinates (see Fig.(2.2)) and  $k$  is the wave number. Scalar Green's function can be expressed as

$$G(\mathbf{r} - \mathbf{r}') = \frac{e^{-jk|\mathbf{r} - \mathbf{r}'|}}{4\pi|\mathbf{r} - \mathbf{r}'|}, \quad |\mathbf{r} - \mathbf{r}'| = \sqrt{(\mathbf{r} - \mathbf{r}') \cdot (\mathbf{r} - \mathbf{r}')}. \quad (2.8)$$

A magnetic field can be calculated using equations (2.3) and (2.6)

$$\mathbf{H}(\mathbf{r}) = \int_V [\nabla \times \overline{\overline{G}}(\mathbf{r} - \mathbf{r}')] \cdot \mathbf{J}_s(\mathbf{r}') dV'. \quad (2.9)$$

Similarly, the magnetic and electric fields induced by a magnetic current source can be calculated from the following integrals

$$\mathbf{H}(\mathbf{r}) = -j\omega\epsilon \int_V \overline{\overline{G}}(\mathbf{r} - \mathbf{r}') \cdot \mathbf{J}_{ms}(\mathbf{r}') dV', \quad (2.10)$$

$$\mathbf{E}(\mathbf{r}) = - \int_V [\nabla \times \overline{\overline{G}}(\mathbf{r} - \mathbf{r}')] \cdot \mathbf{J}_{ms}(\mathbf{r}') dV'. \quad (2.11)$$

Equations (2.6)-(2.11) present in a compact way how current sources induce radiating fields. In practice, the fields are commonly calculated in the free space, and permeability and permittivity can be replaced with the values in vacuum, i.e.  $\mu = \mu_0$  and  $\epsilon = \epsilon_0$ .

### 2.2.3 Field regions

Three field regions which depend on the distance from the antenna are shown in Fig.(2.1). The region nearest to the antenna is called the reactive near-field region, the second region is the radiating near-field region or the *Fresnel region* and the furthest one is called the far-field region or the *Fraunhofer region*. The radiation pattern of an antenna is determined in the far-field region.

The reactive near-field region has to be usually taken into account when investigating current distributions of antenna elements or calculating mutual coupling between antennas on an array (Lindell & Nikoskinen, 1995). The reactive near-field limit is defined as "that portion of the near-field region immediately surrounding the antenna, wherein the reactive field predominates" (IEEE, 1993). The outer boundary of this region is taken to exist at distance  $R_1 < \frac{2L^2}{3\sqrt{3}\lambda}$ , where  $L$  is the

longest dimension of an antenna element and  $\lambda$  is the wavelength (see Fig.(2.1)). When calculating the fields in reactive near-field region the exact field equations (2.6) and (2.9) or (2.10) and (2.11) have to be used. The region between distances

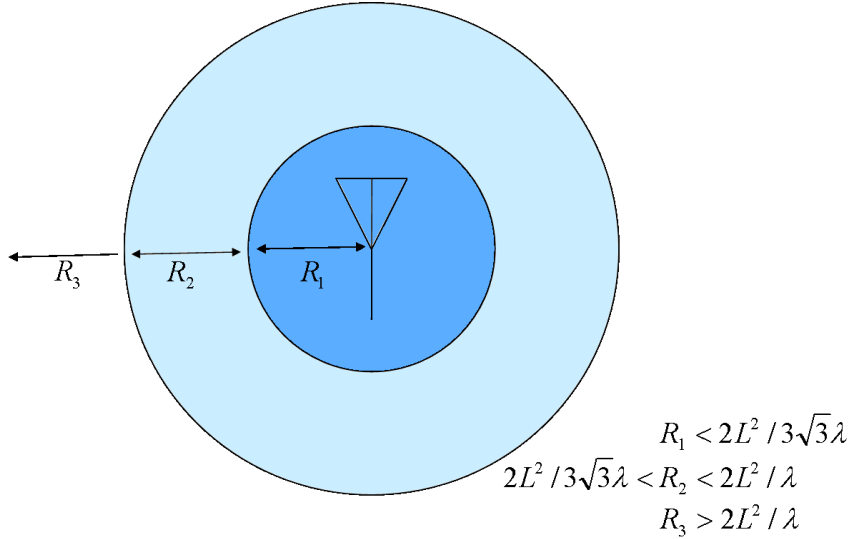


Figure 2.1: Figure 2.1: Field regions of an antenna: 1) reactive near-field region, 2) Fresnel region and 3) Fraunhofer region.

$\frac{2L^2}{3\sqrt{3}\lambda} < R_2 < \frac{2L^2}{\lambda}$  away from the antenna is called the Fresnel region. Fresnel region is defined as "that portion of the near-field region of an antenna between the far-field and the reactive portion of the near-field region, wherein the angular field distribution is dependent upon distance from the antenna" (IEEE, 1993). According to the definition, the radiation pattern is not yet formed in the Fresnel region. But, in the Fresnel region some approximations can be made when calculating radiating fields. If  $|\mathbf{r}| \gg |\mathbf{r}'|$  the Green's dyadic can be simplified. It turns out that  $\nabla$ -operators can be replaced with  $-jk\mathbf{u}_r$  in equation (2.7) (Lindell & Nikoskinen, 1995). Now, Green's dyadic can be simplified as

$$\lim_{r \rightarrow \infty} \overline{\overline{G}}(\mathbf{r} - \mathbf{r}') = (\overline{\overline{I}} - \mathbf{u}_r \mathbf{u}_r) G(\mathbf{r} - \mathbf{r}'). \quad (2.12)$$

The electric field approximation yields

$$\mathbf{E}(\mathbf{r}) = -j\omega\mu(\overline{\overline{I}} - \mathbf{u}_r \mathbf{u}_r) \cdot \int_V G(\mathbf{r} - \mathbf{r}') \mathbf{J}_s(\mathbf{r}') dV', \quad (2.13)$$

and magnetic field can be calculated using the integral

$$\mathbf{H}(\mathbf{r}) = -j\omega k \mathbf{u}_r \times \int_V G(\mathbf{r} - \mathbf{r}') \mathbf{J}_s(\mathbf{r}') dV'. \quad (2.14)$$

The far-field or the Fraunhofer region is defined as "the region of the field of an antenna where the angular field distribution is essentially independent of the distance from a specific point in the antenna region" (IEEE, 1993). In the far-field region the antenna looks like a point source and a radiation pattern is formed. In the far-field region further approximations can be done when calculating electric and magnetic fields. Let us use Taylor's approximation of the first two terms for distance  $D$ ,

$$D = |\mathbf{r} - \mathbf{r}'| \approx \sqrt{r^2 - 2\mathbf{r} \cdot \mathbf{r}' + r'^2} \approx r \sqrt{1 - \frac{2\mathbf{r} \cdot \mathbf{r}'}{r^2}} \approx r - \mathbf{u}_r \cdot \mathbf{r}'. \quad (2.15)$$

Now, the scalar Green's function (2.8) can be written with approximation

$$G(\mathbf{r} - \mathbf{r}') = \frac{e^{-jk(r - \mathbf{u}_r \cdot \mathbf{r}')}}{4\pi(r - \mathbf{u}_r \cdot \mathbf{r}')} \approx \frac{e^{-jkr} e^{jk\mathbf{u}_r \cdot \mathbf{r}'}}{4\pi r}. \quad (2.16)$$

Using (2.16) in (2.13), the electric far-field yields

$$\mathbf{E}(\mathbf{r}) \approx -j\omega\mu \frac{e^{-jkr}}{4\pi r} (\bar{\mathbf{I}} - \mathbf{u}_r \mathbf{u}_r) \cdot \int_V e^{jk\mathbf{u}_r \cdot \mathbf{r}'} \mathbf{J}_s(\mathbf{r}') dV'. \quad (2.17)$$

The magnetic field for the far-field region can be approximated from (2.17) using (2.15)

$$\mathbf{H}(\mathbf{r}) \approx -jk \frac{e^{-jkr}}{4\pi r} \mathbf{u}_r \times \int_V e^{jk\mathbf{u}_r \cdot \mathbf{r}'} \mathbf{J}_s(\mathbf{r}') dV'. \quad (2.18)$$

The relation  $R_3 > \frac{2L^2}{\lambda}$  is commonly used to define the limit of the far-field region. Idea behind the definition is that higher terms of Taylor's approximation would give an effect much smaller than  $90^\circ$  on the phase term (Nikoskinen, 2004). In practice, in the limit of the far-field region the phase difference produced by the center and the edge of an antenna is  $22.5^\circ$  (Räisänen & Lehto, 2001). It is seen from the equations (2.17) and (2.18) that  $\mathbf{E}(\mathbf{r}) \approx \frac{\omega\epsilon}{k} \mathbf{u}_r \times \mathbf{H}(\mathbf{r})$  and  $\mathbf{H}(\mathbf{r}) \approx \frac{k}{\omega\epsilon} \mathbf{u}_r \times \mathbf{E}(\mathbf{r})$ , where  $\frac{k}{\omega\epsilon} = \sqrt{\frac{\mu}{\epsilon}} = \eta$ . In air  $\eta = \eta_0 \approx 377\Omega$ . The ratio of the electric and magnetic field amplitudes is  $\eta$ , which is the case also with a plane wave. Field vectors are orthogonal and transversal to the radial direction. Fields have only first power distance dependence which is seen from  $\frac{e^{-jkr}}{4\pi r}$ . Far away from the antenna the radiated waves look like plane waves in a particular direction, but in reality the fields form spherical waves that propagate away from the antenna. The previous

divisions into the three field regions are not suitable in all cases and they are more recommendations than strict rules. However, they are often useful when estimating the distance of the far-field region when conducting antenna measurements.

## 2.3 Basic antenna parameters

Radiation parameters are used to characterise performance of an antenna when designing and measuring antennas. In this Section, terms like radiation pattern, beamwidth, radiation lobes, directivity, gain, polarisation, bandwidth and input impedance are introduced. Also, scattering parameters and the Friis transmission equation for a radio link are presented.

### 2.3.1 Radiation pattern

Radiation pattern is defined as "the spatial distribution of a quantity that characterises the electromagnetic field generated by antenna" (IEEE, 1993). Radiation pattern can be a two- or three-dimensional spatial distribution of power flux density, radiation intensity, field strength, directivity, phase or polarisation. Radiation pattern is a function of the observer's position along a path or surface of constant radius (Balanis, 1997) and goes through a direction at which maximum radiation occurs. Usually, the spherical coordinate system is used to visualise the radiation pattern. A two-dimensional pattern can be a function of the elevation angle,  $\theta$ , at constant azimuth angle,  $\phi$ , or a function of  $\phi$  at constant  $\theta$ -value. The spherical coordinate system is shown in Fig.(2.2). For a linearly polarised antenna, such as a rectangular microstrip antenna, radiation patterns are often drawn in terms of the principal E- and H-plane patterns. By definition, E-plane is "the plane containing the electric field vector and the direction of maximum radiation" and H-plane is "the plane containing the magnetic field vector and the direction of maximum radiation" (IEEE, 1993).

### 2.3.2 Beamwidth

Beamwidth can be defined as an angle between the first zero points around the main beam. Usually, the half-power beamwidth is used which is defined as follows: "In a radiation pattern cut containing the direction of the maximum of a lobe, the angle between the two directions in which the radiation intensity is one-half the maximum value" (IEEE, 1993).

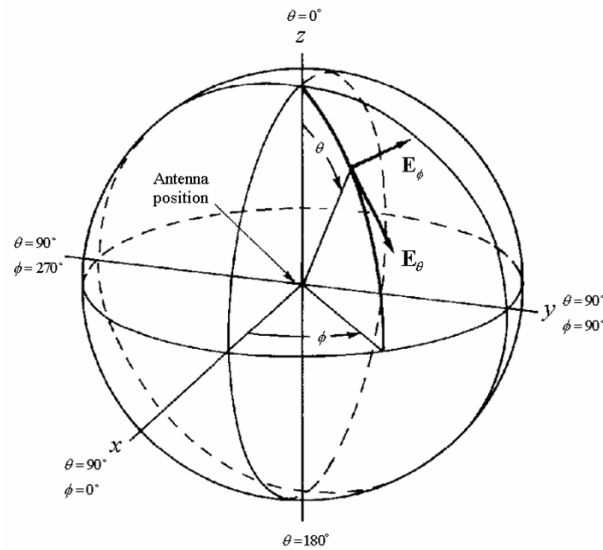


Figure 2.2: Standard spherical coordinate system for antenna analysis, modified from (IEEE, 1979).

### 2.3.3 Radiation lobes

The radiation pattern is divided into lobes which are "portions of the radiation pattern bounded by regions of relatively weak radiation intensity" (Balanis, 1997). Radiation lobes are subclassified into major or main, minor, side and back lobes. The major lobe is "the radiation lobe containing the direction of maximum radiation" and the minor lobe is "any radiation lobe except a major lobe" (IEEE, 1993). Side lobe is defined as "a radiation lobe in any direction other than that of the major lobe". Usually the side lobe is adjacent to the main lobe. The side-lobe level is the maximum value of the side lobe or side lobes compared to the maximum value of the main beam (Lindell & Nikoskinen, 1995). Side lobes are usually undesirable and their levels should be minimised. The back lobe is defined as "a radiation lobe whose axis makes an angle of approximately 180 degrees with respect to the beam axis of an antenna" (IEEE, 1993). Usually, this means that the back lobe points out on a hemisphere that is opposite to that of the major lobe.

### 2.3.4 Directivity

Directivity is "the ratio of the radiation intensity in a given direction from the antenna to the radiation intensity averaged over all directions" (IEEE, 1993). It is a function of direction but it is often defined only to the direction of the major lobe.

Directivity can be expressed as

$$D(\mathbf{u}_r) = \frac{w(\mathbf{u}_r)}{P_t/4\pi} = \frac{4\pi|\mathbf{E}(\mathbf{r})|^2}{\int |\mathbf{E}(\mathbf{r})|^2 d\Omega}, \quad (2.19)$$

where  $w(\mathbf{u}_r)$  is the radiation density per solid angle i.e. in a direction  $\mathbf{u}_r$ ,  $P_t$  is the total power transmitted by the antenna and  $\Omega$  is the solid angle (Lindell & Nikoskinen, 1995).

### 2.3.5 Gain

Gain is "the ratio of the radiation intensity, in a given direction, to the radiation intensity that would be obtained if the power accepted by the antenna were radiated isotropically". Isotropic radiator is defined as "a hypothetical, lossless antenna having equal radiation intensity in all directions" (IEEE, 1993). So, the gain is almost the same as directivity but conductor losses and dielectric losses of the antenna are taken into account<sup>1</sup>. Gain can be expressed as

$$G = \eta_r D \quad (2.20)$$

where  $\eta_r$  is the radiation efficiency, which is the ratio of the radiated power and the input power. In practice, gain is always smaller than directivity.

### 2.3.6 Polarisation

Polarisation of an antenna in a given direction is defined as "the polarisation of the wave transmitted by the antenna" (IEEE, 1993). When the direction is not stated, the polarisation is taken to be the polarisation in the direction of maximum gain. Because typically the antenna has the same characteristics in both receive and transmit modes (Sihvola & Lindell, 1996), the antenna polarisation can also be defined as a polarisation of the received wave which maximises the voltage in the antenna port (Nikoskinen, 2004). Polarisation of a wave describes the temporal behaviour of the wave i.e. what kind of route the end the point of the electric field vector travels along time. As in the equation (2.3) is shown, the polarisation depends on the relationship of the vectors  $\mathbf{E}_r$  and  $\mathbf{E}_i$ . Three types of polarisation can be identified: linear, elliptical and circular polarisations (Balanis, 1997) (see Fig.(2.3)). Linear polarisation occurs when  $\mathbf{E}_r = 0$ , or  $\mathbf{E}_i = 0$ , or  $\mathbf{E}_r \times \mathbf{E}_i = 0$  (Sihvola & Lindell, 1996), i.e. either the real part or the imaginary part of the field vector is

<sup>1</sup>Sometimes surface and substrate modes are generated and they also reduce gain. However, "Gain does not include losses arising from impedance and polarisation mismatches" (IEEE, 1993)



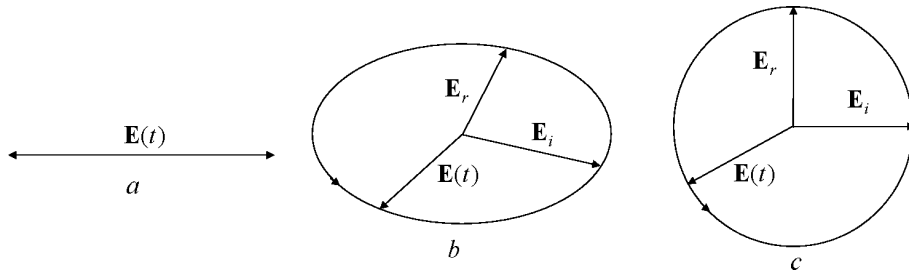


Figure 2.3: Wave polarisations, a) linear polarisation, b) elliptical polarisation and c) circular polarisation.

zero or they are parallel. The end point of an electric field vector draws a line in space along time. If  $\mathbf{E}_r \times \mathbf{E}_i \neq 0$ ,  $|\mathbf{E}_r| \neq |\mathbf{E}_i|$  and  $\mathbf{E}_r \cdot \mathbf{E}_i \neq 0$ , the polarisation is called elliptical. Electric field vector draws an ellipse, which lies on the perpendicular plane to the propagation direction, along time. The rotation direction of the ellipse is the same as the rotation direction of the shortest path from  $\mathbf{E}_i$  to  $\mathbf{E}_r$  (Lindell, 1997). The polarisation is called circular when the electric field vector draws a circle along time. This occurs when  $\mathbf{E}_r$  and  $\mathbf{E}_i$  are equal in amplitude and they are perpendicular, i.e.  $|\mathbf{E}_r| = |\mathbf{E}_i|$  and  $\mathbf{E}_r \cdot \mathbf{E}_i = 0$ . The circular polarisation is a special case of the elliptical polarisation. There is a rule of thumb for handedness of the elliptical and circular polarisations. The polarisation is called right-handed when the thumb points towards propagation direction while other fingers point towards the direction of rotation of the circle. The opposite situation is called the left-handed polarisation. Right- and left-handed circular polarisations are abbreviated as RHCP and LHCP, respectively. The wave polarisations are illustrated in Fig.(2.3).

### 2.3.7 Friis transmission equation

The Friis transmission equation describes the power transmission over a radio link. If the input power of the transmitting antenna is  $P_t$  and it is considered as an isotropic radiator, the power density at distance  $d$  (Fig.(2.4)) from the antenna is

$$S_{isotr} = \frac{P_t}{4\pi d^2}. \quad (2.21)$$

The transmitting antenna is not an isotropic radiator but has directivity  $D_t$  depending on the direction from the antenna. Using the relationship (2.20) between directivity and gain, the power density caused by the transmitting antenna yields

$$S_t = \frac{G_t P_t}{4\pi d^2}. \quad (2.22)$$

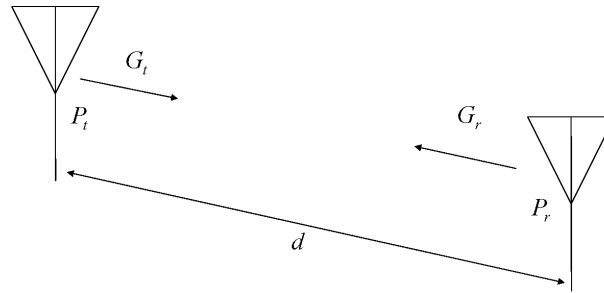


Figure 2.4: Radio link between transmitting and receiving antennas.

where  $G_t$  is the gain of the transmitting antenna. Receiving antenna catches the power equal to the multiplication of the transmitter power density,  $S_t$ , and the effective area of the receiving antenna,  $A_{er}$  (Räisänen & Lehto, 2001)

$$P_r = S_t A_{er} = S_t \frac{\lambda^2 G_r}{4\pi} = \frac{G_t P_t}{4\pi d^2} \frac{\lambda^2 G_r}{4\pi} = G_t G_r \left( \frac{\lambda}{4\pi d} \right)^2 P_t. \quad (2.23)$$

The effective area is defined as follows: "In a given direction, the ratio of the available power at terminals of a receiving antenna to the power flux density of a plane wave incident on the antenna from that direction, the wave being polarisation matched to the antenna" (IEEE, 1993). It can be seen from the equation (2.23) that the received power is inversely proportional to the square of the distance between the antennas and proportional to the square of the wavelength. In practice, the received power is smaller than predicted by (2.23) because of the atmospheric attenuation, misdirected antennas and mismatches of polarisation and impedances. Especially, at the 60 GHz frequency band the path loss due to oxygen absorption is significant. At sea level the oxygen absorption loss is 15 dB/km at 60 GHz and over 10 dB/km at frequency range 57...63 GHz (Lehto & Räisänen, 2002a).

### 2.3.8 Input impedance

The input impedance of an antenna is defined as "the impedance presented by an antenna at its terminals" (IEEE, 1993). The real part of the impedance is called the antenna input resistance,  $R_a$ , and is related to the material and radiation losses in the antenna. The imaginary part of the input impedance, the antenna input reactance  $X_a$ , is formed by the antennas reactive near field which stores energy. In the reactive near field the power flows back and forth near the antenna. This can be compared with the energy vibrating in an inductor or a capacitor (Lindell &

Nikoskinen, 1995). The input impedance can be written as

$$Z_a = R_a + jX_a. \quad (2.24)$$

The antenna input resistance can be divided into radiation and loss resistances of the antenna

$$R_a = R_r + R_l. \quad (2.25)$$

The radiation resistance describes the energy that is transferred from the antenna to the air. Loss resistance includes energy that is wasted into the conductor and dielectric losses. So, the radiation efficiency can be expressed as (Balanis, 1997)

$$\eta_r = \frac{R_r}{R_r + R_l}. \quad (2.26)$$

As shown in equation (2.26), the smaller the radiation resistance the smaller the radiation efficiency. Maximum power is delivered through the antenna when conjugate matching is achieved between the antenna impedance and the generator impedance. The antenna input impedance is usually dependent on the frequency and the antenna has a range of frequencies at which it operates. The input impedance depends also on the antenna geometry, method of excitation of the antenna and the proximity of the antenna to the surrounding objects (Balanis, 1997).

### 2.3.9 Scattering parameters

The scattering parameters are defined from the voltages entering,  $V_i^+$ , and leaving,  $V_i^-$ , the microwave network ports (Räisänen & Lehto, 2001). For example, a linear two-port network, having equal characteristic impedances at each port, can be expressed with a scattering matrix as

$$\begin{pmatrix} V_1^- \\ V_2^- \end{pmatrix} = \begin{pmatrix} S_{11} & S_{12} \\ S_{21} & S_{22} \end{pmatrix} \begin{pmatrix} V_1^+ \\ V_2^+ \end{pmatrix} \quad (2.27)$$

The scattering matrix can be extended for the network with multiple ports. By definition, the  $S_{11}$  and  $S_{22}$  represent reflection coefficients at ports 1 and 2, respectively. Parameters  $S_{12}$  and  $S_{21}$  are the transmission coefficients between ports 1 and 2. An antenna is usually fed by using a transmission line. Usually, the  $S_{11}$ -parameter measurements are conducted for the input port of the antenna to test how well the antenna input impedance is matched to the specific port impedance, for example to

50Ω. The reflection coefficient at port 1 can be calculated as

$$S_{11} = \frac{Z_l - Z_{01}}{Z_l + Z_{01}}, \quad (2.28)$$

where  $Z_l$  and  $Z_{01}$  denote the load and port impedances, respectively. The S-parameter results are usually expressed as a normalised input impedance on a Smith chart or as a return loss

$$L_{ret} = 20 \log \frac{1}{|S_{11}|}, \quad (2.29)$$

in decibels in a rectangular graph. The return loss describes the ratio of the reflected power to the power of the incident wave. In equation (2.29), the return loss is given as a positive number: the bigger the number the smaller the return loss. In practice, the return loss is often given as a negative value, i.e. the more negative value implies the smaller return loss.

### 2.3.10 Bandwidth

The bandwidth of an antenna is defined as "the range of frequencies within which the performance of the antenna, with respect to some characteristic, conforms to a specified standard" (IEEE, 1993). The bandwidth can be considered as a range of frequencies beside the center frequency where the antenna parameters, such as input impedance, radiation pattern, beamwidth, polarisation, side-lobe level and gain are within an acceptable value from those at the center frequency. Often the distinction between the impedance bandwidth and the pattern bandwidth is used (Kraus, 2002). There is no unique characterisation for the bandwidth and the specifications depend on the particular application. Usually, the bandwidth is expressed in percents, i.e. as the percentage of the frequency difference at the edges of an frequency range, compared to the center frequency of the bandwidth. Often the term bandwidth is simply used when impedance bandwidth is considered. The impedance bandwidth is usually specified as a frequency range over which the *voltage standing wave ratio* (VSWR) is less than 2 (Kumar & Ray, 2003). For the antenna input port

$$\text{VSWR} = \frac{1 + |S_{11}|}{1 - |S_{11}|} < 2 \Rightarrow |S_{11}| < \frac{1}{3}, \quad (2.30)$$

which corresponds to a return loss of 9.5 dB or above.

## 2.4 Antenna arrays

The radiation pattern of a single microstrip antenna element is typically wide (the -3 dB beamwidth  $\sim 70^\circ$ ) and has a low gain value. Like it was shown in equation (2.23), the received power depends on the gains of the receiving and transmitting antennas: the received power increases as the gain is increased. To enhance the antenna gain, i.e. to focus the radiation more into a specific direction, the electrical size of the antenna has to be enlarged. Another way is to place two or more antennas with similar characteristics in an array, where antennas are in a particular geometrical formation. An array antenna is defined as "an antenna comprised of a number of identical radiating elements in a regular arrangement and excited to obtain a prescribed radiation pattern" (IEEE, 1993). So, the antenna array is a group of antennas which fulfils specific requirements.

### 2.4.1 Antenna array factor

The far-field of the antenna array element  $i$  located at  $\mathbf{r}_i$  can be computed from the far-field of the basic element,  $\mathbf{E}_o(\mathbf{r})$ , located at the origin as follows (Lindell & Nikoskinen, 1995)

$$\mathbf{E}_i(\mathbf{r}) = a_i e^{jk\mathbf{u}_r \cdot \mathbf{r}_i} \mathbf{E}_o(\mathbf{r}). \quad (2.31)$$

So, only the far-field of the basic antenna element has to be calculated. The far-fields of other elements of the array differ from the basic element with phase and magnitude factors. Let us assume that there are  $N$  elements in an array, their amplitudes and phases defined by factors  $a_1, a_2, a_3, \dots, a_N$ . The position vectors of the elements are  $\mathbf{r}_1, \mathbf{r}_2, \mathbf{r}_3, \dots, \mathbf{r}_N$ , respectively. The far-field of the array can be expressed as a sum

$$\mathbf{E}_i(\mathbf{r}) = \sum_{n=1}^N a_n e^{jk\mathbf{u}_r \cdot \mathbf{r}_n} \mathbf{E}_o(\mathbf{r}) = f(\mathbf{u}_r) \mathbf{E}_a(\mathbf{r}), \quad (2.32)$$

where  $f(\mathbf{u}_r)$  is referred to as an array factor and it is independent of the characteristics of the elements. The far-field of an antenna array is a multiple of the array factor and the far-field of an individual element. When designing antenna arrays, it is often simpler to examine the array factor separately from the elements' far-fields to achieve desirable radiation characteristics.

### 2.4.2 Array factor of a linear array

Often, a constant phase shift is used between adjacent array elements and the feeding of the elements is thus called progressive. Usually, all the elements are fed with uniform current amplitudes, because it is simpler to use identical feeding circuits for the elements. Also the separation of the elements is usually kept constant, because of the lack of deterministic design method for arrays with unequal element spacing (Lindell & Nikoskinen, 1995), thus  $|\mathbf{r}_{n+1} - \mathbf{r}_n| = \text{constant}$ .

Let us first consider a linear array of  $N$  elements where the elements are placed along the  $x$ -axis in the spherical coordinates (see Fig.(2.5 a)). The array factor can be expressed as

$$f(\mathbf{u}_r) = \sum_{n=1}^N a_n e^{jkd_x \sin \theta \cos \phi}, \quad (2.33)$$

where the azimuth angle,  $\phi = 0$  or  $\phi = \pi \Rightarrow \cos \phi = \pm 1$ .  $d_x$  is the element separation in the  $x$ -direction. With a constant phase shift and equal feeding amplitudes the excitation factor of the element  $n$  can be written in a form

$$a_n = a e^{j\delta_{nx}}, \quad (2.34)$$

where  $a$  is real. The phase of the element  $n$  is  $\delta_{nx} = (n-1)\delta_x$ , where  $\delta_x$  represents a constant phase shift. The equation (2.33) now yields

$$f(\Psi_N) = \sum_{n=1}^N a e^{j(n-1)(jkd_x \sin \theta \cos \phi + \delta_x)} = a \sum_{n=1}^N e^{(j\Psi_N)^{(n-1)}}, \quad (2.35)$$

where  $\Psi_N = jkd_x \sin \theta \cos \phi + \delta_x$ . The equation (2.35) is a geometric series and can be summed up in a closed form as

$$S_n = \sum_{t=1}^T w^k = \frac{w(1-w^T)}{1-w}, \quad (2.36)$$

which can be further simplified using complex properties of the sine function,  $\sin \psi = (e^{j\psi} - e^{-j\psi})/(j2)$ :

$$f(\Psi_N) = a e^{j(N-1)\Psi_N/2} \frac{\sin(N\Psi_N/2)}{\sin(\Psi_N/2)}. \quad (2.37)$$

The maximum value of  $\sin(N\Psi_N/2)/\sin(\Psi_N/2)$  is equal to  $N$  ( $\Psi_N = 0$ ). If the feed amplitudes are normalised i.e.  $a = 1/N$ , the absolute value of the array factor yields

$$|f(\Psi_N)| = \left| \frac{\sin(N\Psi_N/2)}{N \sin(\Psi_N/2)} \right|. \quad (2.38)$$

Let us inspect the array factor in the  $xz$ -plane ( $\phi = 0, \phi = \pi$ ). The direction of the major lobe,  $\theta_{max}$ , is obtained from  $\Psi_N(\theta_{max}) = 0$ . This occurs, when ( $\phi = 0, \delta_x = -kd_x$ ) or ( $\phi = \pi, \delta_x = kd_x$ ). For the real values of the angle,  $|\delta_x| \leq kd_x$ . When the phase shift is  $\delta_x = 0$ ,  $\theta_{max} = 0$  or  $\theta_{max} = \pi$ , the array is called *broadside array*. For the *end-fire array*  $\delta_x = \pm kd_x$  and the major lobe is directed at ( $\theta_{max} = \pi/2, \phi = 0$ ) or ( $\theta_{max} = \pi/2, \phi = \pi$ ). With phase shifts between  $-kd_x \leq \delta_x \leq kd_x$  the major lobe can be directed between angles  $0 \leq \theta \leq \pi/2$ . It should be remembered that the array factor of a linear array is rotationally symmetrical around the  $x$ -axis (see Fig.(2.6 a)).

### 2.4.3 Array factor of a planar array

A planar array, which can be thought as an array formed by the combination of several linear arrays (Fig.(2.5 b)), can also be used to enhance the directivity and the gain. Planar arrays provide more symmetrical patterns than linear arrays with lower side lobes. With a planar array the main beam of the antenna can be directed towards any point in space (Balanis, 1997). The rectangular array of  $N \times M$  elements is formed by an  $M$ -element linear array consisting of  $N$ -element linear arrays. The array factor for the  $M$ -element linear array, which is located in the  $y$ -axis, is

$$f(\Psi_M) = \sum_{m=1}^M a e^{j(m-1)(jkd_y \sin \theta \sin \phi + \delta_y)}. \quad (2.39)$$

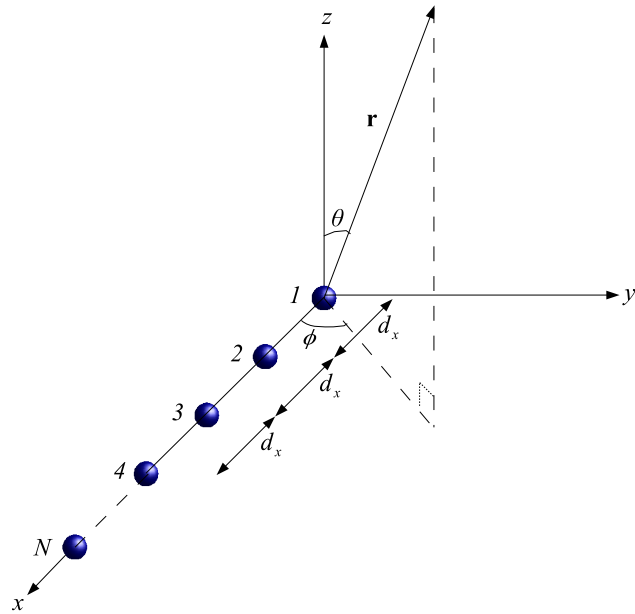
The array factor for the entire planar array is a multiple of two linear array factors

$$\begin{aligned} f(\Psi_{NM}) &= a \sum_{n=1}^N \left[ \sum_{m=1}^M a e^{j(m-1)(jkd_y \sin \theta \sin \phi + \delta_y)} \right] e^{j(n-1)(jkd_x \sin \theta \cos \phi + \delta_x)} \\ &= f(\Psi_N) f(\Psi_M), \end{aligned} \quad (2.40)$$

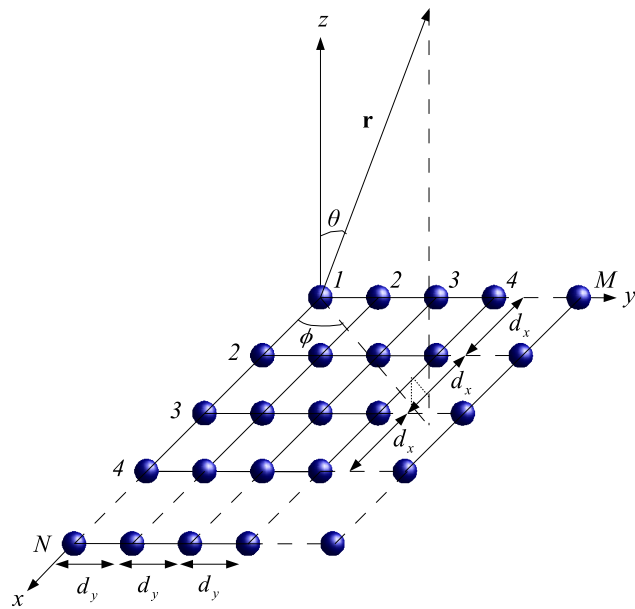
where the phase shifts  $\delta_x$  and  $\delta_y$  are constants but not necessarily equal. The absolute value of the array factor for the planar array can be written as

$$|f(\Psi_{NM})| = \left| \frac{\sin(N\Psi_N/2)}{N \sin(\Psi_N/2)} \frac{\sin(M\Psi_M/2)}{M \sin(\Psi_M/2)} \right|, \quad (2.41)$$

where  $\Psi_N = jkd_x \sin \theta \cos \phi + \delta_x$  and  $\Psi_M = jkd_y \sin \theta \sin \phi + \delta_y$ . The geometries of linear and planar arrays are presented in Fig.(2.5). The absolute values of the array factors in three dimensions are also shown in Fig.(2.6 a) and Fig.(2.6 b) for linear and planar arrays, respectively.



(a)



(b)

Figure 2.5: Antenna arrays: a) a linear array and b) a planar array.



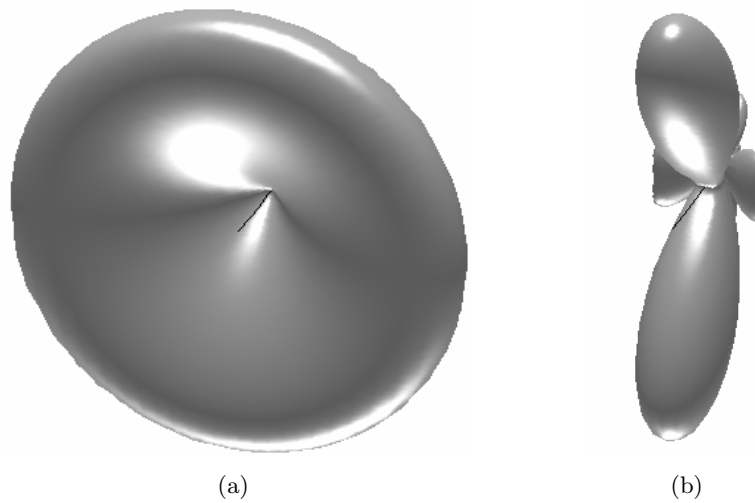


Figure 2.6: Array factors for a) linear and b) planar array.

## Chapter 3

# Microstrip antennas

### 3.1 Microstrip, dipole and slot antennas

In the millimetre-wave region reflector, lens, leaky-wave, microstrip, slot and dipole antennas are widely used. Microstrip, slot and dipole antennas are the most suitable for low-cost mass production and can be fabricated by applying LTCC technology. Also, microstrip, dipole and slot antennas can be integrated with active circuits and they enable small, cost effective packaging.

A dipole antenna is usually a half-wavelength or wavelength long metal wire or strip printed on a substrate. The feeding of a dipole can be done using a microstrip line. A slot antenna is a gap or aperture, whose width is much smaller than the length or wavelength, on a metal plate. The coplanar waveguide (CPW) is suitable for the feeding of slot antennas (Lehto & Räsänen, 2002a). The CPW enables the direct connection to the integrated circuit and no via holes between different substrate layers are needed. The microstrip antenna is constructed of a metal plate on a grounded dielectric substrate. Several feeding mechanisms can be used for the microstrip antenna (see Section 3.3) and they offer the designer many parameters to optimise the antenna performance. The microstrip antenna can be separated from the other circuitry to prevent distortions to the operation of the antenna and the circuit.

The directivities of the dipole, slot and microstrip antennas are in the same order and antenna arrays have to be constructed if sharper radiation beam is desired (Lindell & Nikoskinen, 1995). The feeding mechanisms of microstrip antenna enable separation of the antenna elements and the array feeding circuit. Flexibility of the microstrip antenna configurations was the main reason why these structures were chosen to be designed and manufactured on LTCC.

### 3.2 Basic characteristics of microstrip antennas

The microstrip antenna is "an antenna that consists of thin metallic conductor bonded to a thin grounded dielectric substrate" (IEEE, 1993). The antenna element can be square, triangular, rectangular, circular, elliptical, disc sector, circular ring or ring sector. The radiation of the microstrip antenna is based on the discontinuities of the antenna element but may also occur from bends of the antenna element (Lehto & Räsänen, 2002b).

The radiation characteristics of a rectangular microstrip antenna can be estimated from the field distributions of the patch. The antenna is assumed to operate at the basic resonance mode at which the electric field under the patch is uniform in the direction of the radiating edges and sinusoidal in the direction of the non-radiating edges. The radiating element can be replaced approximately with an equivalent magnetic surface current which can be calculated as follows

$$\mathbf{J}_{s,m}(\mathbf{r}) = -\mathbf{n} \times \mathbf{E}(\mathbf{r}), \quad (3.1)$$

where  $\mathbf{n}$  is the normal vector of a particular surface. When using equation (3.1) for the electric field of the patch it is seen that the equivalent magnetic current model of the patch is a loop consisting of parallel and opposite magnetic current sources (see Fig.(3.1 a)). The opposite currents cancel each others radiation. The effect of the ground plane, at distance  $h_p$ , on the radiation can be taken into account by replacing the ground plane with image currents. Thus, the radiation of the patch is induced by a planar array of four magnetic current source elements with element distances  $l_p$  and  $2 \times h_p$  (see Fig.(3.1 b)). The phase shift between the elements is zero and the maximum radiation occurs at  $z$ -direction. Let us now assume that  $h_p$  is small and the radiation is produced by a two-element linear array. Illustrations of the E- and H-plane radiation patterns are presented in Fig(3.2). In the E-plane, ( $\phi = \pm 90^\circ$ ,  $0^\circ \leq \theta \leq 180^\circ$ ) the radiation pattern is almost circular and the radiation pattern is determined mainly by the array factor. In the H-plane, ( $\phi = 0^\circ$  or  $\phi = 180^\circ$ ,  $0^\circ \leq \theta \leq 180^\circ$ ) the radiation pattern is narrow, donut-like, and the array factor is circular due to symmetry around the array axis. It should be kept in mind that, in reality, the ground plane eliminates most of the back radiation and the radiation pattern is halved of those shown in Fig(3.2).

The microstrip antenna has some disadvantages, such as narrow bandwidth, poor polarisation purity, low power and sensitivity to manufacturing errors. If large operating frequency band is not necessary, the narrow bandwidth is beneficial because

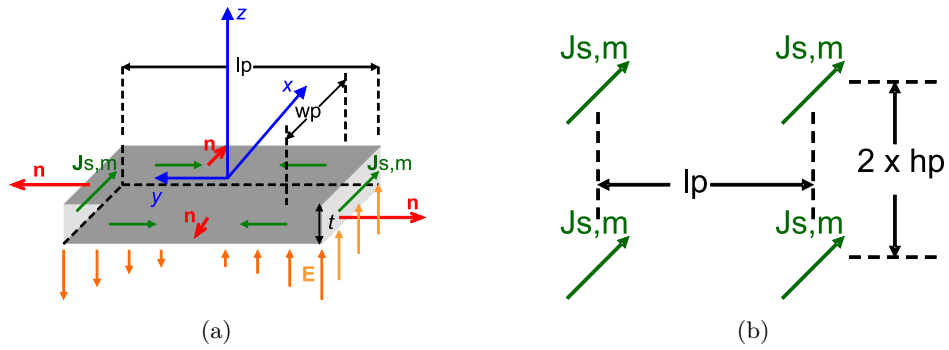


Figure 3.1: The equivalent magnetic current sources of a) a rectangular patch element and b) a patch element with ground plane.

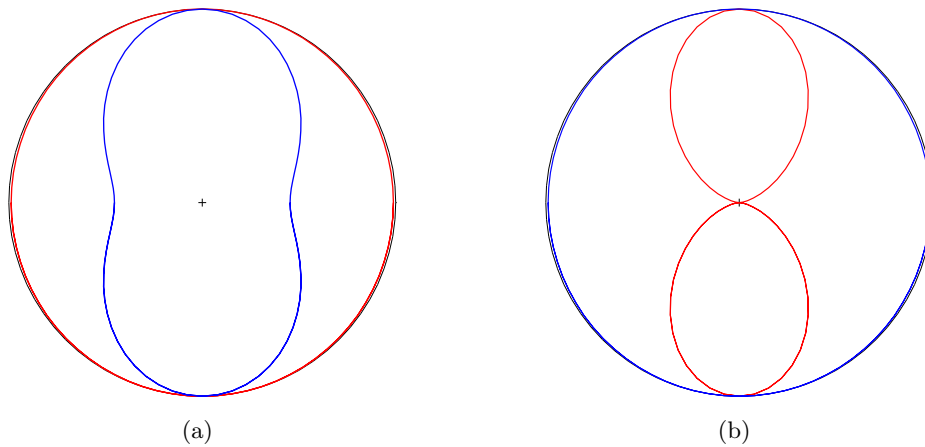


Figure 3.2: Illustrations of the radiation pattern (red line) and the array factor (blue line) of an equivalent magnetic current sources of a microstrip antenna in the a) E-plane and b) H-plane.

the signals outside the operating frequency band are filtered out. In some applications a large bandwidth is required. The bandwidth can be enhanced, for example, by stacking multiple patches with slightly different resonance frequencies relatively close to each other.

Microstrip antennas have also many advantages. They are small, light weight, planar and easily integrated with the integrated circuits also in the 60 GHz frequency band. Planarity suits well with the layered LTCC structures and the metallization can be fabricated using screen printing, photopatterning or etching technologies used in the LTCC process. The shape and size of the antenna element can be modified to find optimal radiation characteristics. Different feeding mechanisms can be used to fulfil the specific requirements of the environment of the antenna.

### 3.3 Feeding mechanisms of microstrip antennas

The feeding of a microstrip antenna can be done using a coaxial probe, a microstrip line, proximity-, aperture- or slot-coupling (Balanis, 1997). The feeding mechanisms are presented in Fig.(3.3). The coaxial-line feed is formed by the inner conductor of the coax attached to the radiating patch and the outer conductor is connected to the ground plane like it is shown in Fig.(3.3 a). It is not so easy to fabricate with the LTCC technology and has only one degree of freedom for the design; the positioning of the feed point. Through the probe positioning, the input impedance can be adjusted. The microstrip line feed is done by connecting the microstrip line to the other end of the antenna element Fig.(3.3 b). It is easy to manufacture and the antenna has a simple structure. Both, the probe feed and the microstrip-line feed suffer from bandwidth/feed radiation trade-off. An increase in the substrate thickness to increase bandwidth leads to an increase of spurious feed radiation and increased surface wave power (Pozar, 1992). Probe and microstrip-line feeds also excite higher-order modes of the antenna in addition to the dominant mode and cross-polarised radiation is produced. Non-contacting feeds, such as proximity-coupled and aperture-coupled feeds, offer more degrees of freedom for the designer and have become popular nowadays. The proximity-coupled feed uses a two-layer substrate with a microstrip line on the lower substrate, terminating in an open stub below the antenna element which is printed on the upper substrate (Fig.(3.3 c)). The length of the feeding stub and the antenna element width-to-microstrip line width ratio can be varied to adjust the input impedance of the antenna. The proximity coupling allows antenna element to exist on a relatively thick substrate, and the bandwidth can be improved. Modified proximity-coupling feed uses an aperture in a ground

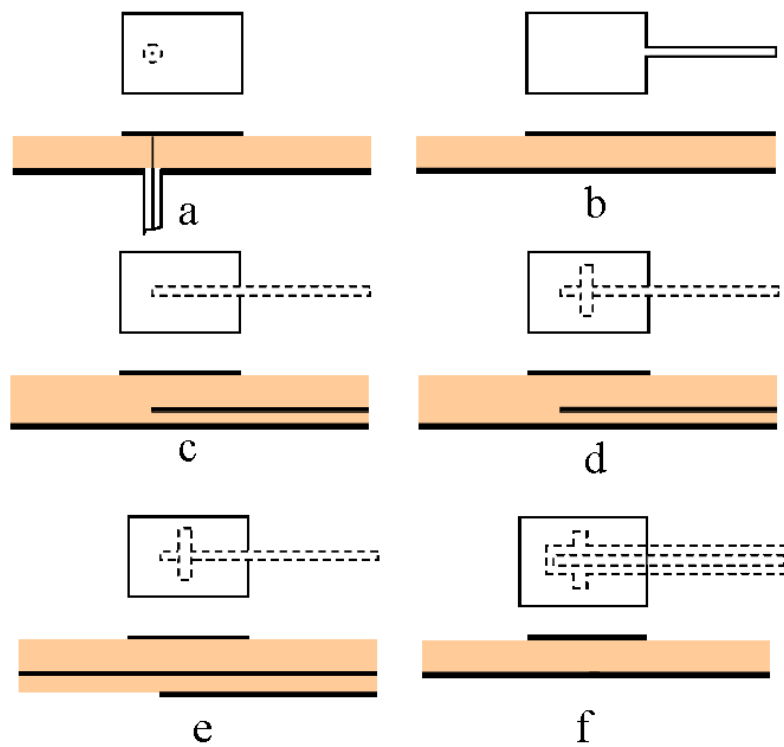


Figure 3.3: Typical feeds of the microstrip antennas, a) probe feed, b) microstrip line feed, c) proximity-coupled feed, d) modified proximity-coupled feed (aperture in the ground plane), e) microstrip line-fed aperture-coupled feed (aperture in the ground plane) and f) coplanar waveguide-fed slot-coupled feed (slot in the ground plane).

plane (Fig.(3.3 d)) and the bandwidth is further improved. The microstrip line-fed aperture-coupled microstrip antenna uses two substrates separated by a ground plane (Fig.(3.3 e)). The antenna element is printed on the upper substrate and is excited through a small aperture by the microstrip feed line on the bottom. In Fig.(3.3 f) the coplanar waveguide-fed slot-coupled microstrip antenna is presented. Only two metallization layers are needed with a substrate layer in between. Modified proximity-coupled, aperture-coupled and slot-coupled feeds allow independent optimisation of the feed and the radiation. The feed lines are terminated with an open stub. With proximity and aperture-coupling, a thin substrate can be used for the feeding line and a thicker substrate for the antenna to improve bandwidth. The aperture is smaller than the resonant size and the backlobe radiation is typically 15-20 dB below the main beam (Pozar, 1992). At least four parameters can be altered to optimize the antenna performance when modified proximity-coupled, aperture-coupled or slot-coupled feed is used: slot length and width, slot position related to the antenna element and the feed line width. The substrate material is uniform when LTCC technology is used. By choosing a different substrate material for the microstrip feed line and the antenna element, proximity and aperture-coupled feeds would have a fifth parameter for the design. Although being beneficial, more degrees of freedom of proximity-, aperture- and slot-coupled feeds leads to more complicated structures. The fabrication is more difficult and they require high manufacturing tolerances.

### 3.4 Design process of microstrip antennas

Before starting to design an antenna, specifications or requirements that the antenna has to fulfil have to be taken into account. Usually, there is no ideal solution but compromises have to be made. For example, at millimetre-wave frequencies relatively thick substrates compared to the wavelength have to be used. An increase in the substrate thickness leads to a broader impedance bandwidth but the gain is reduced due to increased surface wave power. Small permittivity of the substrate material is preferred to maximise bandwidth and gain (Pozar, 1992) but usually substrate material depends on the manufacturing technology and is not alterable. For the aperture- and slot-coupling feeds, a small coupling area is desirable to minimise back radiation but the manufacturing tolerances may restrict the feeding mechanism dimensions.

There is no universal mathematical method to determine the geometry of an antenna based on specific requirements and the design process of the antennas is done

through analysis (Lindell & Nikoskinen, 1995): an antenna geometry is constructed and radiation pattern, input impedance etc. are calculated for that structure. Then, the parameters or dimensions of the antenna are altered until the desired properties are achieved. The transmission line, the cavity and the full-wave models are used to analyse microstrip antennas. The transmission-line model is simple but the most inaccurate. The antenna element is thought as a line resonator with no transverse field variations (Kumar & Ray, 2003). The transmission-line model is useful when defining initial parameters for the antenna in the design process. In the cavity model, the antenna element and the ground plane form the electric walls of the cavity (Balanis, 1997). The substrate in between is enclosed with magnetic walls. The cavity model is quite accurate if a thin substrate is used (Pozar, 1992). The full-wave model is the most accurate but also the most complex. Nowadays, a lot of commercial software is available for full-wave numerical analysis. In this work, *Method of Moments* (MoM), *Finite Element Method* (FEM) and *Finite-Difference Time-Domain* (FDTD) method were used to model, design and simulate microstrip antenna structures.

### 3.4.1 The design using the transmission-line model

An antenna is printed on a substrate which usually has the relative permittivity  $\epsilon_r > 1$ . The electric field exists in the substrate and also in air. The relative permittivity, or the dielectric constant, can be replaced with an effective dielectric constant  $\epsilon_{reff} > 1$ . The effective permittivity is the permittivity of a uniform dielectric material at which the microstrip line or antenna has identical electrical characteristics. The effective dielectric constant can be calculated from the following equation if  $w_p/h_p \geq 1$ , which is usually the case with the microstrip antennas (Lehto & Räsänen, 2002b),

$$\epsilon_{p,reff} = \frac{\epsilon_r + 1}{2} + \frac{\epsilon_r - 1}{2} \frac{1}{\sqrt{1 + 12h_p/w_p}}. \quad (3.2)$$

In the equation (3.2),  $\epsilon_{p,reff}$ ,  $w_p$  and  $h_p$  denote the effective dielectric constant of the substrate, the width of the microstrip patch and the thickness of the substrate, respectively (see Fig. (3.4)). The substrate height is usually between  $0.003\lambda_0 < h_p < 0.05\lambda_0$  (Balanis, 1997). Initial value for the width can be estimated from the operating frequency,  $f_o$ , to be for example  $w_p = c_0/(3f_o\sqrt{\epsilon_r})$  to prevent higher order modes from arising. Ends of the antenna element cause fringing of the fields and electric length of an antenna is bigger than its physical length,  $l_p$ . Fringing can be taken into account by defining the effective length,  $l_{p,eff}$ , which is a sum of extended



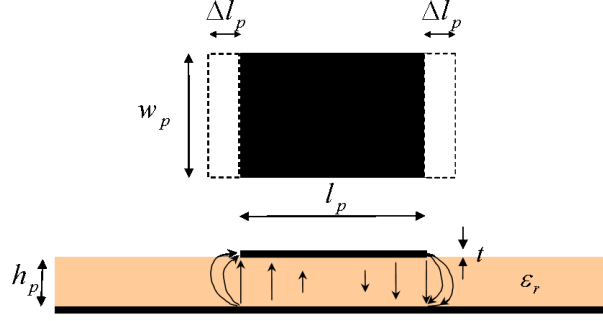


Figure 3.4: Physical and effective dimensions of a rectangular microstrip antenna. Arrows below the antenna element represent electric field lines.

lengths,  $\Delta l_p$ , and the length of the antenna element

$$l_{p,eff} = l_p + 2\Delta l_p, \quad (3.3)$$

where (Lindell & Nikoskinen, 1995)

$$\Delta l_p = 0.412h_p \frac{\epsilon_{p,reff} + 0.300}{\epsilon_{p,reff} - 0.258} \frac{w_p + 0.262h_p}{w_p - 0.813h_p}. \quad (3.4)$$

The length of the patch can be calculated as

$$l_p = \frac{1}{2f_o \sqrt{\mu_0 \epsilon_0 \epsilon_{p,reff}}} - 2\Delta l_p. \quad (3.5)$$

Equations (3.2)-(3.5) can be used to estimate starting values in the design. However, they do not take into account the dispersion (dependency on the frequency) or the metallization thickness. Parameters can be optimised further with a simulation software to obtain desirable radiation and impedance characteristics.

### 3.5 Full-wave modelling of the microstrip antennas

Nowadays, the computer power and software capabilities enable accurate, complete and fast antenna design using numerical full-wave modelling methods such as the method of moments (MoM), the finite element method (FEM) and the finite-difference time-domain (FDTD) method. In this Section, the basic ideas of these methods are presented. Also, some comparison is done between commercial software used in this work. For more information about MoM, FEM and FDTD, see for example (Harrington, 1968), (Volakis *et al.*, 1998) and (Taflove & Hagness, 2000).

### 3.5.1 Method of moments

Method of moments can be used to solve several linear electromagnetic problems. It is widely used also for modelling of microstrip antennas. MoM was introduced by Roger Harrington in 1967 (Lindell & Nikoskinen, 2003). Formulation of MoM can be an integral equation (IE) or a differential equation (DE). In MoM, the unknown currents are solved on metallic parts of the structure. With microstrip antennas, integral equations of form (2.6) or (2.9) are formulated for the unknown electric currents on the antenna element, feed lines and their images (Newman & Tulyathan, 1981).

The commercial MoM software package IE3D version 11.11 by Zeland Inc. was used in this work. IE3D also uses integral equations obtained through the use of Green's functions (Zeland, 2004). First, an incident field is imposed to the structure and a current distribution is induced. Current creates electric and magnetic fields, according to equations (2.6) and (2.9), which satisfy the boundary conditions on the metallic structure and material boundaries. For numerical computation, the current is discretised and represented by a finite number of basis functions, which is an approximation of an infinite set. This creates an error term for the solution. The error term is minimised in a specific manner. The minimisation is done by taking a set of weight functions and demanding their moment, or inner product, with the error term to be zero (Lindell & Nikoskinen, 2003). In IE3D, Galerkin's procedure is used where basis and weight functions are chosen to be the same. From the moment equation, the unknown currents in the antenna structure can be solved. After the current distribution of the antenna is known the S-parameters, radiation patterns or other parameters of interest can be solved.

IE3D is a very powerful tool for planar antenna and circuit geometries. In earlier versions, dielectric layers could only be modelled having infinite widths. IE3D version 11.11 is capable of using finite shapes and widths for the dielectric layers. Also, the metallization thickness can be taken into account.

### 3.5.2 Finite element method

The finite element method belongs to a class of partial DE methods. The FEM was first described by Richard Courant in 1943 (Volakis *et al.*, 1998). In FEM, the calculation space is divided into the finite number of surfaces or volumes depending on the structure to be analysed. These small discretised area or volume units are typically triangles or tetrahedra and bear the name *finite elements*. The elements are associated with shape or basis functions. The collection of elements with basis functions

allows modelling of complex fields in three-dimensional structures. Thereby, FEM is not only suitable for electromagnetic modelling of microstrip antennas, but for all kinds of three-dimensional structures. The equations for the unknown coefficients of the basis functions are determined by solving a wave equation for the electric field in a structure (Volakis *et al.*, 1998). The commercial software Ansoft HFSS version 8.0.22 by Ansoft Corporation was used in this work to model microstrip antennas with FEM.

In HFSS, the field quantities inside the tetrahedra are interpolated from values at vertices. At each vertex, the components of the field that are tangential to the three edges of the tetrahedron, are stored. In addition, the component of a field that is tangential to the face of an element and normal to an edge is explicitly stored at the midpoint of selected edges (Ansoft, 2001). The value of a vector field at an interior point is interpolated from these nodal values. The basis functions are essentially the interpolation schemes used to calculate field values inside the tetrahedra.

Since HFSS calculates the electric and magnetic fields all over the calculation space, field visualisations and animations can be obtained besides S-parameters, radiation pattern or other characteristics. Field visualisations give the designer useful information about the electromagnetic behaviour of the structure. For example, polarisation of the antenna can be investigated with vector field illustrations.

### 3.5.3 Finite-difference time-domain method

MoM and FEM are spectral domain techniques which calculate field solutions at specific frequencies. Frequency sweep for S-parameters is done using interpolation. In the finite-difference time-domain method, FDTD, Maxwell's curl equations (2.1) and (2.2) are solved in three- two- or one-dimensional discretised rectangular grids using the finite-difference expressions of the time-dependent fields. Problem's geometry and boundary conditions are built into the calculation grid. FDTD was introduced by Kane S. Yee in 1966 (Yee, 1966). In FDTD, ultra-wideband frequency response or the sinusoidal steady-state response at any frequency can be calculated with a single run (Taflove & Hagness, 2000). The frequency range depends on the spectrum of an input signal. The S-parameters are calculated using the Discrete Fourier-Transform (DFT) for the time-dependent fields. The radiation pattern is usually calculated at few specific frequencies because of limitations of computer memory (Nikoskinen & Kärkkäinen, 2004).

FDTD is mathematically simple and does not use linear algebra, so large problems can be solved with FDTD (Taflove & Hagness, 2000). FDTD is accurate and robust

because the sources of error are well understood and can be avoided. FDTD can be extended to dispersive, non-linear, unhomogenous and non-isotropic materials (Nikoskinen & Kärkkäinen, 2004) and it provides also the visualisation of time-dependent fields. Field animations of time-stepped arrays of field quantities give valuable information of the field dynamics in the structure. The rectangular grid is not a problem with rectangular microstrip antenna structures but geometry has to be adjusted to the chosen grid or vice versa. If a non-uniform grid can be used, the structure can be modelled with more realistic dimensions.

In addition to simulations with IE3D and HFSS, an FDTD code was implemented by the author with MATLAB 7.0.1 from Mathworks for calculating the  $S_{11}$ -parameters and the input impedance for designed antenna structures. More detailed description of the three-dimensional FDTD MATLAB code is given in Chapter 6.

#### 3.5.4 Comparison between MoM, FEM and FDTD software

Different full-wave modelling software can be compared considering the following characteristics: accuracy, efficiency and utility (Yee, 1988). Accuracy of the software is revealed when simulation and measured results are compared with each other. Efficiency can be considered in terms of the CPU (central processing unit) time and the preparation time. The CPU time is the time that the software takes to run a simulation. Preparation time is time of human effort to build a simulation setup or to implement a simulation code. Utility is a measure of how well the software models the real structure. Utility also relates to ease of use. Utility is important because commercial software is usually quite expensive and is needed for modelling of different kinds of electromagnetic problems. Also, if the user interface is poor the software does not get much support among designers and is useless.

The IE3D (MoM) is a so-called 2.5D software which is well-suited for the microstrip antenna modelling. The preparation time is short and, if infinite widths are used for substrate and ground planes, the CPU time is very short. The finite ground plane does not have so large effect but, if finite substrate width is used, the CPU time increases rapidly. The IE3D is well-suited to get a draft model of the desired structure. It also enables fast tuning and sensitivity analysis i.e. finding limits of design parameters in order to maintain the proper operation of an antenna.

HFSS (FEM) is a general 3D software which is suitable also for the planar microstrip antenna structures. But, HFSS often requires very large number of tetrahedra or triangles and its CPU time is quite long, about 10-15 times longer than for IE3D (Pozar *et al.*, 2000). But, the CPU time can be reduced significantly if symmetry

planes can be used in the structure. The preparation time is higher than in IE3D. In HFSS 8.0.22 tuning of the structures is practically impossible because of difficult user interface. Major benefit of HFSS is that it is very versatile for modelling all kinds of passive structures. Overall utility of the software is quite good because the real operating environment of the structure can be taken into account although the usability could be better.

The implementation of the FDTD MATLAB code is relatively fast. The most challenging problem is to be aware of the matrix indices related to the geometry of the structure when defining finite-difference expressions and the boundary conditions for the fields. CPU time is long and could be reduced with more careful preparation of the code.

When state of the art personal computer is used "short" and "long" computer times are in order of minutes and tens of minutes for the microstrip antenna structures.

## Chapter 4

# LTCC technology

### 4.1 LTCC-what is it?

Low Temperature Co-fired Ceramic (LTCC) is a multilayer platform technology that is nowadays used in fabrication of components, modules and packages in wireless, automotive, military, medical and several other areas. LTCC enables the integration of passive components, such as filters and antennas, in a same package up to millimetre-wave frequencies. Components can be placed in different layers (even up to 70 layers), and three-dimensional integration enables miniaturisation of modules. LTCC processing enables cavities and conducting vias to be placed inside the substrate. Major benefits of LTCC are low conductor and dielectric losses, good thermal conductivity, stability, hermeticity, and cost efficiency. Disadvantages are related to the fabrication tolerances at millimetre-wave region.

### 4.2 LTCC fabrication process

The LTCC package is formed by layered dielectric glass/ceramic sheets or tapes on which the metallizations have been manufactured using the screen-printing or the photoimaging technologies. The LTCC fabrication process is described in Fig.(4.1). First, via holes are punched in the "green" glass/ceramic sheets. Then, via holes are metallized to form electrical interconnection between layers. As a third step, the metallizations of electrical conductors and passive components are fabricated on each glass/ceramic sheet separately. Then, different layers are aligned and laminated. After lamination, the ceramic sheets are *co-fired* or *sintered* together with conductors. Finally, the circuits are separated. Sometimes etched conductors can be *post-fired* on the top after the LTCC processing. In LTCC, glass/ceramic sub-

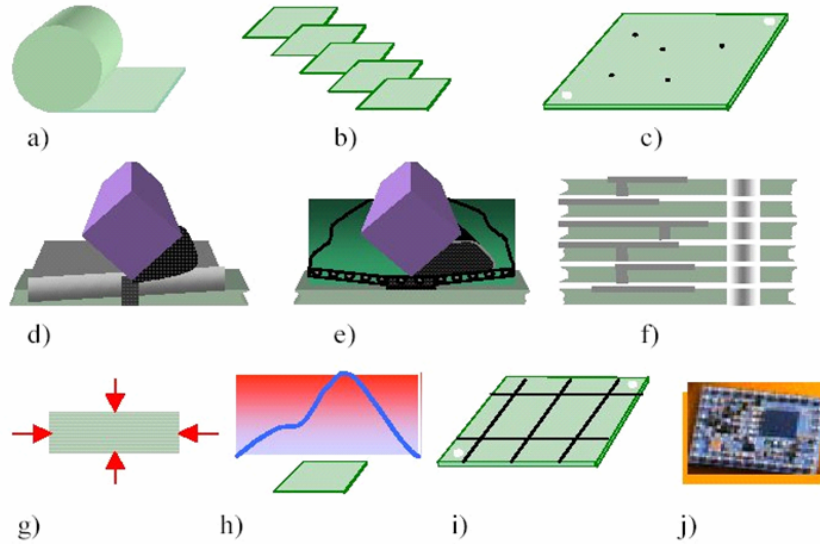


Figure 4.1: The LTCC process: a) glass/ceramic LTCC tape material, b) tape blanking, c) via punching, d) via metallization, e) conductor printing (or photoimaging), f) layer alignment and stacking, g) lamination, h) sintering, i) dicing of fired panel, j) component and die attach. (Obtained from VTT Electronics).

strates have sintering temperatures below  $900^{\circ}\text{C}$  while the alumina substrate used in HTCC (High Temperature Co-fired ceramic) requires a temperature of  $1600^{\circ}\text{C}$  for sintering. Low sintering temperature of LTCC enables co-firing of substrate with gold and silver conductors which have melting points  $960^{\circ}\text{C}$  and  $1100^{\circ}\text{C}$ , respectively (Kulke *et al.*, 2005). When compared to conductors with high melting point, such as tungsten or molybdenum, used in HTCC, silver and gold have higher conductivities which result in a lower conductor loss in LTCC.

During the sintering, the ceramic sheets shrink because of the binding of ceramic ingredients near the sintering temperature. There are two co-firing methods that are used in practise: 1) *free sintering* and 2) *zero-shrinkage*. Shrinkage values for these two methods in  $x$ -,  $y$ - and  $z$ -dimensions are given in Table (4.1). Shrinking has to be taken into account in the LTCC process. Nowadays, the LTCC processing for 60 GHz frequency band applications is being developed and processing has not been standardised yet. Exact values of shrinking of the glass/ceramic sheets and metallizations is quite difficult to predict because the lack of processing repetitions. Especially, as conductor widths or spacings are in the order of the minimum values that can be processed, the predicting of realised dimensions of the structures becomes even more difficult.

Table 4.1: Shrinking in the LTCC sintering process.

Dimension	Free sintering	Zero-shrinkage
$z$	$(\approx 15 \pm 0.5\%)$	$(\approx 45 \pm 0.4\%)$
$x$ or $y$	$(10\dots 15 \pm 0.2\%)$	$(0\dots 0.3 \pm 0.03\%)$

### 4.3 LTCC materials

Several commercial LTCC tapes are available for high-frequency applications. Traditional materials can be used in free-sintering up to millimetre-wave frequencies. With more advanced materials the zero-shrinkage processing is possible. Material information of the commercial LTCC tape systems is presented in Table (4.2) (Obtained from (VTT Electronics, 2005b)). Ferro A6-S/A6-M is currently the best commercial LTCC system available for the millimetre-wave applications and the Ferro A6-S was used in this work as substrate material for the 60 GHz antennas. Ferro A6-S has a low dielectric loss ( $\tan \delta = 0.0015$ ) and silver or gold conductors with high conductivities can be used (for example  $\sigma_{Ag} = 7.4 \cdot 10^6$  S/m) which results in a low conductor loss also. The dielectric constant for the Ferro A6-S was defined with ring-resonator measurements and the value  $\epsilon_r = 5.99$  was used in design. Fired, or final, thickness for Ferro A6-S is  $\sim 100\mu\text{m}$ . Thus, discrete values,  $100\mu\text{m}$ ,  $200\mu\text{m}$ ,  $300\mu\text{m}$ ,  $\dots N \cdot 100\mu\text{m}$ , for the substrate thicknesses are possible.

### 4.4 Conductor patterning in LTCC

At millimetre-wave region narrow conductor lines and spacings are needed. Several methods have been developed for conductor patterning. In this Section, *screen printing*, *photoimaging* and *etching* technologies used also in LTCC processing are introduced.

In the traditional screen-printing technology films are printed on the substrate in a desired pattern. Conductor paste is pressed on the substrate through printing screen (see Fig.(4.2)) using a comb or a squeegee. Printing screen is covered with a mask at which the conductor pattern is left open. Conductor paste is formed by mixing small particle size metal powder with solvents and glass binders. The printing screen is formed by a tense mesh of metal wires, usually stainless steel. The minimum conductor line width is about three times the mesh wire diameter and



Table 4.2: Commercial LTCC material data.

	DuPont 951-AX	Ferro A6-S	DuPont 943	Heraeus CT 2000
dielectric constant	7.8	$5.9 \pm 0.15$	7.5	$9.1 \pm 0.1$
green thickness ( $\mu\text{m}$ )	254	127	127	99
fired thickness ( $\mu\text{m}$ )	205	99	105	77
$\tan \delta$	0.0055 (>1 GHz)	0.001 (>1 GHz)	0.002 (>1 GHz)	0.0027 (>1GHz)
insulation resistance	$> 10^{12} \Omega\text{cm}$ (100 VDC)	$> 10^{14} \Omega\text{cm}$ (bulk resistivity)	N.A. N.A.	$> 10^{13} \Omega\text{cm}$ (bulk resistivity)
breakdown voltage	$> 1000\text{V}/25\mu\text{m}$	$> 5000\text{V}/93\mu\text{m}$	N.A.	$> 1000\text{V}/25\mu\text{m}$
colour	blue	white	blue	white
thermal conductivity	3 W/mK	2 W/mK	3 W/mK	N.A.
thermal expansion	5.8 ppm/K (25...300) $^{\circ}\text{C}$	7 ppm/K (25...300) $^{\circ}\text{C}$	5.3 ppm/K (25...300) $^{\circ}\text{C}$	8.5 ppm/K (25...300) $^{\circ}$
fired density	3.1 g/cm <sup>3</sup>	2.5 g/cm <sup>3</sup>	3.2 g/cm <sup>3</sup>	3.05 g/cm <sup>3</sup>
flexural strength	320 MPA	$> 210$ MPA	N.A.	240 MPA
shrinkage: z-axis	$(15 \pm 0.5)\%$	27%	13%	14%
x-, y-axis	$(12.7 \pm 0.2)\%$	$(15.5 \pm 0.2)\%$	10%	11.5%

the mesh opening should be three times the particle size of the paste. This means that for  $50\mu\text{m}$  lines the wire diameter should be  $18\mu\text{m}$  or less (VTT Electronics, 2005a). The so called *trampoline* printing screen is formed by a stainless steel mesh

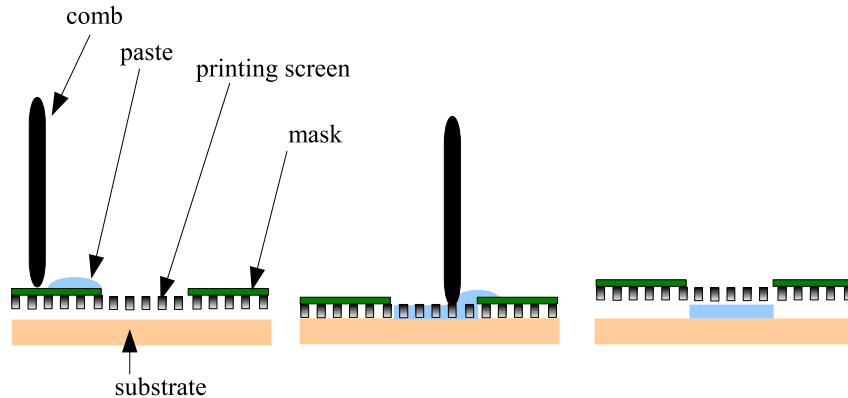


Figure 4.2: Screen-printing technique.

together with a polymer mesh. The screen is strained between the screen frames to obtain good quality for the conductors. Due to elastic polymer fabric used in the trampoline screen the screen tension can be increased without damaging the metal wire screen. The illustration of the trampoline screen is presented in Fig.(4.3). Using the Ferro LTCC system  $75\mu\text{m}$  line width and spacing is achievable with screen printing and even line width and spacing of  $50\mu\text{m}$  have been reported. Numerous factors affect the screen-printing quality but the most important ones are the screen and paste properties. In this work, the conductors and the antenna metallizations were fabricated using a trampoline printing screen.

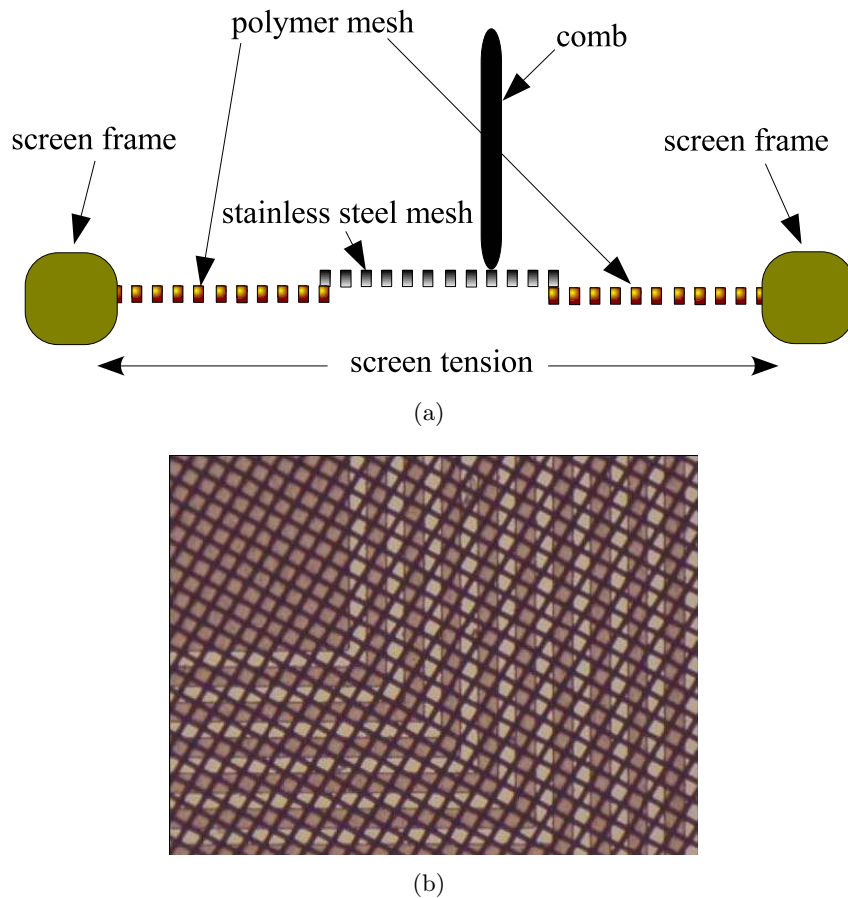


Figure 4.3: Trampoline screen: a) a sketch and b) a realised (500 mesh,  $18\mu\text{m}$  wire diameter and  $32\mu\text{m}$  opening). ((b) obtained from (VTT Electronics, 2005a).)

With photoimaging even smaller conductor line width and spacing can be achieved. The photoimaging technique uses photosensitive thick-film paste materials and feature sizes of  $50\mu\text{m}$  and even smaller can be achieved on the outer substrate surfaces. However, for the Ferro A6-S only post-fire photo-patternable pastes are available

and photoimaging was not used for conductor patterning in this work. Photoimaging for the inside layers is possible for the DuPont 951 LTCC system.

The etching can also be used as conductor patterning of the outer conductors of the LTCC substrate. First, metallization is placed on the surface. Then metallization is covered with photoresist and dried in the oven. As a third step, a mask on which the conductor patterns are formed is placed on the photoresist and metallization. Then the mask is exposed by ultraviolet light and photoresist is etched away from the unexposed parts. Finally, the photoresist is removed (Lehto & Räsänen, 2002b). The conductor width and spacing of  $25\mu\text{m}$  is achievable with etching. However, if etching is used post-firing of metallization is required and it can be used only on the outer surfaces of the substrate.

## 4.5 Layer-to-layer alignment, vias and cavities

The screen-printed conductor alignment error is typically  $5\text{--}10\mu\text{m}$  and over  $20\mu\text{m}$  errors are possible on large tape areas. Also, the lamination process of the tape sheets produces some alignment error. Possible misalignment of tape layers and conductors has to be taken into account in design.

Sometimes vias are used to form conducting walls in LTCC waveguides, or just to obtain electric contact between two layers. Via sizes are dependent on the tape thickness. Typically, the via diameter range is  $100\mu\text{m}\text{--}200\mu\text{m}$ . The minimum via to via pitch within the same tape layers should be  $\sim 2.5\times$  via diameter. If silver paste is used for conductors, then pure silver is used for vias. Thermal management of LTCC substrate can be done using thermal vias. A thermal via is fabricated as electrically conducting vias by filling the via holes with conductor with high thermal conductivity like silver. Thermal via goes completely through the substrate and is placed near the component that produces the high amount of heat.

The LTCC process enables the use of air cavities inside the substrate. The cavity is formed just like via holes by punching the cavity hole to the individual tape sheets before lamination and firing. Cavities can be useful in some applications; for example if particular electrical characteristics are needed by controlling the effective dielectric constant of the substrate. Cavities can also be used in thermal management, for example, in forming a liquid cooling channel inside the substrate (Fig.(4.4)).

The current status and future trends of LTCC processing are presented in Table(4.3). Information in the table is based on the experience of LTCC processing at VTT Electronics. It is seen that electrical via dimensions and conductor line and spacing will

be diminished in future. Submicron structures become more common and passive components with lower loss and smaller sizes will be achievable. Conducting layers and special cooling channels will become more common due to dense packaging of components.

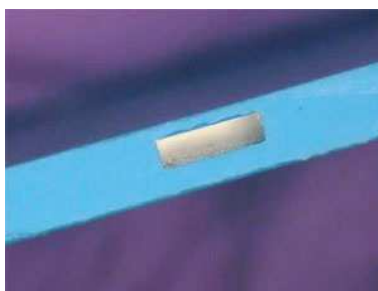


Figure 4.4: A water cooling channel in the LTCC substrate, cross section 0.4 mm×1.5 mm. (Obtained from VTT Electronics.)

## 4.6 Microstrip antennas on LTCC

In this Section, the literature concerning recent work on LTCC antennas and arrays is resumed. For further information the reader is encouraged to see the references in more detail.

LTCC is well-suited for fabrication of planar structures. Microstrip antennas are widely used at microwave and millimetre-wave regions. Due to poor gain of the patch, usually several antenna elements are placed in an array. Phased array consisting of four microstrip antennas using probe- and proximity-coupled feeds have been designed for 20 GHz frequency band on LTCC and integrated with transmitter radio module (Sturzebecher *et al.* , 1996). The 256-element microstrip antenna array at 29 GHz on LTCC have been investigated by (Huang *et al.* , 2005). They used *quasi-cavity-backed patch* (QCBP) elements and mixed feeding network consisting of microstrip lines and low-loss laminated waveguides. Using QCBP instead of the traditional patch element the efficiency is enhanced due to minimised surface-wave loss. Laminated waveguides provide low loss and minimum leakage but structure requires high amount of vias which are used to represent side walls of the waveguides. The developments in LTCC and active circuit technologies have increased the interest of exploiting higher millimetre-wave frequency bands. LTCC enables multilayered structures and this feature has been utilised by (Seki *et al.* , 2005). They used 2×2 antenna elements in three layers fed by single patch element on the bottom layer resulting in a 9-element array. The structure is very compact but beam steering is

Table 4.3: Current status and future trends of LTCC at VTT.

Issue	Current state in production (at VTT)	Future trend
Electrical via diameter/pitch	100 $\mu$ m/200 $\mu$ m	50 $\mu$ m/100 $\mu$ m
Conductor line width/spacing	100 $\mu$ m/100 $\mu$ m (screen printed) 50 $\mu$ m/50 $\mu$ m (photo patterned)	50...75 $\mu$ m/75 $\mu$ m (screen printed) 30...40 $\mu$ m/40 $\mu$ m (photo patterned)
Number of layers	up to 70	Combination of different materials, few layers with fine-line additive redistribution layers
Alignment structures	grooves, holes, bumps, cavities, spacers	Photopatterned submicron structures
Alignment structure tolerances	$\pm 5\mu$ m/ $\pm 3\mu$ m (machined/ photopatterned) on the surface layer layer-to-layer 10 $\mu$ m	Sub-micron structures, dynamic fine-adjustment of device position
Embedded passive components (R,L,C)	Buried and on-surface passives R: 10 $\Omega$ ...100M $\Omega$ $\pm$ 30%, trimmed 1% C: <10 pF $\pm$ 5% ( $\pm$ 5% demonstrated) L: <200 nH/layer $\pm$ 5% (1 $\mu$ H demo)	Lower loss, smaller size  higher capacitance (high k materials) higher inductance (ferrite materials)
Optical via	Free space (through hole), fiber stud	Glass waveguide
Optical waveguides	Post-fired polymer and sol-gel structures	Loss loss pre-fired glass waveguides, active waveguide structures
Dielectric constant	5.9...9.1 (7.8 common)	
Dielectric loss tangent	0.001 (at 1 MHz), 0.001...0.005 (at > 1GHz)	
Thermal conductivity and via	2...3 W/mK (10...15 $\times$ FR-4), with vias 100 $\times$ better than FR-4	Heat conducting layers, cooling channels
CTE (compatibility)	5...7 ppm/K (excellent with GaAs & InP, 2 $\times$ of Si)	
Operation temperatures	Limited by devices & bonds	
Hermetic sealing	Glass-metal & metal-metal junctions, solder sealing	Passive optical elements embedded into the substrate

not possible due to only one feeding point. For the same reason the feed power of the array may not be adequate because of the rather low-gain amplifiers at 60 GHz frequency band.

In this work, antenna elements are designed on LTCC for 60 GHz frequency band. In the near future, the elements are formed in a steerable-beam array with individual feeding mechanisms. The subsequent Chapters concentrate on the design and testing of antenna elements on the Ferro A6-S LTCC substrate.

## Chapter 5

# Antenna design

Different feeding mechanisms of microstrip antennas were presented in Section 3.3. Proximity (PC)- aperture (AC)- and slot-coupled (SC) microstrip antennas offer more degrees of freedom for the design than microstrip- or probe-fed patches. PC, AC and SC feeds are also well-suited for the layered LTCC manufacturing process and these feeding mechanisms were selected for the design and fabrication. In this Chapter, the developed antenna configurations are presented. First, issues related to the antenna element design are described and then detailed information about the feeding mechanisms of the patches is presented. In order to test the antennas, i.e. to conduct the  $S_{11}$ -parameter and radiation pattern measurements, some modifications to the basic structures had to be made. The end of the Chapter concentrates on these modified antenna structures.

### 5.1 Microstrip antenna element

There was no specification determined for the performance of the antenna and many parameters were given as the designer to decide. The rectangular antenna element was chosen which provides linear polarisation. One important thing when designing a microstrip antenna is the radiation efficiency-bandwidth relationship. As was mentioned in Section 3.2, the thicker substrate leads to a broader bandwidth but gain is reduced. The substrate thickness for the antenna element was decided based on a graph by Pozar (Pozar, 1992) at which the bandwidth and efficiency is presented as functions of the substrate thickness/wavelength in free space and the dielectric constant. For the chosen value for the substrate thickness,  $h_p = 300\mu\text{m}$ , the radiation efficiency should be  $\sim 60\%$  and bandwidth  $\sim 5\%$  at 60 GHz. Starting values for the antenna element dimensions are computed using equations (3.2) - (3.5). For

the patch width  $w_p = 0.68$  mm and substrate thickness  $h_p = 300\mu\text{m}$  the effective dielectric constant is  $\epsilon_{p, \text{eff}} = 4.49$ . The extended length of the patch is  $\Delta l_p = 0.243$  mm and the length of the patch yields  $l_p = 0.69$  mm.

The complex input impedance of the microstrip antenna varies as a function of frequency. The microstrip antenna can be considered as a resonator which is an equipment where energy is stored endlessly in forms of electric and magnetic fields if no losses occur. In microstrip antennas the resonance occurs at a frequency where input resistance reaches its maximum and input reactance is equal to the average sum of its maximum and minimum values (Balanis, 1997) (see Fig.(5.1)). The resonance frequency is tuned to a specified operating frequency. The resonance frequency is determined mainly by the patch length  $l_p$ . The characteristic impedance of a microstrip line increases as the ratio  $h_p/w_{ms}$  increases (see Section 5.2.1), so the width of the patch,  $w_p$ , has an effect on the antenna input resistance. The input impedance should be matched to the characteristic impedance of the feed line to prevent reflections. The effects of the patch length and width on the input impedance was investigated with simulations and results are shown in Fig.(5.1) and Fig.(5.2). It seems that resonance frequency shifts 5 GHz and input resistance increases  $20\Omega$  as the patch length is increased by 0.1 mm. There is only small changes in the input resistance and reactance values as the width is altered by 0.1 mm. The effect on the resonance frequency is also negligible. Patch dimensions  $l_p = 0.75$  mm and  $w_p = 0.79$  mm was used for the ACMPA, and  $l_p = 0.74$  mm and  $w_p = 0.79$  mm for the SCMPA in manufacturing.

## 5.2 Aperture-coupled microstrip patch antenna

The aperture-coupled microstrip patch antenna (ACMPA) uses microstrip line as a feed line and the antenna element is excited by the aperture-coupling (see Section 3.3). It was mentioned that the ACMPA has several advantages compared to the microstrip line- or probe-fed patches and the ACMPA was chosen to be designed and manufactured and tested.

The ACMPA uses three metallization and two substrate layers. From the bottom to top there is first the microstrip feed line, the substrate of the microstrip line and the ground plane common with the antenna element. An aperture is cut into the ground plane. Above the ground plane is the patch substrate layer and the patch metallization on the top. The ACMPA geometry used in this work is illustrated in Fig.(5.3).



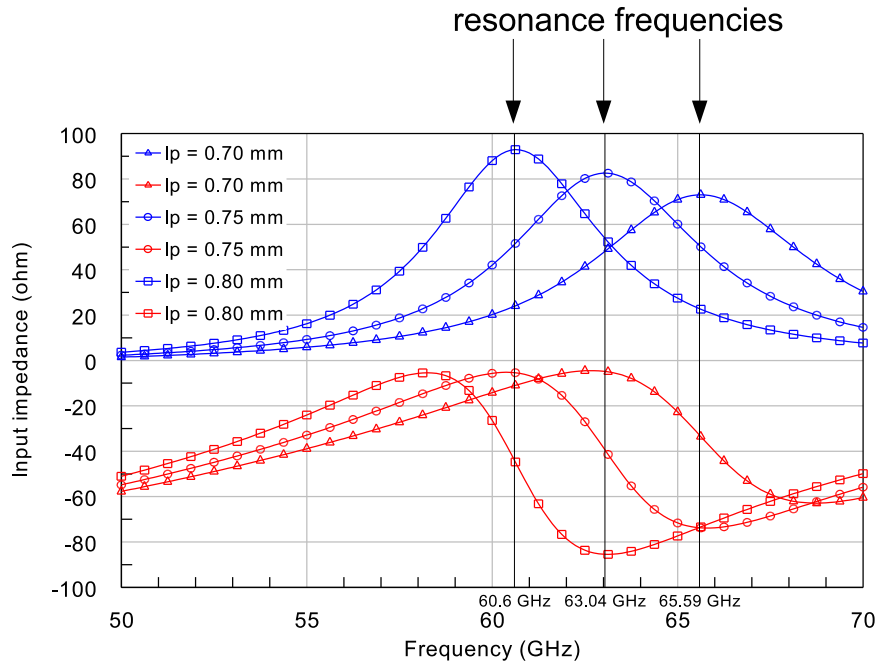


Figure 5.1: The effect of the patch length on the input resistance (blue) and reactance (red) ( $w_p = 0.75$  mm,  $h_p = 0.3$  mm,  $\epsilon_r = 5.99$ ). Simulated with IE3D (MoM).

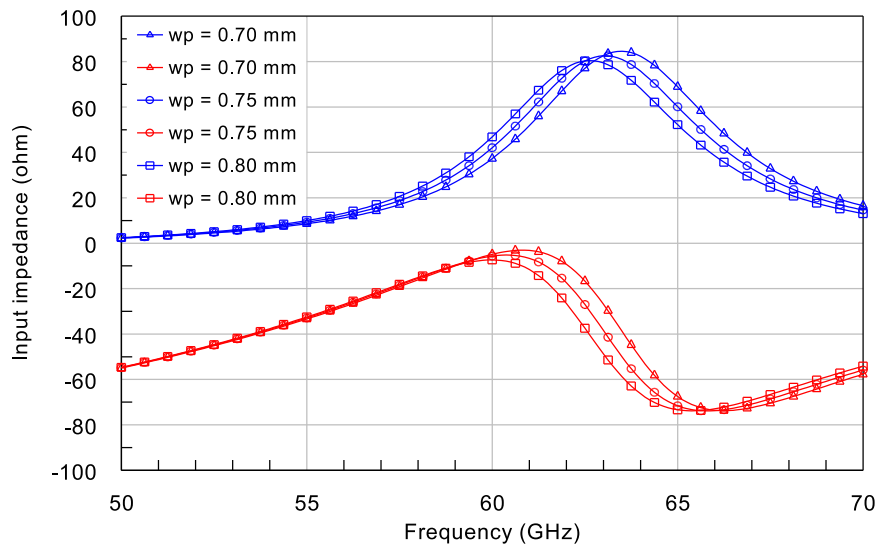


Figure 5.2: The effect of the patch width on the input resistance (blue) and reactance (red) ( $l_p = 0.75$  mm,  $h_p = 0.3$  mm,  $\epsilon_r = 5.99$ ). Simulated with IE3D (MoM).

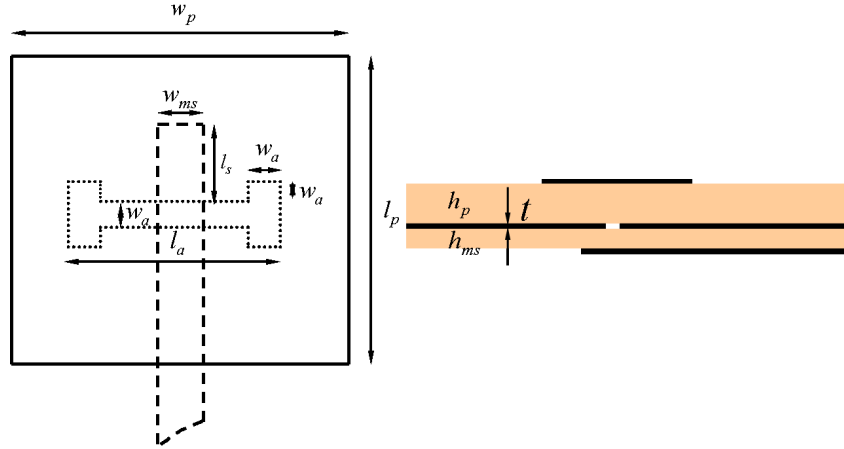


Figure 5.3: Geometry of the ACMPA:  $w_{ms}$ =width of the microstrip line,  $w_p$ =width of the patch,  $l_p$ =length of the patch,  $l_{ap}$ =length of the aperture,  $w_{ap}$ =width of the aperture,  $l_s$ =stub length,  $h_{ms}$ =microstrip line substrate thickness,  $h_p$ =antenna element substrate thickness and  $t$ =metallization thickness.

### 5.2.1 Microstrip line parameters

The aperture coupling provides independent optimisation of the feeding mechanism and the antenna element. It was known beforehand that the Ferro A6-S substrate material used in the LTCC process has the relative dielectric constant  $\epsilon_r = 5.99$  and the loss tangent  $\tan \delta = 0.0015$ . These parameters were defined by VTT Electronics with ring-resonator measurements. It is desirable to use thin substrates for the feed lines to minimise surface wave power and prevent higher order modes from arising. The Ferro A6-S substrate tape thickness is  $100\mu\text{m}$  and possible values for the substrate heights are  $100\mu\text{m}$ ,  $200\mu\text{m}$ ,  $300\mu\text{m}$  etc. The substrate thickness of  $100\mu\text{m}$  was chosen for the feed line. Size of the ground plane was chosen to be  $3\text{ mm} \times 3\text{ mm}$  which was tested with simulations to be large enough. The geometry of a microstrip line is presented in Fig.(5.4). The characteristic impedance,  $Z_c$ , of a microstrip line can be calculated using formula by Wheeler (Lindell, 1997).  $Z_c$  is presented in Fig.(5.5) as a function of  $h_{ms}/w_{ms}$  for different values of  $\epsilon_r$ . The metallization thickness,  $t = 10\mu\text{m}$ , is taken into account. It can be seen from Fig.(5.5) that for  $\epsilon_r = 5.99$  the ratio  $h_{ms}/w_{ms} \approx 0.7$  for  $50\Omega$  line. The line width of  $150\mu\text{m}$  was used. Loss in a microstrip line is the sum of conductor and dielectric losses. Power is also lost by radiation due to discontinuities. Formulas for calculation of conductor and dielectric losses can be found from literature, for example (Lindell, 1997), (Lehto & Räsänen, 2002b) or (Hoffmann, 1987). For  $\frac{1}{2\pi} \leq \frac{w_{ms}}{h_{ms}} \leq 2$  the

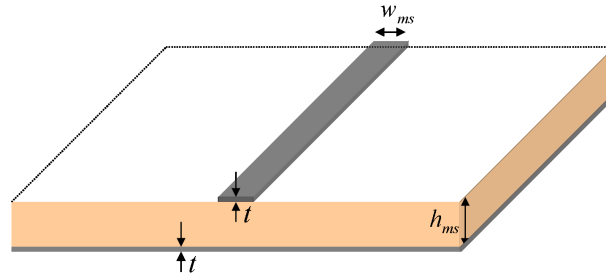


Figure 5.4: Microstrip line:  $w_{ms}$  is the width of the conductor strip,  $h_{ms}$  the substrate height and  $t$  the metallization thickness.

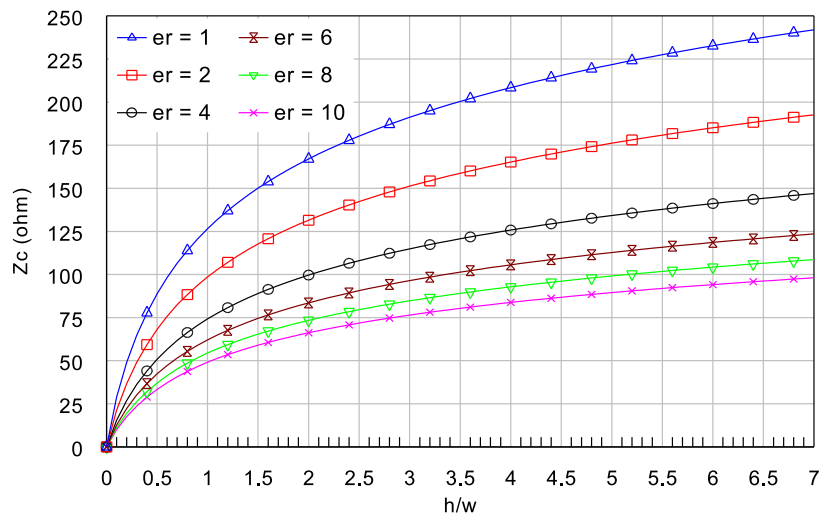


Figure 5.5: Theoretical characteristic impedance of a microstrip line.

conductor loss [dB/m] is

$$\alpha_{cms} = \frac{R_s}{2\pi Z_c h_{ms}} \left[ 1 - \left( \frac{w_{mse}}{4h_{ms}} \right)^2 \right] \left[ 1 + \frac{h_{ms}}{w_{mse}} + \frac{h_{ms}}{\pi w_{mse}} \left( \ln \frac{2h_{ms}}{t} - \frac{t}{h_{ms}} \right) \right], \quad (5.1)$$

where  $R_s = \sqrt{\pi f \mu_0 / \sigma}$  and  $w_{mse}$  is the effective width of the microstrip when metallization thickness is taken into account:  $w_{mse} \approx w_{ms} + \frac{t}{\pi} (1 + \ln \frac{2h_{ms}}{t})$ ,  $\frac{w_{ms}}{h_{ms}} \geq 0.16$ . The dielectric loss factor [1/m] can be calculated as

$$\alpha_{dms} = \frac{\pi \epsilon_r (\epsilon_{ms, \text{reff}} - 1) \tan \delta}{\sqrt{\epsilon_{ms, \text{reff}}} (\epsilon_r - 1) \lambda_0}, \quad (5.2)$$

where  $\epsilon_{ms, \text{reff}}$  is obtained using equation (3.2) with microstrip line dimensions. The conductor loss for microstrip lines having  $Z_c = 50\Omega$  and  $t = 10\mu\text{m}$  for different substrate heights as a function of frequency is shown in Fig.(5.6). Silver paste was used as metallization in the LTCC process. The electric conductivity of the paste,  $\sigma_{Ag} = 7.4 \cdot 10^6$  S/m, includes roughness correction. The roughness has to be taken into account because penetration depth at 60 GHz is  $0.75\mu\text{m}$  which is only 13 % of the metallization thickness, and the signal is transferred on the surface of the conductor. Conductor loss is proportional to the square root of the frequency. It is seen that by increasing the substrate thickness the line width and conductor loss is decreased. But, thicker substrate produces loss in a form of greater surface wave power. The Ferro A6-S is low-loss substrate material and dielectric losses are in order of 0.025 dB/cm.

It was mentioned in Chapter 4 that the LTCC process produces some misalignment errors. The effect of the microstrip line misalignment on the input impedance was investigated. The microstrip line was shifted by  $60\mu\text{m}$  in  $x$ -direction, but the aperture was kept centered below the patch. Thus, the microstrip line was shifted relative to both, the aperture and the patch. Simulation results are shown in Fig.(5.7). It is seen that the effect of the misalignment is negligible and antenna is not sensitive to the alignment tolerances of the LTCC process.

### 5.2.2 Location, size and shape of an aperture

Coupling from the aperture to the antenna element can occur via electric or magnetic field near the aperture but the coupling through magnetic case is the stronger mechanism (Pozar, 1992). The electric field under a patch is sinusoidal,  $E \sim E_z \sin(\pi y/L)$ , when the patch is centered at the origin. The electric field has a maximum at the edges of the patch, i.e. when  $y = \pm L/2$  and is zero at  $y = 0$ . Using equation (2.3) it

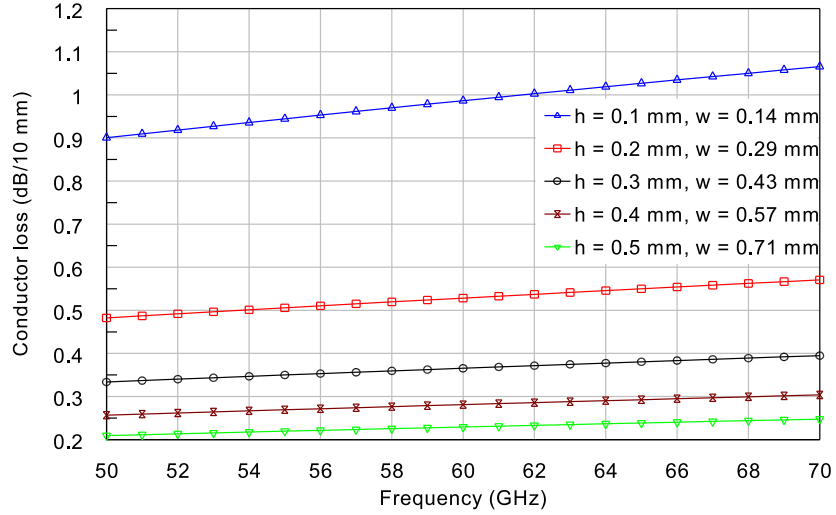


Figure 5.6: Conductor loss of a microstrip line:  $Z_c = 50\Omega$  ( $h_{ms}/w_{ms} = 0.7$ ),  $t = 10\mu\text{m}$  and  $\sigma = 7.4 \cdot 10^6 \text{ S/m}$ .

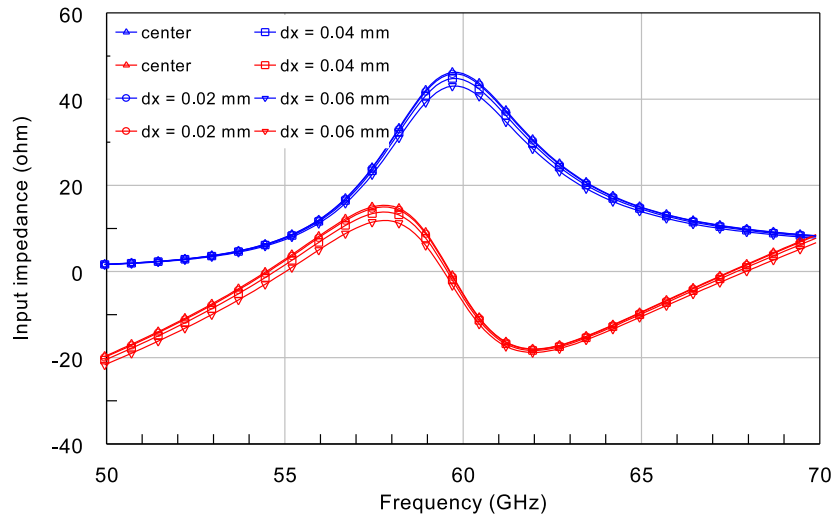


Figure 5.7: ACMPA input resistance (blue) and reactance (red) ( $\epsilon_r = 5.99$ ,  $h_p = 0.3$ , patch size:  $l_p = 0.75 \text{ mm}$ ,  $w_p = 0.75 \text{ mm}$ ): microstrip line position shifted in  $x$ -direction from the center. Simulated with IE3D (MoM).

is seen that the magnetic field under a patch is of form  $H \sim H_x \cos(\pi y/L)$  and has a maximum at  $y = 0$ . On the other hand, the electric field of the microstrip line has only  $z$ -component at  $x = 0$ , propagating towards  $y$ -direction, i.e.  $E \sim E_z e^{-jky}$  (see Fig.(5.8)). The magnetic field is of form  $H \sim H_x e^{-jky}$  and fits the magnetic field of the antenna element. The aperture is placed at the center of the patch,  $y = 0$ , where the electric field is zero and the maximum magnetic coupling is achieved.

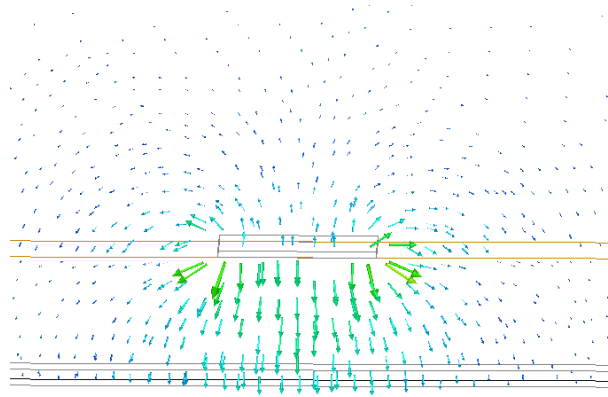


Figure 5.8: Transversal electric field distribution of a microstrip line. Simulated with HFSS (FEM).

The aperture position in the  $x$ -direction does not have strong effect on the coupling but when placing the aperture in the center also in the  $x$ -direction the excitation of the patch becomes symmetric leading to a symmetric radiation pattern.

An aperture can be considered as a magnetic dipole which is complementary to the electric dipole. The size of an aperture determines the amount of coupling. By increasing the radiating resistance, the radiated power and coupling of the aperture also increases. When short aperture is used,  $l_{ap} \leq 0.5\lambda$ , the radiating resistance increases as the length of the aperture is increased (Lindell & Nikoskinen, 1995). Changing the width of the aperture does not have strong effect on the coupling. The size of the aperture should be kept as small as possible to minimise back radiation. When the length of the aperture is kept smaller than the resonant size, the backlobe radiated by the aperture is typically 15-20 dB below the main lobe (Pozar, 1992). Size of an aperture can be minimised by choosing aperture shape in a proper way. Various shapes such as rectangular, H-shape, bowtie, or hourglass can be used as an aperture geometry (see Fig.(5.9)). The rectangular aperture is the simplest, but the length has to be bigger compared to other shapes in order to obtain the same amount of coupling. The H-shaped aperture is a modification from the rectangular

aperture and it provides more uniform field in the aperture because the electric field transversal to the longitudinal dimension of the aperture,  $E_y$ , do not have to vanish at the edges. Using bowtie-shaped aperture wider impedance bandwidth can be achieved. The hourglass shape is similar to bowtie shape but sharp discontinuities have been removed and field distribution becomes more uniform. In this work, the H-shaped aperture was chosen because of its simple geometry and its insensitivity to manufacturing tolerances of the LTCC process. Length of the aperture was kept below the half wavelength, in order of  $\lambda/4 - \lambda/3$  at 60 GHz. The input impedance of

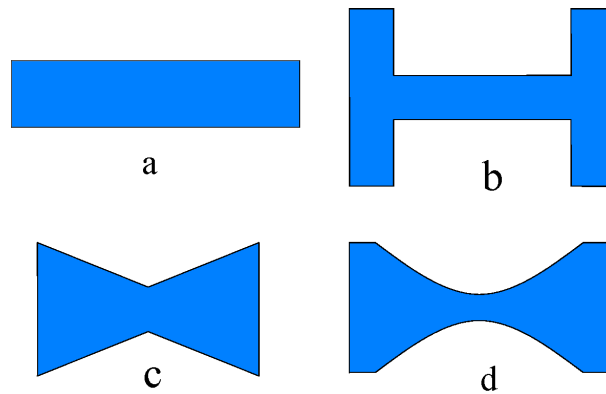


Figure 5.9: Various aperture shapes of the ACMPA: a) rectangular, b) H-shaped, c) bowtie and d) hourglass.

the patch integrated with the aperture is complex and open microstrip line stub is used to compensate the input reactance. With an open-ended stub, the impedance at distance  $l_s$  from the end is

$$Z_s = -jZ_c \tan(\beta l_s), \quad (5.3)$$

where  $l_s$  is the stub length and  $\beta = 2\pi/\lambda$  is the propagation constant. With an appropriate stub length the input reactance of the antenna can be eliminated at a desired frequency. The effect of the varying aperture length on the antenna input impedance is shown in Fig.(5.10). It is seen in Fig.(5.10) that changing the aperture length the input resistance increases as the radiation resistance of the aperture increases. At resonance, the input reactance remains almost constant but resonance frequency shifts a bit. The effect of the stub length on the input impedance is shown in Fig.(5.11). The stub length does not have an influence on the input resistance but on the input reactance as predicted by equation (5.3). The input impedance of the antenna can be optimised by tuning the aperture shape and size and length of

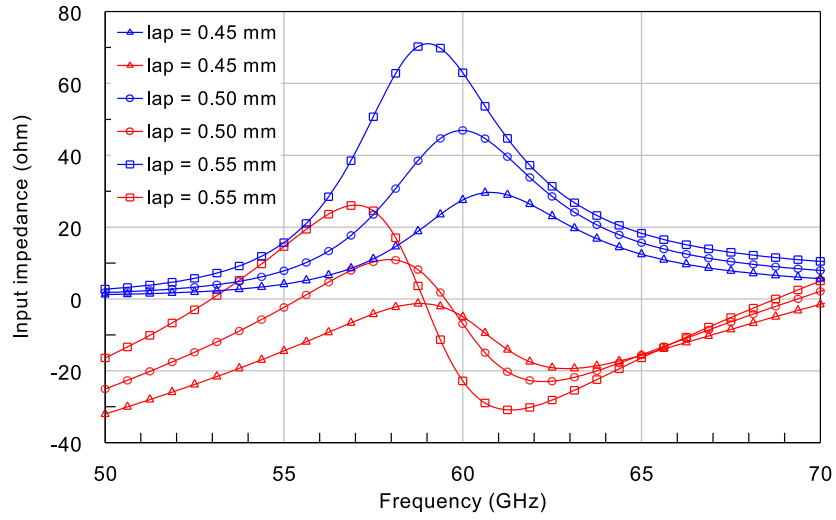


Figure 5.10: ACMPA normalised input impedance as a function of frequency and aperture length ( $\epsilon_r = 5.99$ ,  $h_p = 0.3$  mm, patch size:  $l_p = 0.75$  mm,  $w_p = 0.75$  mm). Simulated with IE3D (MoM).

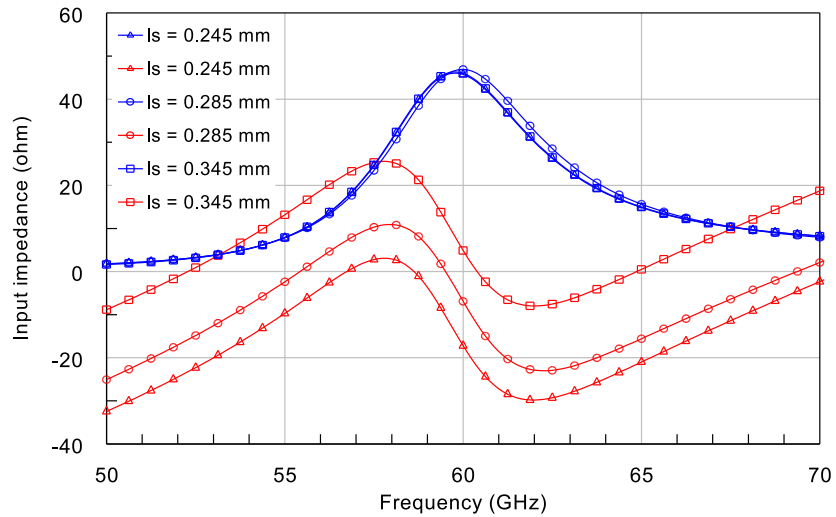


Figure 5.11: ACMPA normalised input impedance as a function of frequency and the stub length ( $\epsilon_r = 5.99$ ,  $h_p = 0.3$  mm, patch size:  $l_p = 0.75$  mm,  $w_p = 0.75$  mm). Simulated with IE3D (MoM).



the matching stub.

Due to shrinkages of the structures during the LTCC process, final dimensions of the antennas are difficult to predict. Since relatively small changes in the aperture length have a strong influence on the input impedance (Fig.(5.10)), ACMPA structures with different aperture lengths were manufactured. Other parameters were kept constant. Design parameters for the ACMPA are summarised in Table (5.1).

Table 5.1: ACMPA design parameters.

	$w_{ms}$	$l_{ap}$	$w_{ap}$	$l_s$	$l_p$	$w_p$	$w_g$	$h_{ms}$	$h_p$
	( $\mu\text{m}$ )	( $\mu\text{m}$ )	( $\mu\text{m}$ )	( $\mu\text{m}$ )	( $\mu\text{m}$ )	( $\mu\text{m}$ )	( $\mu\text{m}$ )	( $\mu\text{m}$ )	( $\mu\text{m}$ )
ACMPA1	150	560	80	315	750	790	2385	100	300
ACMPA2	150	504	80	315	750	790	2385	100	300
ACMPA3	150	616	80	315	750	790	2385	100	300

### 5.3 Slot-coupled microstrip patch antenna

The SCMPA is formed from two metallization layers which are separated by one substrate layer in between. The CPW and the patch use the same substrate (see Fig.(5.12)). The structure is very simple and provides easy integration with integrated circuits. The substrate thickness of  $h_p = 300\mu\text{m}$  was used also for the SCMPA structures. The silver metallization thickness was  $t = 10\mu\text{m}$ .

The slot-coupled microstrip patch antenna uses coplanar waveguide (CPW) as feed and the antenna element is excited by the coupling slot below the antenna element. The CPW is formed by a conducting strip and two side strips separated from the middle strip by slots. The geometry of a CPW is illustrated in Fig.(5.13).

In the SCMPA, the feed line and coupling slot are in the same layer but the patch element may be misaligned relative to the slot and CPW. The effect of the patch element misalignment on the SCMPA input impedance was tested and results are shown in Fig.(5.14). Patch element was shifted by  $60\mu\text{m}$  in  $x$ - and  $y$ -directions. The shift in the  $x$ -direction does not have influence on the input impedance but the shift in the  $y$ -direction changes both, the input resistance and the input reactance. This is probably caused by the increased electric-field coupling from the slot to the patch element (electric field in  $z$ -direction is zero only at the center of the patch). However, it looks like that the expected misalignment of the different layers in LTCC

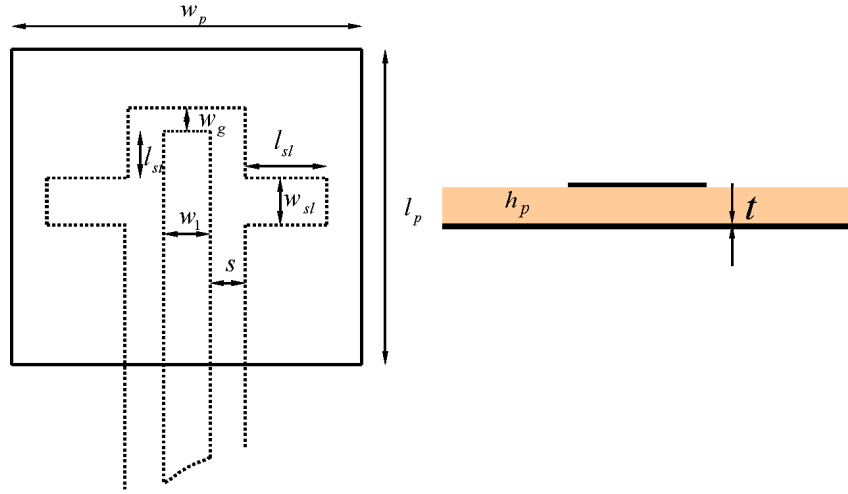


Figure 5.12: Geometry of SCMPA:  $w_1$ =width of the CPW center line,  $s$ =slot width,  $l_{st}$ =stub length,  $w_p$ =width of the patch,  $l_p$ =length of the patch,  $l_{sl}$ =length of the slot,  $l_{st}$ =length of the stub,  $w_{st}$ =width of the slot,  $h_p$ =substrate thickness and  $t$ =metallization thickness.

process (in order of  $\sim 20\mu\text{m}$ ) should not cause problems.

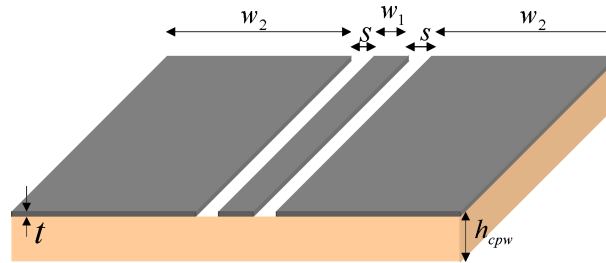


Figure 5.13: Coplanar waveguide:  $w_1$  is the width of the middle strip,  $s$  the width of the slots,  $w_2$  the width of the side strips,  $h_{cpw}$  the substrate height and  $t$  the metallization thickness.

### 5.3.1 Coplanar waveguide parameters

The CPW has design parameters  $w_1$ ,  $w_2$ ,  $s$  and  $h_{cpw}$  to be optimised. In this work, the characteristic impedance of  $50\Omega$  was desired for the CPW. The propagation mode of the CPW is *quasi-TEM* (QTEM), which means that the field distribution is not completely transversal to the propagation direction but fields have also small longitudinal components. The QTEM mode has zero cut-off frequency. Character-

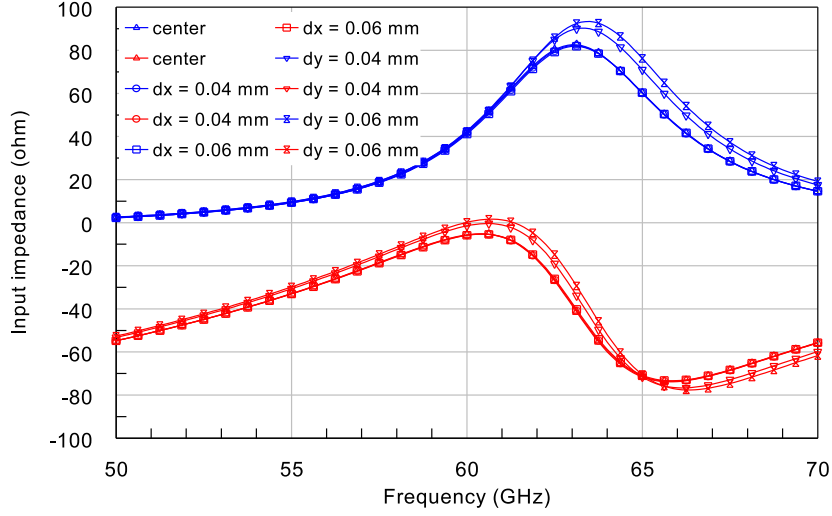


Figure 5.14: SCMPA input resistance (blue) and reactance (red) ( $\epsilon_r = 5.99$ ,  $h_p = 0.3$ , patch size:  $l_p = 0.75$  mm,  $w_p = 0.75$  mm): patch element position shifted in  $x$ - and  $y$ -directions from the center. Simulated with IE3D (MoM).

istic impedance of the CPW can be calculated as

$$Z_c = \frac{1}{c_0 C_0 \sqrt{\epsilon_{cpw,eff}}} + \epsilon_{cpw,eff}, \quad (5.4)$$

where the effective dielectric constant is taken simply as  $\epsilon_{cpw,eff} = (1 + \epsilon_r)/2$ . When calculating  $Z_c$ , the capacitance per unit length,  $C_0$ , has to be solved first. The CPW with three metal strips supports *symmetrical* and *antisymmetrical* QTEM modes. In addition, the *asymmetrical* mode is achieved as a combination of the symmetrical and antisymmetrical modes. Different values for  $C_0$  and  $Z_c$  can be determined in each case.

When outermost strips are in the same potential we get the symmetrical capacitance (see Fig.(5.15 a)) (Lindell, 1997)

$$C_0 = 4\epsilon_0 \frac{K'(k)}{K(k)}, \quad (5.5)$$

where  $K(k)$  is the complete elliptic integral of the first kind,  $K'(k) = K(k')$ ,  $k' = \sqrt{1 - k^2}$  and

$$k = \left( \frac{2 + \frac{w_1 + 2w_2}{s}}{2 + \frac{w_1}{s}} \right) \sqrt{\frac{1 + \frac{w_1}{s}}{(1 + \frac{w_1}{s})(1 + \frac{w_1 + w_2}{s})}}. \quad (5.6)$$

When the middle strip is grounded and outermost strips have opposite potentials (see Fig.(5.15 c)), we obtain the antisymmetrical capacitance as

$$C_0 = \epsilon_0 \frac{K'(k_c)}{K(k_c)}, \quad (5.7)$$

$$k_c = \sqrt{\frac{1 + \frac{w_1}{s}}{(1 + \frac{w_2}{s})(1 + \frac{w_1+w_2}{s})}}. \quad (5.8)$$

When the middle and outermost strips has the same potential we get the asymmetrical capacitance (see Fig.(5.15 b))

$$C_0 = \epsilon_0 \left( \frac{K'(k_a)}{K(k_a)} + \frac{K'(k_b)}{K(k_b)} \right), \quad (5.9)$$

where

$$k_a = \sqrt{\frac{1 + \frac{w_1}{s}}{(1 + \frac{w_2}{s})(1 + \frac{w_1+w_2}{s})}}, \quad (5.10)$$

$$k_b = \left( \frac{2 + \frac{w_1+2w_2}{s}}{2 + \frac{w_1}{s}} \right) k_a. \quad (5.11)$$

It is seen from the previous equations that the asymmetrical capacitance can be formed as a combination of the symmetrical and antisymmetrical capacitances.

In previous equations, the metallization thickness is not taken into account, and the substrate thickness is thought as infinite,  $h_{cpw} \rightarrow \infty$ . In practice, the signal is usually connected to the middle strip and outermost strips are grounded, so the other modes than symmetrical one are not supported. Thus, equations (5.4)-(5.6) can be used to estimate the characteristic impedance of the CPW. In reality, the substrate has finite thickness. The substrate of finite thickness together with the finite ground planes support slab modes in the CPW. However, the dispersion caused

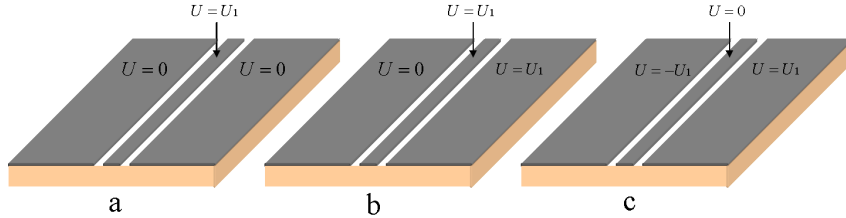


Figure 5.15: a) Symmetrical, b) asymmetrical and c) antisymmetrical QTEM modes of the CPW. The asymmetrical mode is a combination of the symmetrical and antisymmetrical modes.

by slab modes can be avoided if the criterion  $h < 0.1\lambda_d$ , where dielectric wavelength

$\lambda_d = c_0/(f\sqrt{\epsilon_r})$ , is met (Riaziat *et al.*, 1990). At 60 GHz it means using substrate thickness below  $200\mu m$ .

Conductor loss factor of CPW is [dB/m] (Lehto & Räsänen, 2002b)

$$\alpha_{ccpw} = \frac{R_s}{1.6Z_c d K^2(k)[1 - (w_1/d)^2]} \cdot \left\{ \frac{2d}{w_1} \left[ \pi + \ln \left( \frac{4\pi w_1(1 - w_1/d)}{t(1 + w_1/d)} \right) \right] + 2 \left[ \pi + \ln \left( \frac{4\pi d(1 - w_1/d)}{t(1 + w_1/d)} \right) \right] \right\} \quad (5.12)$$

where  $d = w_1 + 2s$ . The surface resistance,  $R_s = \sqrt{(\pi f \mu / \sigma)}$ , so the conductor loss increases as  $\sqrt{f}$  as a function of frequency. The characteristic impedance of the CPW is presented in Fig.(5.16) and the conductor loss in Fig.(5.17). The dielectric loss factor can be calculated using equation (5.2). For the characteristic impedance of  $50\Omega$  the ratio  $s/w_1 \approx 0.21$  for  $\epsilon_r = 5.99$ . It is seen that the conductor loss increases if the center-strip width  $w_1$  or the ratio  $s/w_1$  is decreased. However, it is desirable to keep  $d$  as small as possible compared to the dielectric wavelength to minimise dispersion and radiation losses (Riaziat *et al.*, 1990). In this work, limitations for the CPW parameters came from the manufacturing tolerances which require conductor widths and spacing to be at least  $50\mu m$ . Another restrictive factor was dimensions of the GSG-probes used in the S-parameter measurements which have  $150\mu m$  spacing between the the signal and ground probes. The center strip of width  $w_1 = 200\mu m$  and spacing  $s = 50\mu m$  was used for SCMPAs. These values imply conductor losses 1.1 dB/cm and the dielectric loss of 0.02 dB/cm at 60 GHz.

### 5.3.2 Location, size and shape of the slot

When symmetrical QTEM mode of the CPW is considered, there is a potential difference between the center and ground strips. Thus, the electric field has strong components  $E_x$  and  $-E_x$ , propagating towards  $y$ -direction. Because fields curve symmetrically relative to the CPW center strip, the dominant component of the electric field is of form  $E \sim E_z e^{-jky}$  at the center ( $x = 0$ ) of the strip (see Fig.(5.18)). Using equation (2.3) it is seen that the magnetic field is of form  $H \sim H_x e^{-jky}$  at  $x = 0$ . The electric field,  $E_z$ , is zero under the patch at  $y = 0$  while the magnetic field,  $H_x$ , has its maximum. So, the coupling through the slot to the patch occurs mainly through magnetic field also in the SCMPA. The coupling slot is centered below the patch element in both,  $x$ - and  $y$ -directions.

As was the case with the ACMPA, the magnitude of slot-coupling depends on the

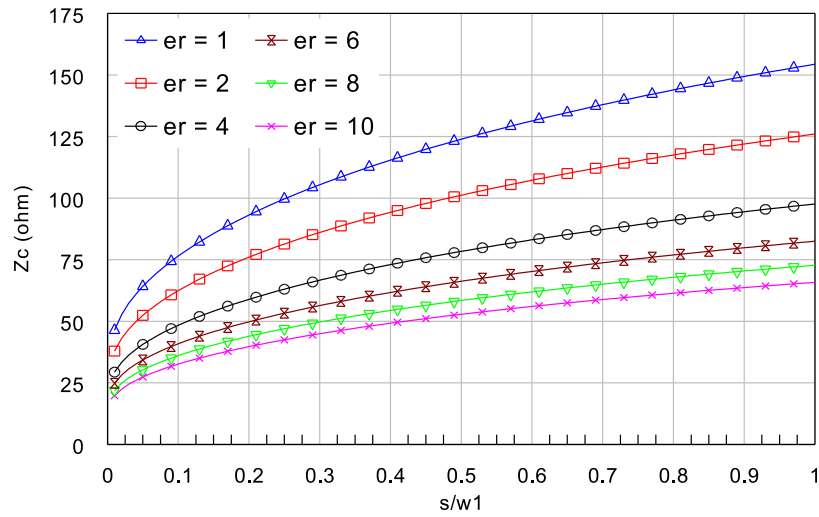


Figure 5.16: Theoretical characteristic impedance of the CPW.

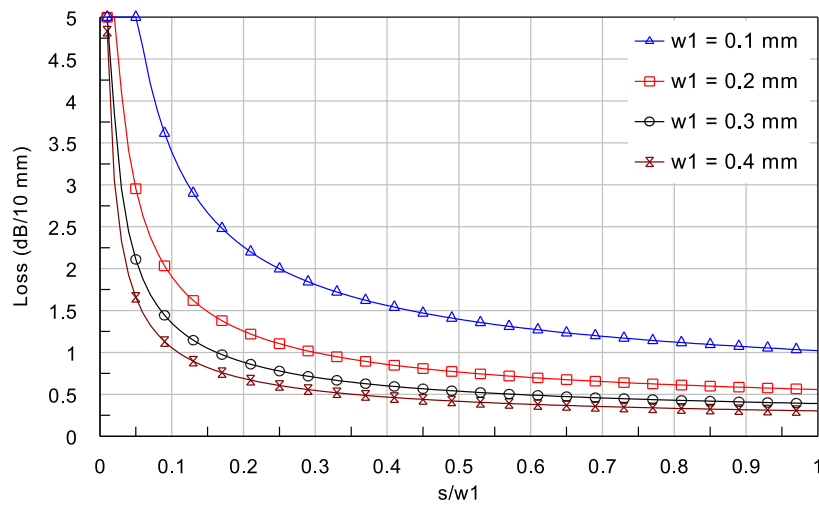


Figure 5.17: CPW conductor loss.

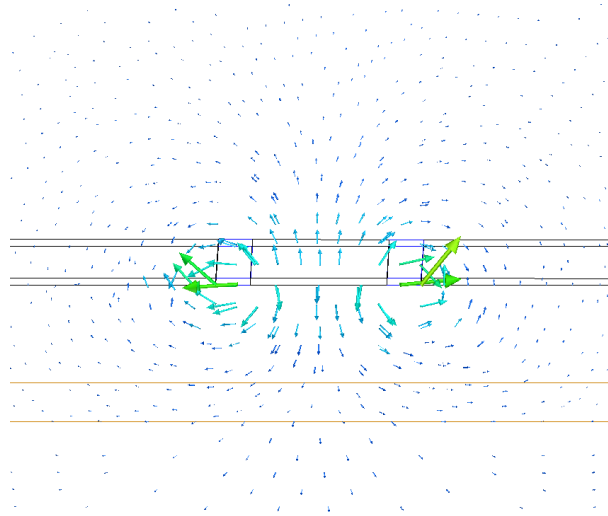


Figure 5.18: Transversal electric field of the symmetrical QTEM mode in the CPW. Simulated with HFSS (FEM).

size of the slot. The radiating resistance increases when the slot length is increased. A rectangular slot was used with SCMPA which provided adequate coupling with reasonable slot size. Simple rectangular slot was chosen mainly because of more complex feed-line structure compared to the ACMPA. The SCMPA input resistance can be tuned by varying the slot size and the input reactance can be eliminated with a matching stub. SCMPA was simulated with varying parameters and effects of the slot and stub lengths on the SCMPA input impedance are presented in Fig.(5.19) and Fig.(5.20), respectively. It is seen in Fig.(5.19) that at resonance, the input resistance increases from  $68\Omega$  to  $98\Omega$  but the input reactance level is constant as the slot length is increased from 0.165 mm to 0.265 mm. The resonance frequency shifts downwards by 1 GHz. Thus, the slot and patch lengths both have an effect on the resonance frequency. The CPW stub length has an effect on both the input resistance and the reactance but resonance frequency keeps unchanged (Fig.(5.20)). The resistance level decreases from  $80\Omega$  to  $45\Omega$  and reactance increases from  $-40\Omega$  to  $-20\Omega$  at resonance as the stub length is increased from 0.08 mm to 0.18 mm. The variation of the resistance may be due to a short stub length: the stub itself is a part of the slot geometry and increasing the stub length leads to a increased radiating resistance of the slot. Stub length 0.08 mm was used in manufacturing. The SCMPAs with three different slot lengths was fabricated. Design parameters of the SCMPAs are shown in Table (5.2).

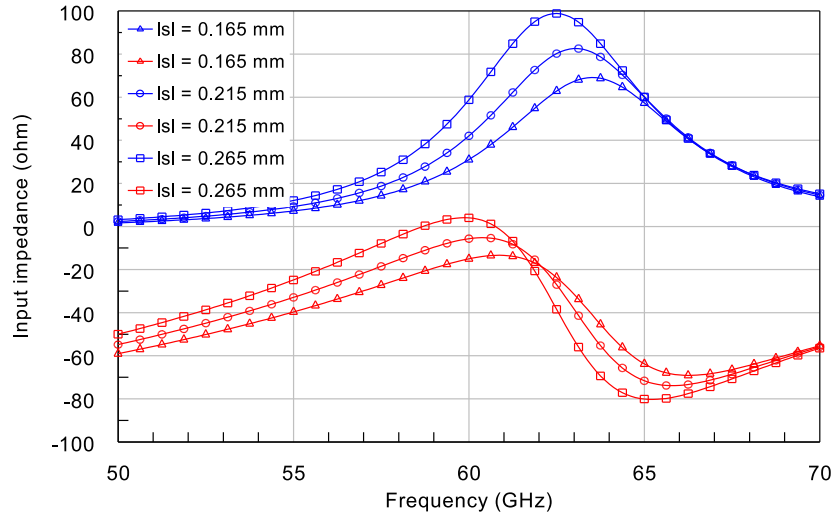


Figure 5.19: SCMPA input resistance (blue) and reactance (red) as a function of frequency and the slot length ( $\epsilon_r = 5.99$ ,  $h_p = 0.3$  mm, patch size:  $l_p = 0.75$  mm,  $w_p = 0.75$  mm). Simulated with IE3D (MoM).

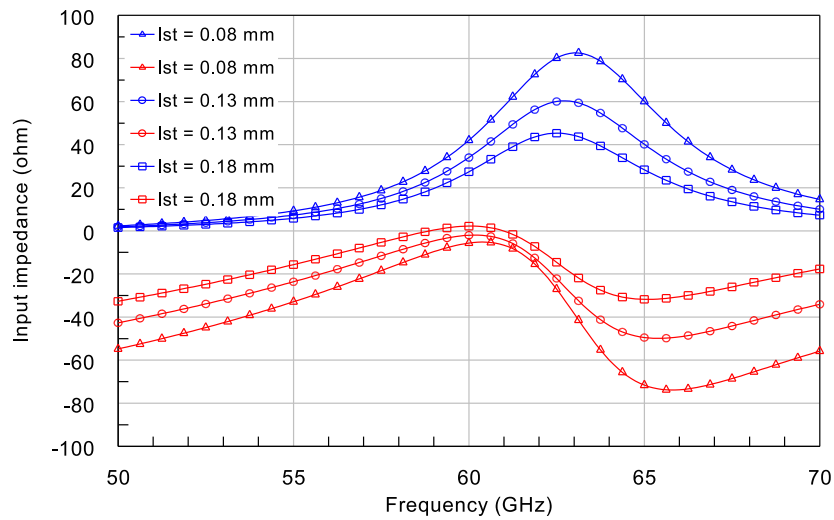


Figure 5.20: SCMPA input resistance (blue) and reactance (red) as a function of frequency and the stub length ( $\epsilon_r = 5.99$ ,  $h_p = 0.3$ , patch size:  $l_p = 0.75$  mm,  $w_p = 0.75$  mm). Simulated with IE3D (MoM).



Table 5.2: SCMPA design parameters.

	$w_1$	$w_2$	$s$	$l_{sl}$	$w_{sl}$	$l_{st}$	$l_p$	$w_p$	$h_p$
	( $\mu\text{m}$ )	( $\mu\text{m}$ )	( $\mu\text{m}$ )	( $\mu\text{m}$ )	( $\mu\text{m}$ )	( $\mu\text{m}$ )	( $\mu\text{m}$ )	( $\mu\text{m}$ )	( $\mu\text{m}$ )
SCMPA1	200	1350	50	215	130	80	740	790	300
SCMPA2	200	1350	50	194	130	80	740	790	300
SCMPA3	200	1350	50	237	130	80	740	790	300

## 5.4 Proximity-coupled microstrip patch antenna

Basic proximity-coupled feed shown in Fig.(3.3 c) uses two substrate layers with a microstrip line on a lower substrate. This structure is simple but suffers from quite poor bandwidth although thicker substrate can be used for the patch. Bandwidth can be improved by using an aperture on a ground plane (Gao & Sambell, 2005). Now, the structure is similar to the ACMPA but the ground plane and the microstrip line have changed positions (Fig.(3.3 d)). In this work, it was beneficial to use PCMPA because of its suitable geometry for the measuring equipment (see Section 5.5). Since the basic structure of the PCMPA is quite similar to the ACMPA the same parameters are varied for the input impedance and resonance frequency tuning: patch size, aperture size, microstrip line width and stub length. It was mentioned earlier that the aperture width does not have much influence on the input impedance. In Fig.(5.21) the input impedance for different values of aperture widths is presented. It is seen that for wide aperture the input impedance does not change much if the aperture width is altered. At resonance frequency ( $\sim 57$  GHz) the input reactance keeps constant for all values of  $w_{ap}$  but the input resistance increases as the aperture width is decreased. For very small values of  $w_{ap}$  the resistance starts to increase rapidly. Manufacturing tolerances of the LTCC process require the aperture and metal strip widths to be at least  $50\mu\text{m}$  and  $w_{ap} = 0.1$  mm was used for PCMPA. It can be assumed that in this work, the variations in the aperture width values do not have much effect on the input impedance. The substrate thickness of  $200\mu\text{m}$  was used for the microstrip line. Overall substrate thickness was  $400\mu\text{m}$ . In the PCMPA the microstrip is embedded inside the substrate. There was no design formula for the characteristic impedance for such a structure available and the width of the microstrip line was determined with the HFSS (FEM) simulator. The width  $0.18$  mm was used to obtain a characteristic impedance of  $50\Omega$ . Other parameters

for PCMPA were: stub length 0.265 mm, patch length 0.84 mm and patch width 0.76 mm. PCMPAs with two different values of aperture length was fabricated. Summary of the PCMPA design parameters are given in Table (5.3).

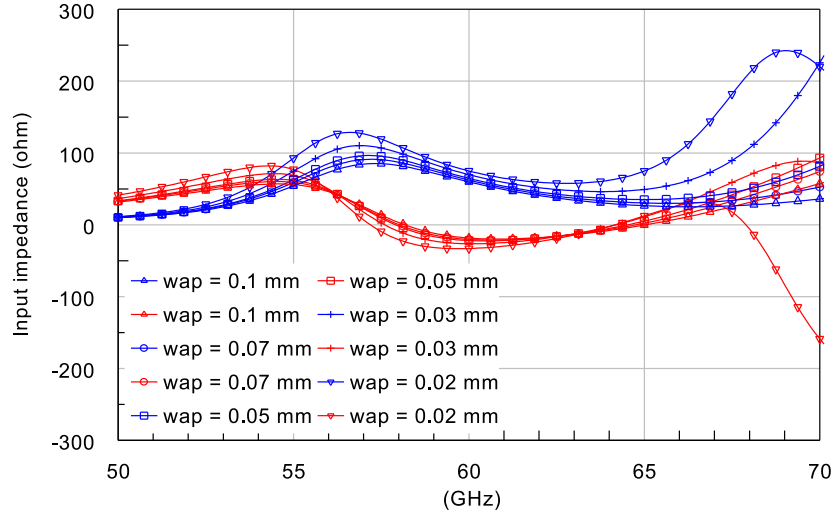


Figure 5.21: PCMPA input resistance (blue) and reactance (red) as a function of frequency and aperture width ( $\epsilon_r = 5.99$ ,  $h_p = 0.4$  mm, patch size:  $l_p = 0.88$  mm,  $w_p = 0.76$  mm). Simulated with IE3D (MoM).

Table 5.3: PCMPA design parameters.

	$w_{ms}$	$l_{ap}$	$w_{ap}$	$l_s$	$l_p$	$w_p$	$w_g$	$h_{ms}$	$h_p$
	( $\mu\text{m}$ )	( $\mu\text{m}$ )	( $\mu\text{m}$ )	( $\mu\text{m}$ )	( $\mu\text{m}$ )	( $\mu\text{m}$ )	( $\mu\text{m}$ )	( $\mu\text{m}$ )	( $\mu\text{m}$ )
PCMPA1	180	860	100	265	840	760	3000	200	200
PCMPA2	180	940	100	265	840	760	3000	200	200

## 5.5 Antenna modifications

### 5.5.1 Antennas connected to the test fixture

In order to measure radiation patterns the antennas had to be connected to a test fixture. Anritsu Wiltron 3680V universal test fixture (Fig. (5.22)) provides either CPW or MS connection and reliable measurements up to 65 GHz and it was used

in this work. Frequency limitation is due to coaxial *V-connector* with 1.85 mm diameter. The antenna is connected between the fixture jaws which are pulled to-

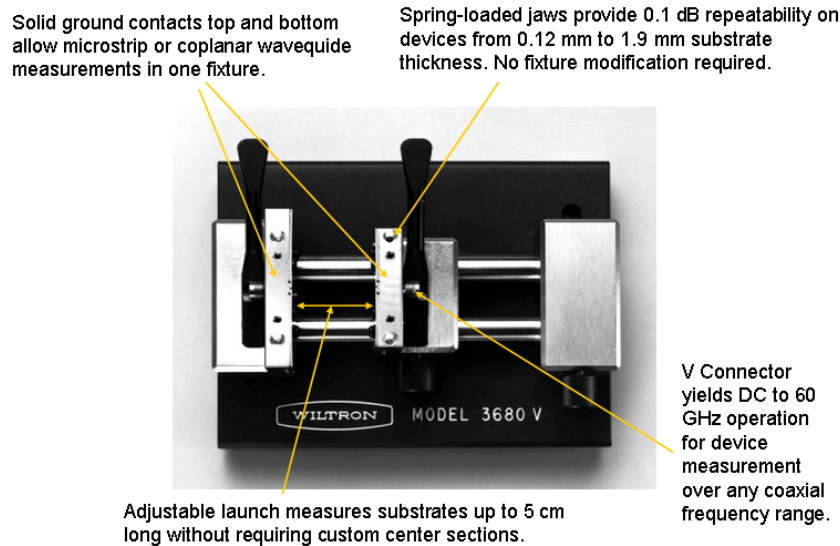


Figure 5.22: Test fixture used in radiation pattern measurements. Redrawn from (Anritsu Wiltron, 2005)

gether by springs. Between the jaws there is a connector that has a small pin where the high-frequency signal is fed through a coaxial cable. Other metal parts of the jaws act as grounds. Pin is connected into the microstrip line or CPW center strip while the jaws ground the ground planes of the microstrip line or CPW. To keep the influence of the metal parts of the fixture on the measurements small enough, the antenna feed lines were designed to be in order of  $\sim 1.5 - 2$  cm. The patch element and the feed line connection should be on the same side to direct the major lobe of the radiation pattern upwards from the test fixture. Feeding of the ACMPA is not possible in this way but SCMPA and PCMPA can be fed with a CPW and a microstrip line, respectively. However, some modifications on these structures had to be made.

The CPW is used to feed the SCMPA. Orientation of the CPW should be such that the ground planes and center strip should be on the upper and the substrate on the lower side. This is contrary to the basic SCMPA structure which has the metallization on the lower and the substrate on the upper sides. Some modifications were done for the SCMPA structure.

The test fixture contains lots of metal parts and prevents radiation below the fixture. The SCMPA was modified so that an additional substrate (thickness  $h_{cpw} = 500\mu\text{m}$ )

and a ground plane were placed below the the CPW. The CPW is transformed into a GCPW (grounded CPW) and the structure is abbreviated as SCGMPA. In order to connect the structure to the test fixture the feed line consists of an air-filled GCPW which transforms into a dielectric-filled GCPW embedded inside the substrate (Fig(5.23)). The characteristic impedance was kept as  $50\Omega$  and GCPW parameters had to be determined with simulations. The GCPW supports parallel plate modes. With finite substrate widths the structure is a dielectric waveguide that has cutoff frequencies relative to the substrate width. Two via fences with  $180\mu\text{m}$  via diameters and  $450\mu\text{m}$  mutual distances were placed along the CPW between two conducting plates to avoid additional modes. Via fences with conducting plates form a rectangular waveguide. Via fences were placed  $900\mu\text{m}$  apart from each other to set the cutoff frequency of the lowest rectangular waveguide mode,  $\text{TE}_{10}$ , apart from the operating frequency, approximately to 68 GHz. Because of small enough distances between vias ( $\sim 0.13\lambda_d$ ), via fences were replaced with solid conducting walls in simulations to reduce complexity. The CPW had parameters  $w_1 = 0.2$  mm and  $s = 0.1$  mm. Three different variants of the SCGMPA were manufactured with  $l_{sl} = 0.200$  mm,  $l_{sl} = 0.180$  mm and  $l_{sl} = 0.220$  mm. Other parameters were:  $w_1 = 0.2$  mm and  $s = 0.160$  mm,  $l_{sl} = 0.200$  mm,  $w_{sl} = 0.160$  mm,  $l_{st} = 0.070$  mm,  $l_p = 0.750$  mm and  $w_p = 0.750$  mm.

It was noticed that the metallization of the test fixture causes a lot of distortion to the radiation pattern results. Also, due to lack of calibration standards the  $S_{11}$ -parameter results for the SCGMPA were poor (see Section 6.2).

At next stage, the test fixture was taken to pieces because only one jaw is needed to conduct the measurements. The back radiation of the antennas is not critical anymore and the design was desired to be kept as simple as possible. Also, there was a need for manufacturing calibration standards for better S-parameter measurement results. SCMPA was modified in such a way that another substrate of thickness  $200\mu\text{m}$  was added below the CPW in SCMPA but no additional conducting plates or vias were used. The CPW transforms from CPW into dielectric-filled, embedded CPW. Again, the CPW parameters had to be determined with HFSS (FEM) simulations in order to keep the impedance level at  $50\Omega$ . The CPW feed with  $200\mu\text{m}$  thick substrate had design parameters  $w_1 = 0.2$  mm and  $s = 0.05$  mm and the length of 25 mm. The conductor loss of the CPW feed can be approximated from Fig.(5.17). It is seen that conductor loss is  $\sim 2.5$  dB/2.5cm at 60 GHz. The CPW embedded inside the substrate had parameters  $w_1 = 0.2$  mm and  $s = 0.1$  mm. Other parameters used in manufacturing: slot lengths 0.165 mm and 0.202 mm, slot width 0.13 mm, stub length 0.09 mm, patch length 0.79 mm and patch width 0.79

mm. The SCMPA integrated with the feed line is abbreviated as SCEMPA, where "E" refers to an embedded CPW in the SCMPA. Design parameters for SCGMPA and SCEMPA are summarised in Table (5.4). The HFSS simulation model of the SCGMPA and SCEMPA structures are shown in Fig(5.23). Only half of the structures is shown because symmetry plane was used in simulations (see Section 6.1).

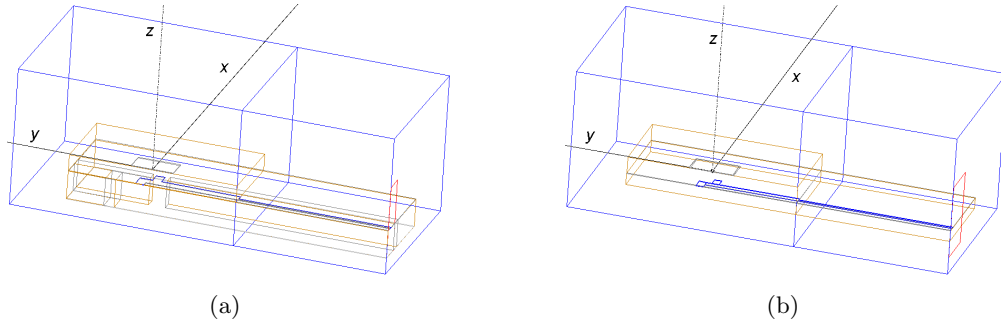


Figure 5.23: HFSS simulations models of the a) SCGMPA and b) SCEMPA.

Table 5.4: Design parameters of the SCGMPA and SCEMPA.

	$w_1$	$w_2$	$s$	$l_{sl}$	$w_{sl}$	$l_{st}$	$l_p$	$w_p$	$h_{cpw}$	$h_p$
	( $\mu\text{m}$ )	( $\mu\text{m}$ )	( $\mu\text{m}$ )	( $\mu\text{m}$ )	( $\mu\text{m}$ )	( $\mu\text{m}$ )	( $\mu\text{m}$ )	( $\mu\text{m}$ )	( $\mu\text{m}$ )	( $\mu\text{m}$ )
SCGMPA1	200	2000	160	200	160	70	750	750	500	300
SCGMPA2	200	2000	160	180	160	70	750	750	500	300
SCGMPA3	200	2000	160	220	160	70	750	750	500	300
SCEMPA1	200	1300	100	165	130	90	790	790	200	300
SCEMPA2	200	1300	100	202	130	90	790	790	200	300

In the PCMPA, the microstrip is embedded inside the substrate and feeding of the antenna is not possible without some modifications.  $50\Omega$  microstrip feed line with substrate thickness of  $200\mu\text{m}$ , strip width  $w = 0.26$  mm and length 25 mm was designed to feed the PCMPA. Thus, the feeding of the PCMPA is constructed from a microstrip line which transforms into an embedded microstrip line. The conductor loss of two-layered microstrip line is in order of  $\sim 1.4$  dB/2.5cm, a half compared to one-layered line (Fig.(5.6)). From now on the abbreviation PCMPA is used to refer to the antenna structure integrated with the microstrip line feed (see Fig(5.24)).

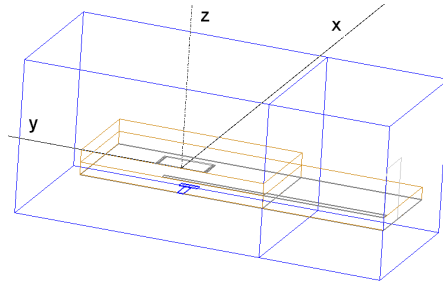


Figure 5.24: HFSS simulation model for PCMPA.

### 5.5.2 Calibration standards

When making scattering-parameter measurements there is a need to separate the effects of the transmission medium from the device characteristics and calibration of the measurement environment is required. SCEMPA and PCMPA antenna structures were designed to be tested with the test fixture (Fig.(5.22)). In addition to the distortions caused by the vector network analyzer, coaxial cables and so on, the effects of the coaxial-to-microstrip and coaxial-to-CPW transitions on the measurements are desired to be minimised. The calibration standards using CPW and microstrip lines were designed for this purpose.

The so-called TRL calibration method was used which relies only on the characteristic impedance of a short transmission line (Agilent Technologies, 2001). TRL refers to the three steps in the calibration: *thru* - connection of port 1 and port 2, directly or with a short length of transmission line, *reflect* - connect identical one-port high reflection coefficient devices to each port and *line* - insert a short length of transmission line between port 1 and 2 (different line lengths are required for the *thru* and *line*). TRL calibration standards for the microstrip connection are presented in Fig(5.25). The calibration plane will be established as the plane where the vertical dashed line is located, i.e. at the end of the *reflect*. The *reflect* can be an open or short circuit and both were manufactured in this work. The length of the *reflect*,  $l_{ref}$  is half of the length of the *thru*,  $l_{thru}$ . The length of the *line*,  $l_{line}$ , should be approximately  $\lambda/4$  longer than  $l_{thru}$ . The wavelength of the transmission line is obtained from speed of light, frequency and effective permittivity of a line as  $\lambda = c_0/(f\sqrt{\epsilon_{reff}})$ . Calibration lines were designed to be similar to those used as feed lines for SCEMPA and PCMPA. Two TRL calibration sets with different line lengths were manufactured. The parameters of the TRL calibration standards are presented in Table (5.5). Subscripts 1 and 2 are used to refer sets 1 and 2, respectively.

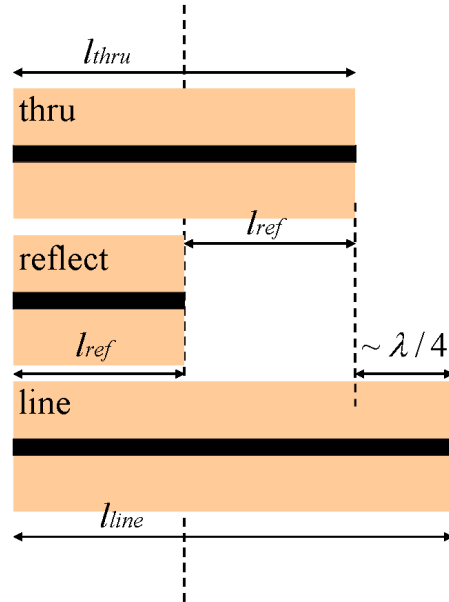


Figure 5.25: TRL calibration.

Table 5.5: Line lengths of TRL calibration standards

Parameter	MS (mm)	CPW (mm)
$l_{thru,1}$	20	20
$l_{ref,1}$	10	10
$l_{line,1}$	20.59	20.72
$l_{thru,2}$	25	25
$l_{ref,2}$	12.5	12.5
$l_{line,2}$	25.59	25.72

## Chapter 6

# Simulations and measurements

Simulation software are based on numerical technique such as MoM, FEM or FDTD. Each technique has its own benefits and disadvantages but none of them gives "exact" results. Validation of the design is needed and it is usually done by conducting test measurements for the prototype structures. In order to determine the input impedance, bandwidth, gain, polarisation or other parameters of an antenna, usually the S-parameter and radiation pattern measurements are conducted.

In this Chapter, simulations and measurements of the designed structures are presented. Section 6.1 concentrates on the issues related to the simulation software. Also, the MATLAB simulation code implemented by the author is described. In Section 6.2 measurement equipment and procedures are presented. Measurements include checking dimensions using microscope, S-parameter and radiation pattern measurements. Finally, the simulation and measurement results are analysed in Section 6.3.

### 6.1 Simulations

The numerical simulation is an important stage in the modern RF design. Although the simulation itself is performed by a personal computer, the preparation of the simulation setup requires understanding of the physical properties of the structure to be simulated. Also, the designer has to be aware of software-related issues in order to obtain proper results.

#### 6.1.1 IE3D (MoM)

Simulations were first conducted using the Zeland IE3D 11.11 commercial MoM software. It was mentioned earlier that when substrates and ground planes with infinite



widths are used, IE3D is very fast for solving S-parameters and radiation patterns for the microstrip antennas. Thus, IE3D is useful especially at the early stage in the design when appropriate design parameters are sought. Parameter studies in Chapter 5 were conducted using infinite ground plane and substrate widths. Later, finite ground planes were used but substrate widths were kept as infinite. Also, the metallizations were modeled having zero thicknesses.

IE3D uses triangular and rectangular mixed non-uniform meshing on polygons that usually represent electric conductor parts of the structure. If a layer is defined as a conductor with infinite width, polygons on that layer represent apertures or slots of, for example, slot antenna. In ACMPA and SCMPA, apertures and slots, instead of large metal plates (ground planes), can be represented with polygons and less unknowns are produced in simulation leading to a reduced simulation time.

Versions 11.0 and later enable the use of *automatic edge cells* (AECs) for the metallic strips. Current concentrates on the edges of metallic plates. The AEC feature improves simulation accuracy by adding small cells along the edges. However, more grid cells means more unknowns and more simulation time and the designer has to decide in each case if the AEC feature is advantageous or not. In this work, the AEC feature was used but it did not have great influence on the results.

### 6.1.2 HFSS (FEM)

After simulated and optimised with the IE3D, the ACMPA and SCMPA structures were modeled with the Ansoft HFSS 8.0.22 commercial software based on FEM. Also, the modified structures, SCGMPA, SCEMPA and PCMPA, were simulated with HFSS since the structures have dielectric layers with finite dimensions and simulations with IE3D would have required more simulation time. Basic characteristics of the FEM are presented in Section 3.5, and now practical issues related to the simulations using the HFSS are concerned.

In the HFSS, the geometry of the structures to be simulated is drawn in a three-dimensional form. Substrate layers, ground planes, feed lines, patch elements etc. can be drawn with realistic dimensions. In order to get proper results the *radiation boundary* must be drawn around the structure. The radiation boundary is an approximation of free space. In this work, the radiation boundary was formed by the faces of the air-filled rectangular box around antenna structures. The size of the box should be big enough to prevent distortions in radiation and impedance characteristics. It is recommended that the distance from the radiating sources to the radiation boundary should be at least  $\lambda/4$  (Ansoft, 2001). This requirement was

fulfilled. Another important issue in drawing is the size of the port, i.e. the area at which the software calculates the field distribution that it uses as feed mode of the structure. For example, the port can be a rectangle transversal to the microstrip feed line. If the port is too small the field distribution of the microstrip line is miscalculated which causes error in the input impedance. For the CPW port, the width should be at least  $3 \cdot (2s + w_1)$  and height at least  $4h_{cpw}$  (Ansoft, 2001). The sizes of the ports used in simulation were defined to be big enough.

The simulation time can be reduced if the structure has symmetry properties. Depending on the orientations of the electric and magnetic field lines, E-plane or H-plane symmetries can be used. If symmetry occurs such that the electric field is normal to the symmetry plane, *perfect E-symmetry plane* is used. If symmetry occurs such that electric field is tangential to the symmetry plane, *perfect H-symmetry plane* is used. In this work, it is assumed that the microstrip line operates at the basic QTEM mode (Fig.(5.8)) and the CPW at the symmetrical QTEM mode (Fig.(5.18)), so H-plane symmetry can be used for the antenna structures at  $x = 0$ . It should be thought twice if the symmetry planes can be used or not. Transmission lines usually have number of modes at which they can operate. When symmetry plane is used, modes that are not symmetrical are eliminated from the simulation due to boundary conditions. For example, for the CPW only the field distribution related to symmetrical QTEM mode is calculated and excited into the structure. The use of symmetry planes reduces simulation time significantly. For example with adequate convergence criterion, simulation of the SCMPA with symmetry plane took  $\sim 10$  minutes, used approximately 9000 tetrahedra and 150 MB of computer memory whereas without symmetry plane simulation took  $\sim 20$  minutes with 13000 tetrahedra and 260 MB of computer memory.

### 6.1.3 MATLAB code (FDTD)

In this Section, the FDTD code written with MATLAB is described in detail. However, the theoretical and mathematical concepts related to FDTD algorithm are not presented here. If interested, the reader is encouraged to see for example (Yee, 1966) or (Taflove & Hagness, 2000) for more information. The code is given as Appendix A.

Simulation consists of one- (1D) and three- (3D) dimensional simulations. In one-dimensional simulation, the voltage source is excited in the middle of the calculation grid and voltage and current values are updated by turns. The Gaussian pulse was used as an excitation. It was tested with DFT that pulse contained enough energy

up to 75 GHz frequencies. The 3D simulation models the ACMPA1 or SCMPA1 structure. The last voltage component of the 1D simulation is used as the source of 3D simulation. The port of the 3D simulation is modeled as a rectangular coaxial waveguide (RCW) in both ACMPA1 and SCMPA1 antennas. In ACMPA1, the inner conductor of the RCW is attached to the microstrip line and the outer conductor is connected to the ground plane. In SCMPA1, the inner conductor is connected to the CPW center strip while the outer conductor is attached to the ground strips of the CPW. Voltage difference is placed at four locations directed from the inner to the outer conductor of the RCW.

Two 1D simulations were run simultaneously. First one simulated the incident field with absorbing boundary conditions (ABC). The second simulation was connected in 3D antenna structures and the reflected voltage signal was stored in memory. The DFT was calculated for both the incident and the reflected signals and the  $S_{11}$ -parameter was achieved as a function of frequency by dividing the reflected signal with the incident one.

A uniform rectangular grid of size  $3\text{ mm} \times 3\text{ mm} \times 1.5\text{ mm}$  in  $x$ -,  $y$ - and  $z$ -directions is used with a cell size  $\Delta x = 25\mu\text{m}$ ,  $\Delta y = 75\mu\text{m}$  and  $\Delta z = 50\mu\text{m}$ , resulting in 144000 cells in the 3D calculation grid. The 1D simulation consisted of 50 cells with cell size  $\Delta y = 75\mu\text{m}$ . The cell dimensions was decided such that the dimensions of the ACMPA1 and SCMPA1 antennas will be as close as possible to the ones simulated with IE3D and HFSS. However, the design parameters had to be adjusted to the uniform grid. Parameters for ACMPA1 and SCMPA1 used in FDTD simulations are presented in Table (6.1).

It is recommended that the minimum wavelength/cell dimension ratio of the structure should be at least 20 (Nikoskinen & Kärkkäinen, 2004). Minimum ratio is  $\lambda_d/\Delta y = 2.04/0.075 \approx 27$ , and the requirement is fulfilled. The time step,  $\Delta t$ , is determined by the stability criterion in three dimensions which leads to a value of  $\Delta t \approx 71.5\text{ fs}$ . The number of time steps was chosen such that  $S_{11}$ -parameters were settled down and no variations occurred anymore. Simulations were conducted with 3000 time steps.

The metallizations were thought as perfect electric conductors (PEC) and electric fields tangential to the conductors were set as zero. With a dielectric object the boundary condition requires the tangential electric field to be continuous at the boundaries. The value of the dielectric constant at air-substrate interface was calculated as an average of the dielectric constants of the air and dielectric material. The Mur 1 absorbing boundary condition was used in the 1D and the 3D simulation space was surrounded by the Liao (N=3) ABC. The FDTD method provides

Table 6.1: Parameters used in FDTD simulations.

	$w_{ms}$	$l_{ap}$	$w_{ap}$	$l_s$	$h_{ms}$	$l_p$	$w_p$	$h_p$
ACMPA1	150	550	75	300	100	750	800	300
	$w_1$	$s$	$w_{sl}$	$l_{sl}$	$l_{st}$	$l_p$	$w_p$	$h_p$
SCMPA1	200	50	150	250	75	750	800	300

time-stepped field illustrations. Field dynamics of  $E_z$  and  $H_x$  field components of ACMPA1 is shown in Fig.(6.1) between time steps 500...550. It is seen from the  $E_z$  plotted on the  $xy$ -plane at the level of the antenna element that the field strength is at maximum at the edges of the patch, especially at the corners. During 50 time steps the phase of the field shifts by  $\sim 180^\circ$  (blue and red colours are interchanged). Magnetic field  $H_x$  is plotted on  $xy$ -plane at the level of the microstrip line. It is seen that the field distribution is symmetrical and signal is transferred along the microstrip line.

## 6.2 Measurements

In this Section, the measurements are presented. First, realised dimensions of manufactured structures were checked. Then, S-parameter measurements were conducted to determine the input matching of the antennas. Finally, the radiation pattern measurements were carried out to test how the antennas radiate in reality.

### 6.2.1 Realised antenna parameters

Shrinking in the LTCC process is about 15% in  $x$ - and  $y$ -directions for the Ferro A6-S substrate (Table (4.2)). Due to uncertainty of the final dimensions of the antenna structures, dimensions of the antennas were checked with a Wild Heerbrugg M3Z microscope.

The accuracy of the measurement was determined by the minimum possible distance which was able to be perceived. All the important parameters were possible to be measured for the SCMPA structures (see Fig.(6.2)). The patch element and the microstrip line dimensions were measured for ACMPAs (see Fig.(6.3)) but aperture sizes remained unknown because of the aperture location inside the substrate. Designed and measured values for SCMPA and ACMPA structures are presented

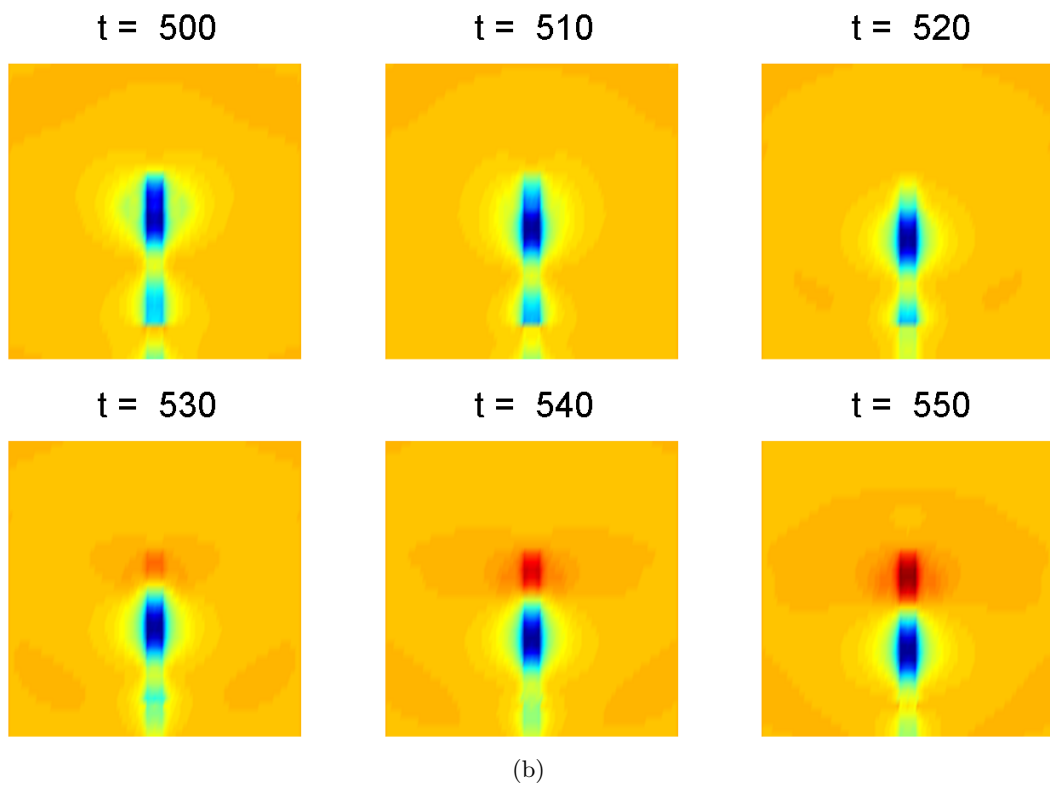
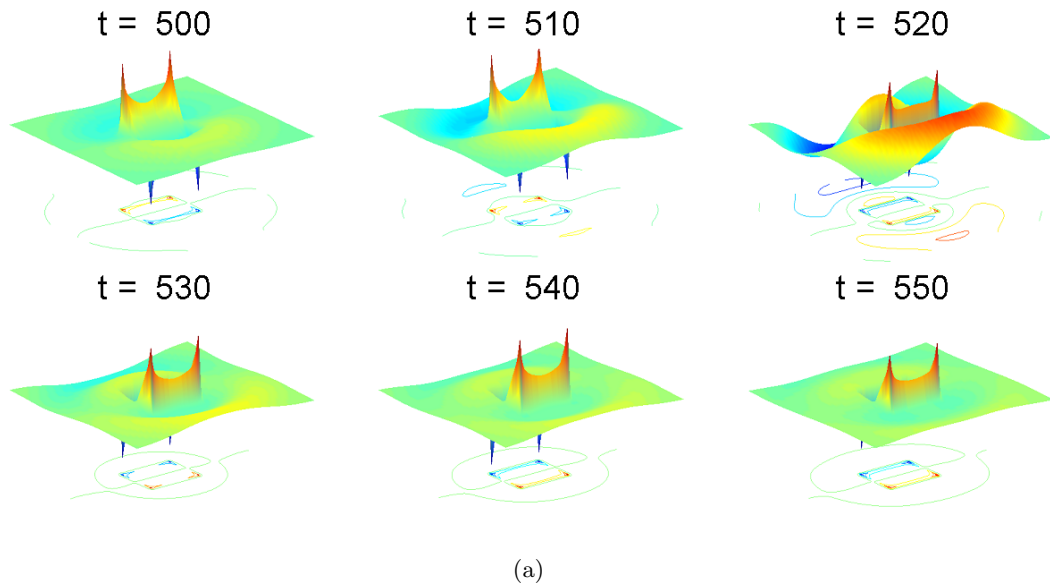


Figure 6.1: Magnitudes of the field components of the ACMPA at different time instances ( $t$ ): a)  $E_z$  at the patch level and b)  $H_x$  at the level of the microstrip line. Simulated with MATLAB (FDTD).

in Tables (6.2) and (6.3). It is seen that the measured CPW spacing ( $s$ ) deviates

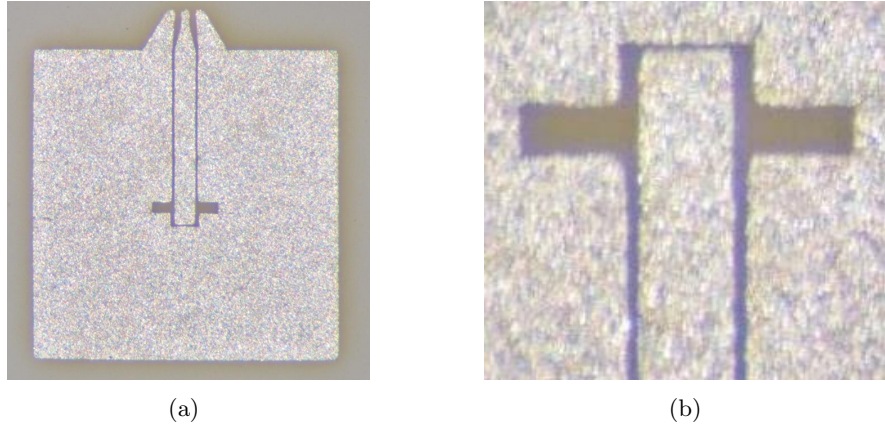


Figure 6.2: Photographs of SCMPA ground plane.

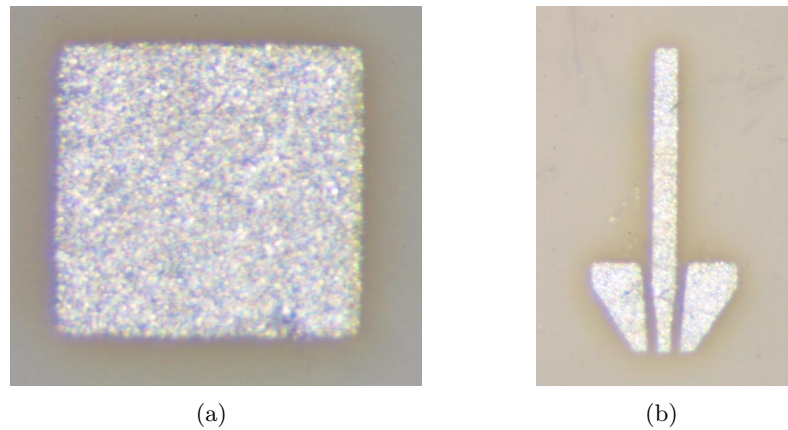


Figure 6.3: Photographs of ACMPA patch element and microstrip line.

strongly from the designed value which has an effect on the CPW characteristic impedance. It can be assumed that deviations in slot length ( $l_{sl}$ ) and patch widths ( $w_p$ ) have an effect on the input impedance values whereas deviations in patch lengths may cause shifting in resonance frequencies.

### 6.2.2 S-parameter measurements

The S-parameter measurements for ACMPA and SCMPA antennas were carried out with an on-wafer probe station at frequency range 50 - 75 GHz. The GSG probes with  $150 \mu\text{m}$  pitch between signal and ground probes enabled direct connection to CPW feeds in SCMPAs (see Fig.(6.4)). In order to use the same probes for mea-

Table 6.2: Realised SCMPA parameters.

	Designed ( $\mu\text{m}$ )	Measured $\pm 9$ ( $\mu\text{m}$ )	Error (%)
$w_1$	200	213	7
$s$	50	19	62
$l_{sl,1}$	215	210	2
$l_{sl,2}$	194	201	4
$l_{sl,3}$	237	245	3
$w_{sl}$	130	105	19
$l_{st}$	80	140	75
$l_p$	740	779	5
$w_p$	790	823	4
$w_{gap}$	80	13	84

Table 6.3: Realised ACPMA parameters.

	Designed ( $\mu\text{m}$ )	Measured $\pm 9$ ( $\mu\text{m}$ )	Error (%)
$w_{ms}$	150	158	5
$l_p$	750	796	6
$w_p$	790	831	6

suring ACPMAs, small metal plates connected with vias into the ground plane were added in manufacturing (Fig.(6.3 b)). Antennas were positioned on top of a 1 cm thick Rohacell foam sheet ( $\epsilon_r < 1.15$ ) with Cuming Microwave C-RAM GDSS absorber slab on the bottom. Since the far-field limit is at distance  $\sim 0.32$  mm at 75 GHz the Rohacell and absorber sheets were adequate to simulate far-field conditions and prevent multiple reflections.

The modified antenna structure, SCGMPA, was measured with the test fixture. Other antennas, SCEMPA and PCMPA will be tested in near future as soon as they are manufactured. SCGMPA and SCEMPA use GCPW and CPW and PCMPA use microstrip feed lines. Extra substrate layer added in manufacturing below the GCPW in SCGMPA assured basic CPW connection in SCGMPA. The measure-

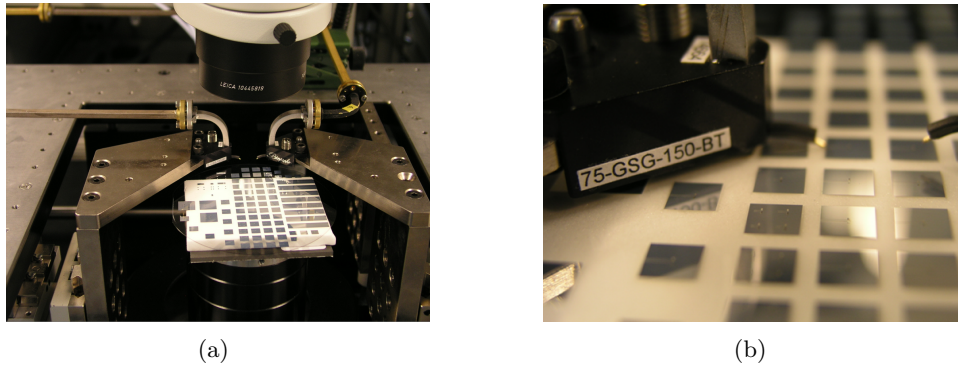


Figure 6.4: S-parameter measurements with the on-wafer probe station: a) measurement arrangement, b) GSG-probes.

ment arrangement is shown in Fig.(6.5). Measurements were conducted with a HP 8510C vector network analyzer. The calibration was carried out with HP 85109B K19 coaxial calibration kit for a coaxial cable with a diameter of 1.85 mm. However, distortions caused by the coaxial-to-cpw transition were included in the  $S_{11}$ -parameter results. The test fixture was covered with a Cuming Microwave C-RAM FLX-10/PSA 0.0062" absorber. Absorber sheets located approximately at distance 2 cm from the antenna element and far-field conditions were fulfilled.

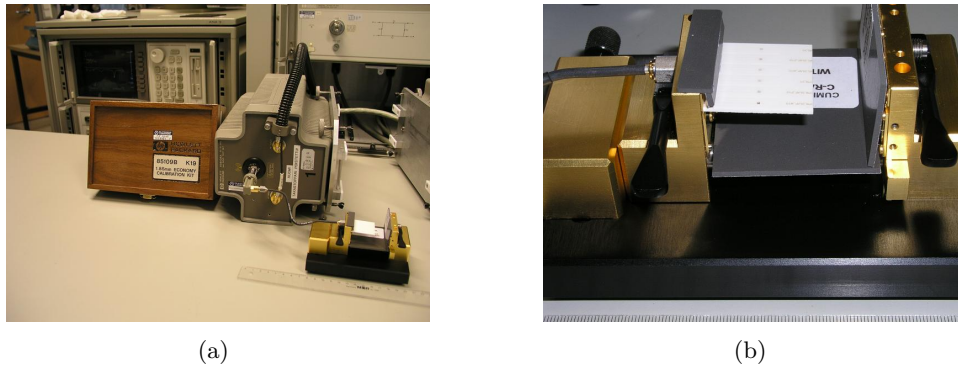


Figure 6.5: S-parameter measurements for SCGMPA: a) measurement arrangement, b) antenna connected to the test fixture.

### 6.2.3 Radiation pattern measurements

The radiation pattern measurements were conducted in an anechoic chamber. The measurement system is shown in Fig.(6.6). The basic idea is as follows: the signal from generator is amplified, multiplied and delivered from the horn antenna to the



receiving LTCC antenna. Then, the signal is fed through a coaxial waveguide to the mixer and the low-frequency signal is detected by the spectrum analyzer. The antenna positioner is controlled by custom LabView software. The signal from the spectrum analyzer is also imported to LabView and the signal is stored in a computer memory.

The LTCC antenna-under-test with the test fixture was attached to the support made from Rohacell. The support was  $\sim 40\text{cm}$  tall which prevented the antenna positioner from disturbing the measurements. The antenna positioner provides adjustment of the antenna in the horizontal plane and rotation of the antenna with  $1/6000^\circ$  steps. The data was collected with  $1^\circ$  steps and E- and H-plane gain patterns were measured.

At the first stage, the whole test fixture was used in the measurements. However, it was noticed soon that the metal parts of the fixture caused lot of distortions to the results due to reflections and diffraction of the signal, although the fixture was covered with absorbing material. At the next stage, the fixture was taken into pieces and only one jaw of the jig was needed to provide a coaxial connection. The results with this arrangement were much more reliable. Illustrations of the E- and H-planes are shown in Fig.(6.7). It is seen that the E-plane cuts through the test fixture but there is no obstacles when measuring H-plane pattern. Metal parts near the antenna were covered with suitable absorbers.

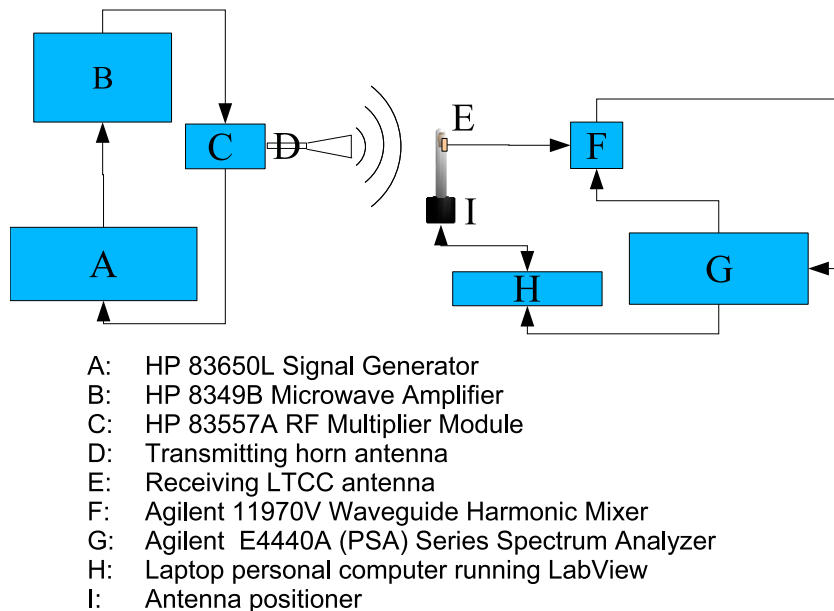


Figure 6.6: Radiation pattern measurement arrangement in an anechoic chamber.

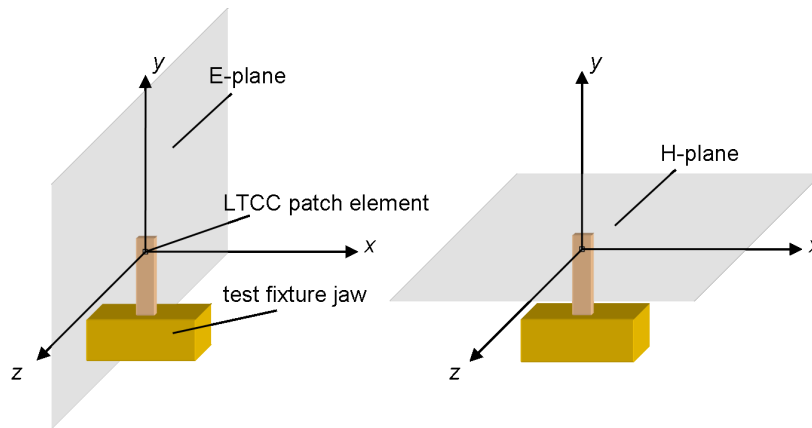


Figure 6.7: E- and H-planes of the LTCC microstrip antenna.

## 6.3 Results

In this Section, the simulation and measurement results for the S-parameters and radiation-pattern measurements are presented.

### 6.3.1 S-parameter results

In this Section, the S-parameter results are presented as functions of frequency: normalised input impedance on a Smith chart (normalisation to  $50\Omega$ ) and return loss in a rectangular graph.

The S-parameter results calculated with different simulation software are compared with each other: for the ACMPA1 in Fig.(6.8) and SCMPA1 in Fig.(6.9). It is seen that each method (MoM, FEM and FDTD) gives a bit different results. Differences between IE3D and HFSS results are due to zero metallization thickness used in the IE3D and finite metallization thicknesses used in the HFSS. Variations in metallization thickness alter the effective permittivity of the feed lines and patch, leading to differences in the characteristic impedance of the feed lines and resonance frequency of the antenna. However, IE3D and HFSS results are relatively similar but the results calculated with FDTD code deviate from the others. There is several possible reasons for this: 1) differences in dimensions of the antennas (see Table (6.1)) 2) metallizations had zero thicknesses 3) conductors were thought as PEC 4) excitation of the fields caused distortions at port locations 5) ABCs (Liao not PML) 6) smaller calculation space than used in HFSS. I would say the most critical part in FDTD code is the port definition. Now, the ports were modeled as rectangular coaxial ports. To minimize the discontinuity distortions, the ports should be defined

in a same manner as in the HFSS: transversal field distributions are calculated first for the feed line and then the field distribution is excited into the structure to be simulated.

Since HFSS simulation models are closest to the real structures (finite ground planes, substrate widths and metallization thickness), measured results are compared with HFSS simulation results from now on.

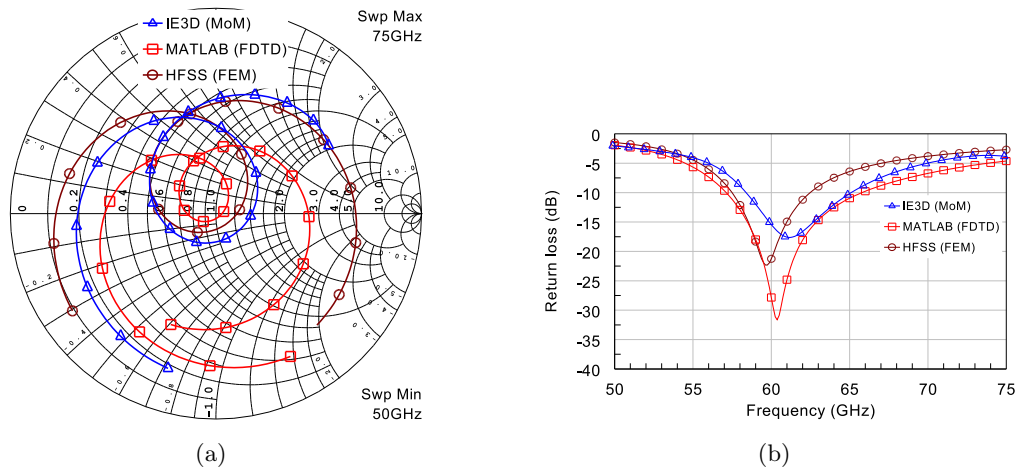


Figure 6.8: Simulated S-parameter results for ACMPA1: a) Normalised input impedance and b) return loss.

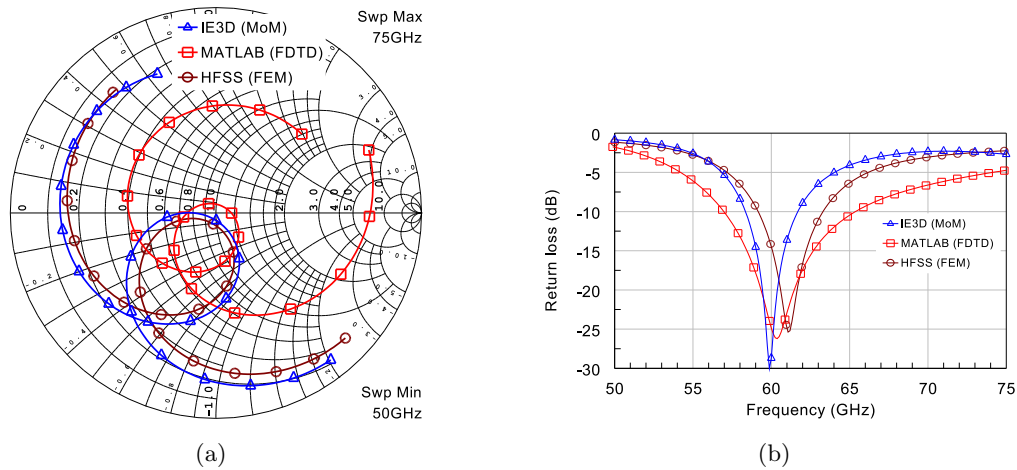


Figure 6.9: Simulated S-parameter results for the SCMPA1: a) normalised input impedance and b) return loss.

The normalised input impedance (normalised to  $50\Omega$ ) and return loss for SCMPA1, SCMPA2 and SCMPA3 are shown in Fig.(6.10), Fig.(6.11) and Fig.(6.12), respec-

tively. Simulation results are compared with the measured ones. After the dimensions of the manufactured antennas were checked, SCMPA structures were re-simulated with realised dimensions. It is seen that simulation results are more closer to the measured ones when the parameters are the same. The antenna resonance frequency is at the culmination point of the input impedance loop on the Smith chart. The best input matching occurs at frequency ( $f_{op}$ ) at which the input impedance loop is at the nearest distance from the center on the Smith chart, or at which the most negative decibel value of return loss is achieved. It is seen that for SCMPA1-3 the resonance frequency is close to the frequency of the best input matching. Measured return loss for SCMPA1-3 is worse than simulated. This is caused mainly by the errors in characteristic impedances of the CPWs in the measured antennas. With the realised CPW parameters the characteristic impedance was  $37\Omega$ , not the designed  $50\Omega$ . When comparing the results of SCMPA1, SCMPA2 and SCMPA3 with each other it is seen that input matching is improved when the slot length (and coupling) is increased. The best return loss for SCMPA2 is only  $-9.5$  dB while the one for SCMPA3 is  $-20$  dB. Increased coupling is seen as increased loop size on the Smith chart. Better input matching is a consequence of the loop closer to the center. Small differences in  $f_{op}$  are caused by  $39\mu\text{m}$  error in patch lengths. It can be also seen that the impedance bandwidth is quite narrow, in order of  $3.5\%$  for the SCMPA1. Simulated and measured values for the impedance bandwidth ( $BW_{imp}$ ), the best input matching frequency ( $f_{op}$ ) and the best return loss  $L_{ret}$  for SCMPA1-3 are summarised in Table (6.4).

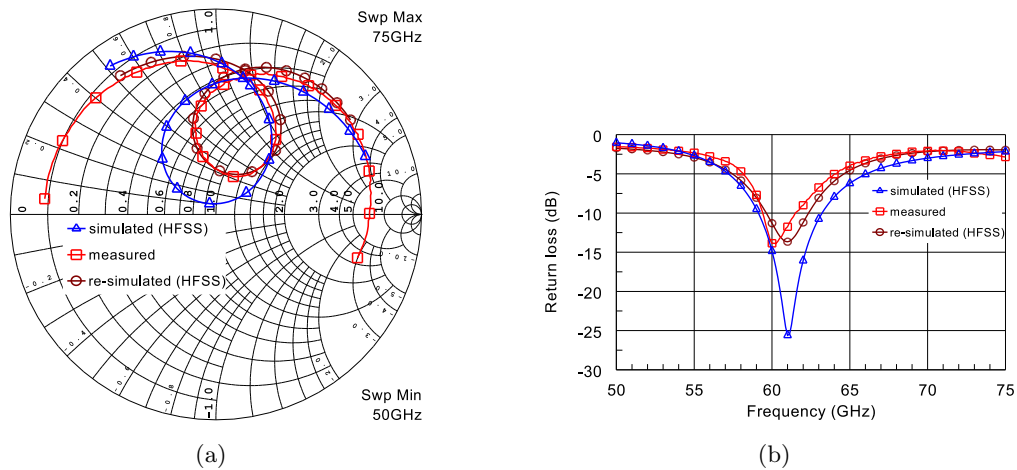


Figure 6.10: S-parameter results for the SCMPA1: a) normalised input impedance and b) return loss.

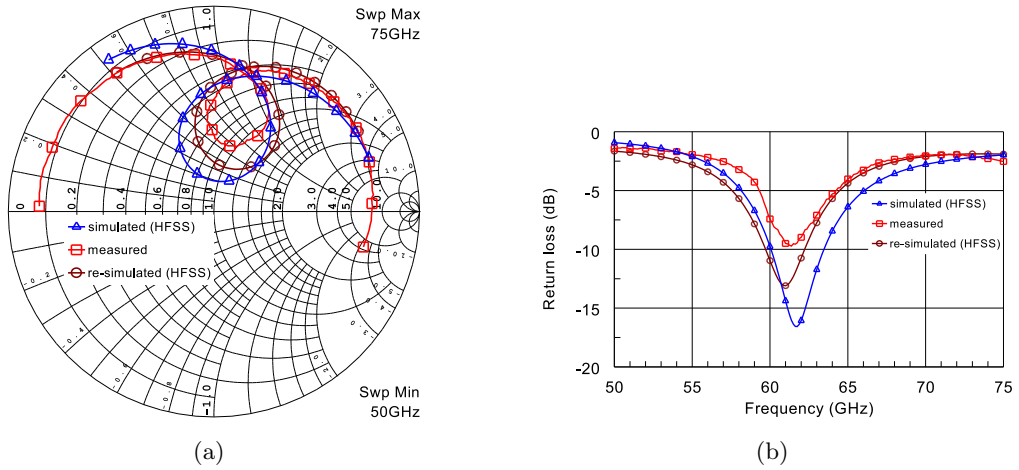


Figure 6.11: S-parameter results for the SCMPA2: a) normalised input impedance and b) return loss.

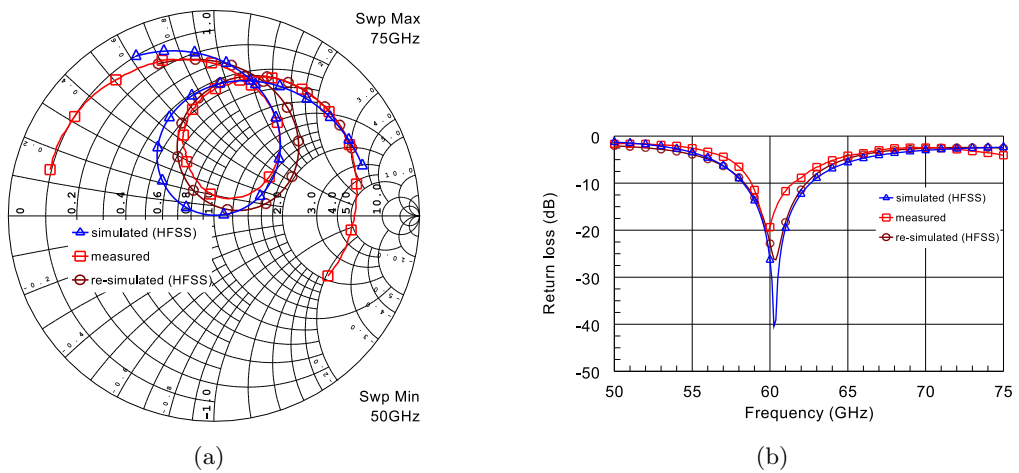


Figure 6.12: S-parameter results for the SCMPA3: a) normalised input impedance and b) return loss.

Table 6.4: Impedance characteristics of SCMPA antennas.

	SCMPA1		SCMPA2		SCMPA3	
	Simulated	Measured	Simulated	Measured	Simulated	Measured
$BW_{imp}(\%)$	6.7	3.5	5.7	-	7.3	4.3
$f_{op}$ (GHz)	61.1	60.1	61.7	61.3	60.3	59.8
$L_{ret}$ (dB)	-25.6	-14.1	-16.5	-9.6	-40.1	-20.4

The S-parameter results for ACMPA1, ACMPA2 and ACMPA3 are shown in Fig.(6.13), Fig.(6.14) and Fig.(6.15), respectively. Only original simulations are compared with the measurement because the lack of information of the realised parameters of the antennas. It is seen that input impedance loop on the Smith chart is smaller for the measured antennas than for the designed ones. The decreased loop size can be explained partly with smaller aperture size inside the substrate. In fact, if simulated results of ACMPA1 are compared with measured results of ACMPA3, it shows that input impedance loops are quite similar. This supports the idea that the aperture size has decreased during manufacturing process due to shrinking. Small differences in operating frequencies are caused by the errors in patch lengths.

The best measured input matching is achieved with the ACMPA3 and the best simulated input matching for the ACMPA1. The input impedance of the designed ACMPA1 was quite close to the center of the Smith chart at 60 GHz. As the aperture length is increased (ACMPA3) the input impedance loop increases and distance to the center increases leading to reduced input match. Tested ACMPA3 has the best input match because the input impedance loop is closer to the center of the Smith chart than for ACMPA1 or ACMPA2 antennas. Impedance characteristics for ACMPA1-3 are summarised in Table (6.5).

The scattering-parameter results for the SCGMPA1 are shown in Fig.(6.16). Due to longer uncalibrated GCPW feed in the manufactured SCGMPA1, there is ripple in the return loss graph. Ripple is seen as multiple loops rotating around the Smith chart and results are difficult to analyse. That is why the frequency sweep in the Smith chart graph is limited between 58...62 GHz. It is seen that both, simulated and measured SCGMPA1, have resonance frequency around 60 GHz. Return losses are in order of -24 dB and -34 dB for the simulated and measured antennas, respectively, at center frequencies. Much narrower impedance bandwidth of the measured

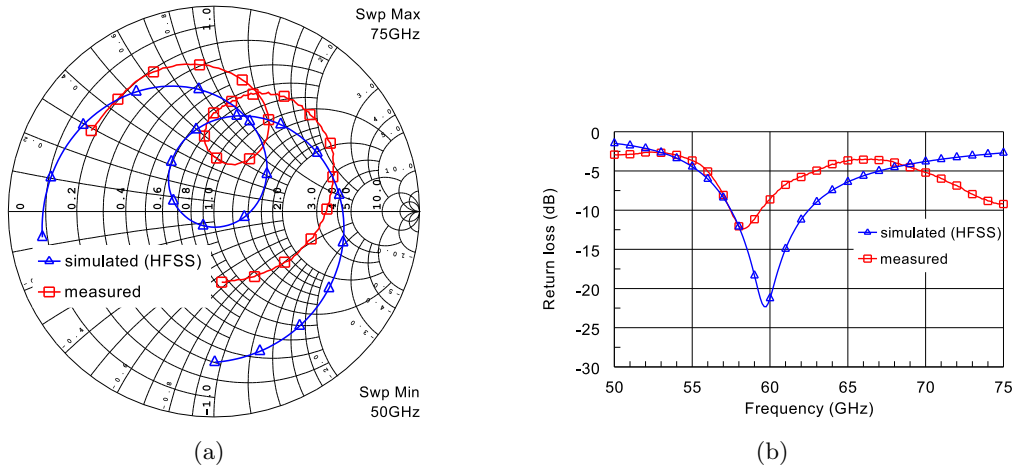


Figure 6.13: S-parameter results for the ACMPA1: a) normalised input impedance and b) return loss.

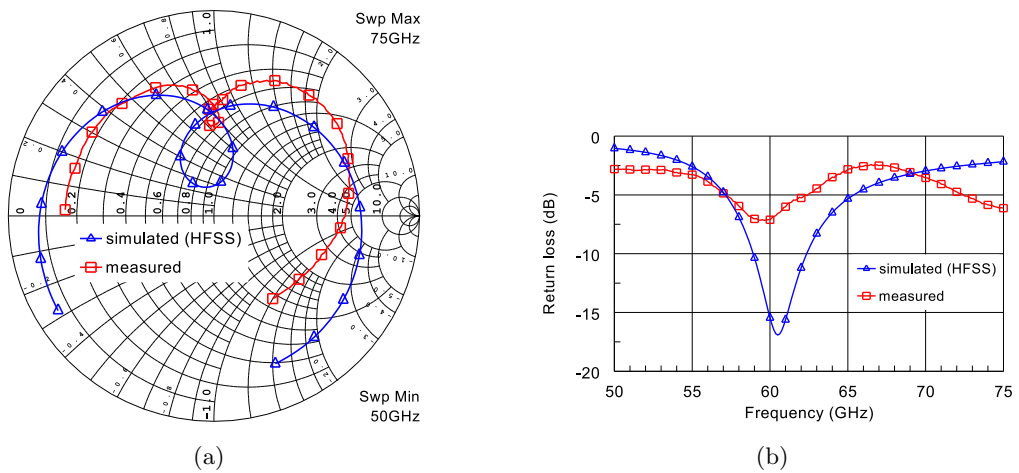


Figure 6.14: S-parameter results for the ACMPA2: a) normalised input impedance and b) return loss.

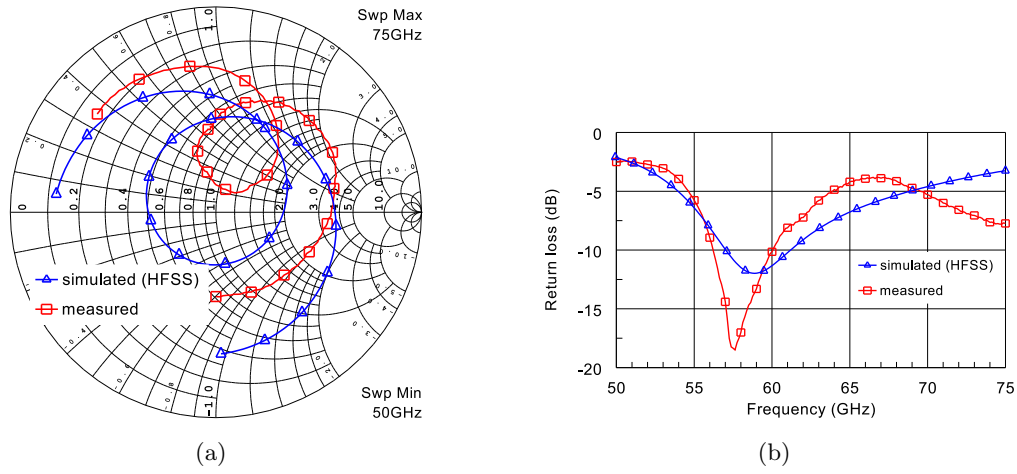


Figure 6.15: S-parameter results for the ACMPA3: a) normalised input impedance and b) return loss.

Table 6.5: Impedance characteristics of ACMPA antennas.

	ACMPA1		ACMPA2		ACMPA3	
	Simulated	Measured	Simulated	Measured	Simulated	Measured
$BW_{imp}(\%)$	8.6	3.3	5.8	-	7.1	6.6
$f_{op}$ (GHz)	59.6	58.3	60.5	59.4	58.9	57.6
$L_{ret}$ (dB)	-22.3	-12.3	-16.8	-7.2	-11.9	-18.4

antenna may be related to the lack of calibration and multiple reflections in the test fixture, although absorbers were used. In fact, it was seen when measuring radiation patterns that the fixture caused a lot of distortion to the results. So, it is obvious that also the S-parameter results are disturbed by the metal parts of the jig. However, the resonance and operating frequencies of SCGMPA1 seems to be close to which was designed. Impedance characteristics for SCGMPA1 are summarised in Table (6.6).

### 6.3.2 Radiation pattern results

In practise, the radiation characteristics are usually presented as gain patterns. The simulated normalised H-plane gain patterns for SCGMPA, SCEMPA and PCMPA are shown in Fig.(6.17) in polar and cartesian graphs. The SCEMPA has the lowest



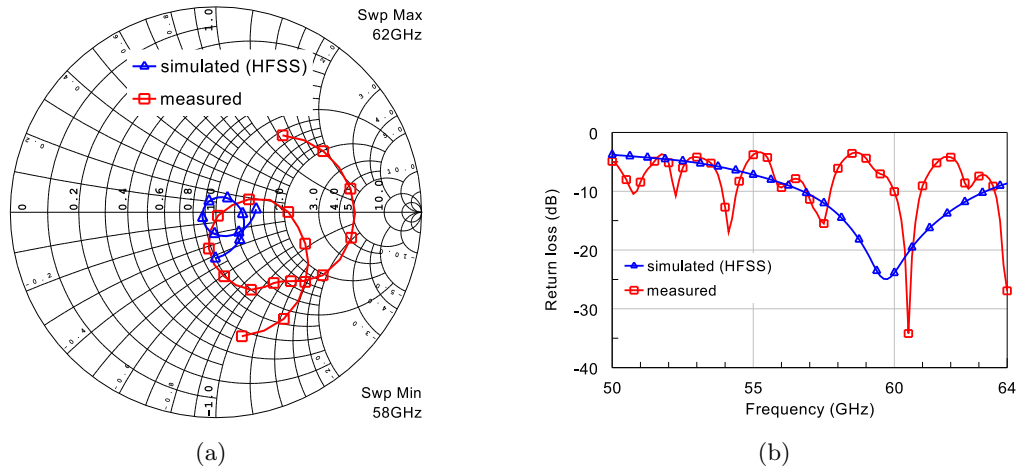


Figure 6.16: S-parameter results for the SCGMPA1: a) normalised input impedance and b) return loss.

Table 6.6: Impedance characteristics of the SCGMPA.

	SCGMPA1	
	Simulated	Measured
$BW_{imp}(\%)$	10.5	1.7
$f_{op}$ (GHz)	59.8	60.5
$L_{ret}$ (dB)	-24.2	-33.8

maximum gain value and the largest -3 dB beamwidth. Also, the back radiation level is larger than for SCGMPA1 or PCMPA1. The patterns for SCGMPA1 and PCMPA1 are quite similar. In the SCGMPA1, the additional ground plane was used to minimise the back radiation. The backlobe level is quite acceptable, approximately -17 dB. However, even smaller backlobe level, -21 dB, is achieved with the PCMPA1. Radiation characteristics for SCGMPA, SCEMPA and PCMPA are summarised in Table (6.7) using variables: maximum absolute gain,  $G_{max}$ , -3 dB beamwidth,  $bw_{-3dB}$  and backlobe level,  $bl$ .

As it was mentioned earlier, gain for the SCGMPA1 was measured in two planes, E- and H-planes. The frequency at which the data was stored was determined as the frequency at which the largest amplitude of the received signal occurred. Thus, the gain patterns were stored at 59.5 GHz frequency. It was tested few times that there was enough absorbers and excess reflections were minimised. The simulated and

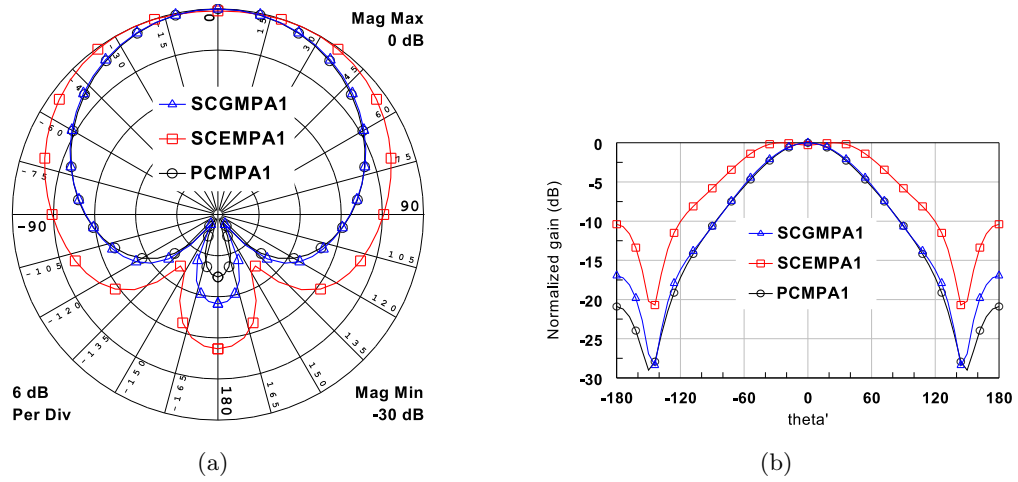


Figure 6.17: Simulated normalised H-plane gain for SCGMPA, SCEMPA and PCMPA: a) in polar form and b) in cartesian form. Simulated with HFSS (FEM).

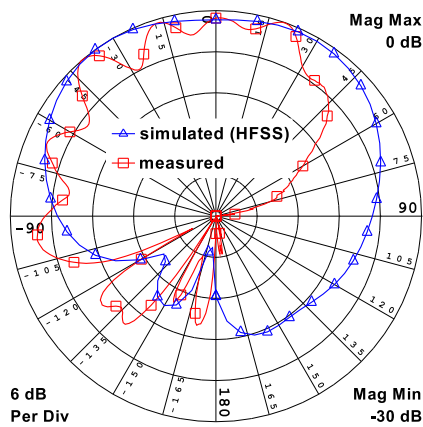
Table 6.7: H-plane radiation characteristics.

	SCGMPA1	SCEMPA1	PCMPA1
$G_{max}$ (dB)	3.5	2.9	4.3
$bw_{-3dB}$ ( $^\circ$ )	85.4	138	85.4
$bl$ (dB)	-17.2	-10.6	-21.2

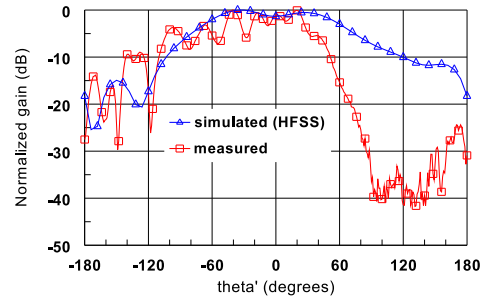
measured E- and H-plane gain patterns are presented in Fig.(6.18) and Fig.(6.19). The gain values are normalised to their maximum. Result are presented as a function of angle  $\theta'$ . In E-plane the angle  $\theta'$  goes from  $-180^\circ \dots 0^\circ$ , when  $y \geq 0$  and from  $0^\circ \dots 180^\circ$ , when  $y \leq 0$ . In the H-plane the angle  $\theta'$  goes from  $-180^\circ \dots 0^\circ$ , when  $x \geq 0$  and from  $0^\circ \dots 180^\circ$ , when  $x \leq 0$ .

The simulated E-plane gain is unsymmetrical due to radiation of the CPW feed. This is seen as increased gain value at angles  $0^\circ \dots 180^\circ$ . Measured E-plane gain is very noisy and even more unsymmetrical than simulated. Ripple at angles  $-180^\circ \dots 0^\circ$  is caused by multiple reflections from the metal parts. Reflections cause interference minimum and maximum to occur at particular values of  $\theta'$ . Because the antenna was rotated at constant speed the minimum and maximum values of interference appear with almost at constant shifts in rotation angle. When  $30^\circ \leq \theta' \leq 180^\circ$ , the gain results were disturbed by the shading of the fixture. This was a thing that could not be solved because the test fixture was necessary to conduct the measurements.

The simulated and measured gain results in the H-plane gain are quite similar. The measurement arrangement was rotationally symmetrical, i.e. the background remained constant as antenna was rotated. Measured results seem to have succeeded well and even the back radiation fits well with the simulation. However, there is small deviation between the results at angles  $-120^\circ \leq \theta' \leq -80^\circ$  and  $80^\circ \leq \theta' \leq 120^\circ$ . The deviation is probably caused by the reflections of the fixture. The disturbance of the pattern seems to be strongest when the signal is reflected from the corners of the fixture. The backlobe level,  $bl$ , is about -17 dB.

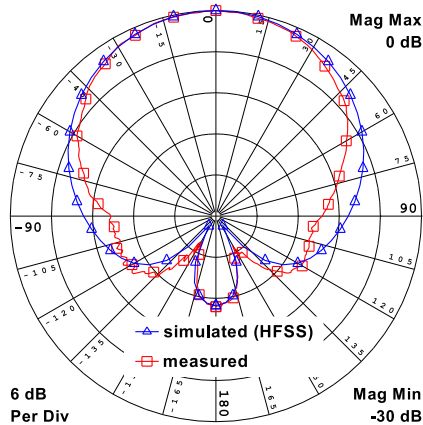


(a)

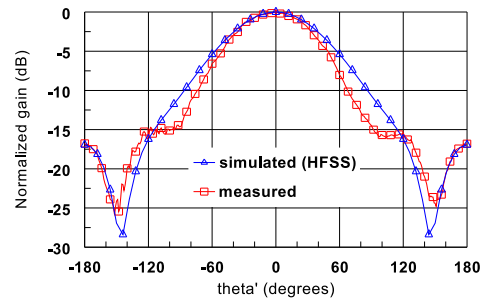


(b)

Figure 6.18: SCGMPA1 E-plane normalised gain: a) in polar form and b) in cartesian form.



(a)



(b)

Figure 6.19: SCGMPA1 H-plane normalised gain: a) in polar form and b) in cartesian form.

In this Chapter, some practical issues related to simulations were first considered. Also, the MATLAB FDTD code written by the author was described. Then, the prototype test measurements for the manufactured antennas were presented. The measurements consisted of checking the realised dimensions of the antennas with the microscope, scattering parameter measurements on probe station and with the test fixture, and radiation pattern measurement for LTCC antenna connected to the test fixture. The end of the Chapter concentrated on the simulation and measurement results. It was seen that simulations with different numerical methods agreed quite well with each others. Differences in the results are mainly caused by differences in simulation parameters (dimensions of the antennas). Measured scattering-parameter results could be predicted from the simulated ones. Differences between simulation and measurement results were caused by shrinking of the antenna structures in the LTCC process. Radiation characteristics of one type of antenna was verified in an anechoic chamber. The simulated normalised gain in E- and H-planes was compared with the measured one. It was seen that in E-plane the test fixture caused distortions to the radiation pattern, but the results were almost identical in H-plane. These results encourage to proceed the measurements also with the other designed antenna structures, SEMPAs and PCMPAs, as soon as they are manufactured.

## Chapter 7

# Conclusions

In this work, antenna configurations for the steerable-beam array operating at 60 GHz frequency band were studied. The goal was to select, design, model and test a set of antennas operating at 60 GHz band and fabricated with LTCC technology. The boundary conditions for the whole work were determined mainly by the capabilities and tolerances of the LTCC technology, and the measurement facilities for testing the input matching and radiation characteristics of the antennas.

First, antenna topologies suitable for LTCC processing and 60 GHz frequency band were investigated. The microstrip antenna was considered as the most applicable candidate due to its versatile design characteristics. Several feeding mechanisms enable tuning of the input impedance without additional matching stubs or circuits. Several aperture-, slot- and proximity-coupled microstrip antennas were selected for the work. In addition to the simpler models that were able to be tested with an on-wafer probe station, antennas with some modifications were designed in order to conduct the radiation pattern measurements with a test fixture.

Modelling of the antennas was conducted by using commercial numerical full-wave software based on MoM and FEM. The purpose was to validate the design using different numerical approaches, and use the most suitable software for each antenna structure. There was also an interest to simulate the antennas starting from the Maxwell's equations, and an FDTD code for scattering-parameter calculation was also implemented in MATLAB by the author.

The input matching of the antennas was tested with an on-wafer probe station. Modified structures were designed to be tested with a test fixture, which enables the transitions from the coaxial waveguide to the microstrip line or to the CPW. Gain patterns for the slot-coupled microstrip antenna were measured in E- and H-planes.

It was seen that different numerical methods gave slightly different results, mainly due to somewhat different simulation parameters. There is a need to improve the FDTD code for more accurate modeling of the antenna geometries and excitations of the fields. There were deviations between the simulated and measured scattering parameters. The realised dimensions of the slot-coupled antennas were checked with a microscope and it was noticed that the differences in the results were caused by the shrinking of the antennas in the LTCC process. It can be assumed that in the future, as the number of processing repetitions increases, the shrinking of the conductors and spacing can be predicted more accurately. The E-plane gain pattern was strongly distorted by the metal parts of the test fixture. In the H-plane, the simulated and measured gain agreed well with each other and only minimal amount of distortion was perceived. In order to minimise the distortions, a small special connector that provides the coaxial-to-microstrip line or coaxial-to-CPW transitions, should be used. At millimetre-wave frequencies, such as 60 GHz, there is not many providers for these types of connectors and they are quite expensive. At least at this stage, the test fixture available at VTT Information Technology fulfills our needs for testing purposes.

As a summary of the results, it is clearly seen that microstrip antennas even at 60 GHz frequency band can be manufactured with LTCC technology and several of the presented configurations can be used as array elements. Perhaps the best candidates are the slot-coupled and proximity-coupled microstrip antennas. The slot-coupled patch can be easily integrated with active circuits and proximity-coupling provides large impedance bandwidth and low back-radiation level.

Reliable results are achieved with commercial simulation software, but basic understanding of the electromagnetic behaviour of the structure to be simulated is usually needed. The designer has to be also aware of the software-related issues, such as the port definition and boundary conditions, in order to properly model the real environment of the antenna. Implementing a FDTD simulation code is a good way to deepen the understanding of the electromagnetic behaviour of the antennas, and time-stepped field animations give valuable information about the field dynamics. There are few things that could be improved in the MATLAB FDTD code. First, the transversal field distribution of the feed lines should be used as excitation fields of the simulations. Secondly, if the perfectly matched layer (PML) boundary conditions were used, the reflections at the boundaries of the calculation grid would be minimised. With non-uniform grid the number of cells in the grid would be diminished and smaller cells could be used at critical regions, i.e. at which the amplitude variations of the fields are the strongest. With more careful preparation of the code,

the simulation time could be decreased significantly. In the near future, the new antenna structures will be tested as soon as they are fabricated. It is known from the preliminary inspections that the dimensions of the new antennas are more close to the designed values, which indicates even better test results. Testing facilities are developed to obtain more accurate and simpler positioning of the antennas when measuring radiation patterns. In future, an array will be designed and fabricated on LTCC. Beam steering will be demonstrated with an array integrated with active phase shifters. First, a linear array is designed and perhaps later the antennas are placed in a planar array. Hopefully in future, the array will be integrated with active circuits in order to build a radio transceiver for wireless communications, operating at 60 GHz frequency band with data speed of 1 Gbit/s.

# REFERENCES

- Agilent Technologies. 2001. *Network Analysis-Applying the HP 8510 TRL Calibration for Non-Coaxial Measurements*. Included with the measurement facility. Product Note 8510-8.
- Anritsu Wiltron. 2005 (November). *3680 Series Universal Test Fixtures*. Web resource. <http://www.us.anritsu.com/downloads/files/11410-00024.pdf>.
- Ansoft. 2001. *HFSS 8.0.22 Maxwell Online Help System*. Included with software.
- Balanis C.A. 1997. *Antenna Theory, Analysis and Design*. 2nd edn. John Wiley and Sons, Inc.
- Bhobe A.U., Holloway C.L., Picket-May M., & Hall R. 2004. Wide-band slot antennas with CPW feed lines: hybrid and log-periodic designs. *IEEE Transactions on Antennas and Propagation*, **52**, 2545–2554.
- Doan C.H., Emami S., D.A. Sobel, Niknejad A.M., & Brodersen R.W. 2004. Design considerations for 60 GHz CMOS radios. *IEEE Communications Magazine*, **12**, 132–140.
- Gao S.S., & Sambell A. 2005. Dual-polarized broad-band microstrip antennas fed by proximity coupling. *IEEE Transactions on Antennas and Propagation*, **53**, 526–530.
- Harrington R.E. 1968. *Field Computation by Moment Methods*. New York: Macmillan.
- Hoffmann R.K. 1987. *Handbook of Microwave Integrated Circuits*. Artech House Inc.
- Huang Y., Wu K.-L., Fang D.-G., & Ehlert M. 2005. An integrated LTCC millimeter-wave planar array antenna with low-loss feeding network. *IEEE Transactions on Antennas and Propagation*, **53**, 1232–1234.



- IEEE. 1979. *IEEE standard test procedures for antennas*. International standard Std 149-1979. Antenna Standards Committee of the IEEE Antennas and Propagation Group, 345 East 47th Street, New York, NY 10017-2394, USA.
- IEEE. 1993. *IEEE standard definitions of terms for antennas*. International standard Std 145-1993. The Institute of Electrical and Electronics Engineers, Inc., 345 East 47th Street, New York, NY 10017-2394, USA.
- Kraus J.D. 2002. *Antennas for All Applications*. 3rd edn. McGraw Hill.
- Kulke R., Rittweger M., Uhlig P., & Günner C. 2005 (November). *LTCC - Multilayer Ceramic for Wireless and Sensor Applications*. Web resource. <http://www.taconic-add.com/pdf/technicalarticles--ltccmultilayer.pdf>.
- Kumar G., & Ray K.P. 2003. *Broadband Microstrip Antennas*. Artech House Inc.
- Lehto A., & Räsänen A. 2002a. *Millimetriaaltotekniikka*. 2nd edn. Otatiето.
- Lehto A., & Räsänen A. 2002b. *RF- ja mikroaaltotekniikka*. 7th edn. Otatiето.
- Lindell I. 1997. *Aaltojohtoteoria*. 2nd edn. Otatiето.
- Lindell I., & Nikoskinen K. 1995. *Antenniteoria*. 4th edn. Otatiето.
- Lindell I., & Nikoskinen K. 2003. *Sähkömagnetiikka*. Lecture material. Department of Electrical and Communications Engineering, Helsinki University of Technology.
- Newman E.H., & Tulyathan P. 1981. Analysis of microstrip antennas using method of moments. *IEEE Transactions on Antennas and Propagation*, **29**, 47–53.
- Nikoskinen K. 2004. *Antenniteoria*. Lecture material. Department of Electrical and Communications Engineering, Helsinki University of Technology.
- Nikoskinen K., & Kärkkäinen K. 2004. *Numeerinen sähkömagnetiikka*. Lecture material. Department of Electrical and Communications Engineering, Helsinki University of Technology.
- Ohata K., Maruhashi K., Ito M., Kishimoto S., Ikuina K., Hashiguchi T., Ikeda K., & Takahashi N. 2002. 1.25 Gbps wireless gigabit ethernet link at 60 GHz-band. *In: IEEE Radio Frequency Integrated Circuits Symposium*.

- Pozar D. M., Duffy S. M., Targonski S. D., & Herscovici N. 2000. A comparison of commercial software packages for microstrip antenna analysis. *In: IEEE International Symposium on Antennas and Propagation.*
- Pozar D.M. 1992. Microstrip antennas. *Proceedings of the IEEE*, **80**, 79–102.
- Riaziat M., Majidi-Ahy R., & Feng I-J. 1990. Propagation modes and dispersion characteristics of coplanar waveguide. *IEEE Transactions on Microwave Theory and Techniques*, **38**, 245–251.
- Räisänen A., & Lehto A. 2001. *Radiotekniikan perusteet*. 10th edn. Otatiето.
- Seki T., Honma N., Nishikawa K., & Tsunekawa K. 2005. A 60-GHz multilayer parasitic microstrip array antenna on LTCC substrate for system-on-package. *IEEE Microwave and Wireless Components Letters*, **15**, 339–341.
- Sierra-Garcia S., & Laurin J.-J. 1999. Study of a CPW inductively coupled slot antenna. *IEEE Transactions on Antennas and Propagation*, **47**, 58–64.
- Sihvola A., & Lindell I. 1996. *Sähkömagneettinen kenttäteoria 2. Dynaamiset kentät*. 2nd edn. Otatiето.
- Sturzebecher D., Leen J., Cadotte R., DeMarco J., Ni T.-D., Higgins T., Popick M., & Cummings M. 1996. 20 GHz LTCC phased array module. *IEEE MTT-S Digest*, 991–994.
- Taflove A., & Hagness S.C. 2000. *Computational Electrodynamics: The Finite-Difference Time-Domain Method*. 2nd edn. Artech House Inc.
- Venot Y., & Wiesbeck W. 2003. 76.5 GHz radar sensor for contact-free distance measurement with micrometer accuracy. *Proceedings of the IEEE*, 216–221.
- Volakis J.L., Chatterjee A., & Kempel L.C. 1998. *Finite Element Method for Electromagnetics: Antennas, Microwave Circuits, and Scattering Applications*. IEEE Press.
- VTT Electronics. 2005a (November). *Fine-Line Screen Printing in LTCC*. Web resource. [http://www.vtt.fi/ele/research/ope/pdf/fine\\_line\\_screen\\_printing.pdf](http://www.vtt.fi/ele/research/ope/pdf/fine_line_screen_printing.pdf).
- VTT Electronics. 2005b (November). *LTCC tape material data*. Web resource. <http://www.vtt.fi/ele/research/ope/pdf/tapematerial.pdf>.

- Yamada A., Suematsu E., Sato K., Yamamoto M., & Sato H. 2000. 60 GHz ultra compact transmitter/receiver with a low phase noise PLL-oscillator. *IEEE MTT-S Digest*, 2035–2038.
- Yee K.S. 1966. Numerical Solution of Initial Boundary Value Problems Involving Maxwell's Equations in Isotropic media. *IEEE Transactions on Antennas and Propagation*, **14**, 302–307.
- Yee K.S. 1988. A Selective Survey of Computational Electromagnetics. *IEEE Transactions on Antennas and Propagation*, **36**, 1281–1305.
- Zeland. 2004. *IE3D User's Manual: Release 10.2*. Included with software.

# Appendix A

## Matlab FDTD code

```
% This program simulates the aperture-coupled microstrip-line-fed patch
% antenna. Microstrip line is fed by 50 ohm rectangular coaxial waveguide.
% Gaussian pulse is used as a voltage source in coaxial cable.
% Mur1-absorbing boundary condition is used for coaxial cable and Liao (N=3)
% abc for three-dimensional antenna structure. Metal parts are considered as
% perfect electric conductor. Dielectric material is thought as lossless.
%
% Program calculates the S11-parameters and stores them into a matrix. Antenna
% input impedance is also calculated. Results are stored into the file
% "ms_fed_patch.mat".
%
% Antti Lamminen
% TTE/VTT, 3.12.2005

clear;
% Number of time steps
steps = 3000;
% Dimensions of a grid cell
dx = 25e-6;
dy = 75e-6;
dz = 50e-6;
s_param = [];
% Frequency band for Fourier transform
f=45e9:0.125e9:75e9;
% Voltage vectors for incident and reflected signals
Uinc = zeros(size(f));
Uref = zeros(size(f));
% Permeability ...
mu0 = 4*pi*1e-7;
% and permittivity of free space
eps0 = 8.85419e-12;
% Speed of light in a vacuum
c0 = 1/sqrt(eps0*mu0);
% Relative permittivity of the substrate
er = 5.99;
% Interface between air and substrate
epsmean = (eps0+eps0*er)/2;
% Time step
dt = 1/(c0*sqrt((1/(dx^2))+1/(dy^2))+1/(dz^2)));
```

```

% ----- One-dimensional simulation for coaxial feed -----%

% First component is current and the last is voltage
Usize = 50;
Isize = 50;
% Vectors forming the calculation grid
U = zeros(Usize,1);
I = zeros(Isize,1);
% Time-dependent incident signals
Uinct = zeros(Usize,1);
Iinct = zeros(Isize,1);
% Constant used in Mur abc
abcy = (c0*dt-dy)/(c0*dt+dy);
% Current calculated in 3D - space
I3D = 0;
% Characteristic impedance of the coaxial feed line
ZO = 50;
% Ci and Cu are used when calculating current and voltage, respectively
Ci = (1/ZO)*(c0*dt/dy);
Cu = ZO*(c0*dt/dy);
% Source is located in the middle of the coaxial line
srcp = Usize/2;
% Gaussian pulse is used as a source. FWHM is 48 time steps
% checked that -3dB bandwidth is ~75 GHz
pulsewidth = 48;
source = exp(-(((1:steps)-3*pulsewidth).^2./((pulsewidth/2)^2/log(2))));

% -----%

% ----- Three - dimensional simulation of the patch -----%

% Size of the grid, 144000 cells
xsize = 120; ysize = 40; zsize = 30;
% Port location in y-direction in the 3D grid
dem = 0.45e-3/dy;
% Substrate thicknesses
t = 100e-6; % for microstrip line
h = 300e-6; % for patch element
% z-coordinate of the microstrip line
msz = 0.5e-3/dz;
% z-coordinate of the ground plane
gndz = msz + t/dz;
% z-coordinate of antenna element
antz = gndz + h/dz;
% Edges of the patch (L = left, R = right, F = front, B = back)
mLL = 45;
mLR = 76;
mLF = 17;
mLB = 25;
% Grids for the field components
Ex = zeros(ysize+1, xsize, zsize+1);
Ey = zeros(ysize, xsize+1, zsize+1);
Ez = zeros(ysize+1, xsize+1, zsize);
Hx = zeros(ysize, xsize+1, zsize);
Hy = zeros(ysize+1, xsize, zsize);
Hz = zeros(ysize, xsize, zsize+1);
Cax = zeros(ysize+1,xsize+1,zsize+1);
Cay = zeros(ysize+1,xsize+1,zsize+1);
Caz = zeros(ysize+1,xsize+1,zsize+1);
Dax = zeros(ysize+1,xsize+1,zsize+1);
Day = zeros(ysize+1,xsize+1,zsize+1);
Daz = zeros(ysize+1,xsize+1,zsize+1);

```

```

% These are used when calculating E- and H-components
Cax(:,:,1:msz-1) = dt/(eps0*dx); % Air
Cax(:,:,msz) = dt/(epsmean*dx); % Interface
Cax(:,:,msz+1:antz-1) = dt/(eps0*er*dx); % Substrate
Cax(:,:,antz) = dt/(epsmean*dx); % Interface
Cax(:,:,antz+1:end) = dt/(eps0*dx); % Air
Cay(:,:,1:msz-1) = dt/(eps0*dy); % Air
Cay(:,:,msz) = dt/(epsmean*dy); % Interface
Cay(:,:,msz+1:antz-1) = dt/(eps0*er*dy); % Substrate
Cay(:,:,antz) = dt/(epsmean*dy); % Interface
Cay(:,:,antz+1:end) = dt/(eps0*dy); % Air
Caz(:,:,1:msz-1) = dt/(eps0*dz); % Air
Caz(:,:,msz) = dt/(epsmean*dz); % Interface
Caz(:,:,msz+1:antz-1) = dt/(eps0*er*dz); % Substrate
Caz(:,:,antz) = dt/(epsmean*dz); % Interface
Caz(:,:,antz+1:end) = dt/(eps0*dz); % Air
% Permeability is thought as constant, mu0, in whole space
Dax(:,:,:) = dt/(mu0*dx);
Day(:,:,:) = dt/(mu0*dy);
Daz(:,:,:) = dt/(mu0*dz);
% Liao (N = 3) absorbing boundary condition is used. It requires four field
% values from four previous time points to be stored in a memory. The first
% two letters denote the field component. The next letter denotes the
% placement of the boundary: L = left, R = right, F = front, B = back, T =
% top, Bo = bottom. Number defines the the time point, 0 is the newest and
% 3 is the oldest.
EyL0 = zeros(ysize, 4, zsize+1);
EyL1 = zeros(ysize, 4, zsize+1);
EyL2 = zeros(ysize, 4, zsize+1);
EyL3 = zeros(ysize, 4, zsize+1);
EzL0 = zeros(ysize+1, 4, zsize);
EzL1 = zeros(ysize+1, 4, zsize);
EzL2 = zeros(ysize+1, 4, zsize);
EzL3 = zeros(ysize+1, 4, zsize);
EyR0 = zeros(ysize, 4, zsize+1);
EyR1 = zeros(ysize, 4, zsize+1);
EyR2 = zeros(ysize, 4, zsize+1);
EyR3 = zeros(ysize, 4, zsize+1);
EzR0 = zeros(ysize+1, 4, zsize);
EzR1 = zeros(ysize+1, 4, zsize);
EzR2 = zeros(ysize+1, 4, zsize);
EzR3 = zeros(ysize+1, 4, zsize);
ExF0 = zeros(4, xsize, zsize+1);
ExF1 = zeros(4, xsize, zsize+1);
ExF2 = zeros(4, xsize, zsize+1);
ExF3 = zeros(4, xsize, zsize+1);
EzF0 = zeros(4, xsize+1, zsize);
EzF1 = zeros(4, xsize+1, zsize);
EzF2 = zeros(4, xsize+1, zsize);
EzF3 = zeros(4, xsize+1, zsize);
ExB0 = zeros(4, xsize, zsize+1);
ExB1 = zeros(4, xsize, zsize+1);
ExB2 = zeros(4, xsize, zsize+1);
ExB3 = zeros(4, xsize, zsize+1);
EzB0 = zeros(4, xsize+1, zsize);
EzB1 = zeros(4, xsize+1, zsize);
EzB2 = zeros(4, xsize+1, zsize);
EzB3 = zeros(4, xsize+1, zsize);
Ext0 = zeros(ysize+1, xsize, 4);
Ext1 = zeros(ysize+1, xsize, 4);
Ext2 = zeros(ysize+1, xsize, 4);
Ext3 = zeros(ysize+1, xsize, 4);
Eyt0 = zeros(ysize, xsize+1, 4);

```

```

EyT1 = zeros(ysize, xsize+1, 4);
EyT2 = zeros(ysize, xsize+1, 4);
EyT3 = zeros(ysize, xsize+1, 4);
ExBo0 = zeros(ysize+1, xsize, 4);
ExBo1 = zeros(ysize+1, xsize, 4);
ExBo2 = zeros(ysize+1, xsize, 4);
ExBo3 = zeros(ysize+1, xsize, 4);
EyBo0 = zeros(ysize, xsize+1, 4);
EyBo1 = zeros(ysize, xsize+1, 4);
EyBo2 = zeros(ysize, xsize+1, 4);
EyBo3 = zeros(ysize, xsize+1, 4);
% Left side (y,z)
EyLif = 0;
EzLif = 0;
% Right side (y,z)
EyRif = 0;
EzRif = 0;
% Top side (y,x)
ExTif = 0;
EyTif = 0;
% Bottom side (y,x)
ExBoif = 0;
EyBoif = 0;
% Front side (x,z)
ExFif = 0;
EzFif = 0;
% Back side (x,z)
ExBif = 0;
EzBif = 0;
%Left side (y,z)
HyLif = 0;
HzLif = 0;
%Right side (y,z)
HyRif = 0;
HzRif = 0;
% Top side (y,x)
HxTif = 0;
HyTif = 0;
% Bottom side (y,x)
HxBoif = 0;
HyBoif = 0;
% Front side
HxFif = 0;
HzFif = 0;
% Back side
HxBif = 0;
HzBif = 0;

%-----%

% ----- Time-stepping-loop begins -----%

for t = 1:steps,

% Previous voltage and current vectors stored for Mur abs
I_prev = I;
Iinct_prev = Iinct;
Uinct_prev = Uinct;
% Previous field components for Liao abs
EyL2 = EyL1;
EyL1 = EyL0;
EyL0 = Ey(:,1:4,:);
EzL2 = EzL1;

```

```

EzL1 = EzL0;
EzL0 = Ez(:,1:4,:);
EyR2 = EyR1;
EyR1 = EyR0;
EyR0 = Ey(:,xsize-2:xsize+1,:);
EzR2 = EzR1;
EzR1 = EzR0;
EzR0 = Ez(:,xsize-2:xsize+1,:);
ExF2 = ExF1;
ExF1 = ExF0;
ExF0 = Ex(1:4,.,.);
EzF2 = EzF1;
EzF1 = EzF0;
EzF0 = Ez(1:4,.,.);
ExB2 = ExB1;
ExB1 = ExB0;
ExB0 = Ex(ysize-2:ysize+1,.,.);
EzB2 = EzB1;
EzB1 = EzB0;
EzB0 = Ez(ysize-2:ysize+1,.,.);
ExT2 = ExT1;
ExT1 = ExT0;
ExT0 = Ex(:,.,zsize-2:zsize+1);
EyT2 = EyT1;
EyT1 = EyT0;
EyT0 = Ey(:,.,zsize-2:zsize+1);
ExBo2 = ExBo1;
ExBo1 = ExBo0;
ExBo0 = Ex(:,.,1:4);
EyBo2 = EyBo1;
EyBo1 = EyBo0;
EyBo0 = Ey(:,.,1:4);

% Finite-difference expressions for magnetic field components
Hx(1:ysize,2:xsize,1:zsize) = Hx(1:ysize,2:xsize,1:zsize) + ...
    Dax(1:ysize,2:xsize,1:zsize).*(Ey(1:ysize,2:xsize,2:zsize+1) - Ey(1:ysize,2:xsize,1:zsize)) + ...
    Day(1:ysize,2:xsize,1:zsize).*(Ez(1:ysize,2:xsize,1:zsize) - Ez(2:ysize+1,2:xsize,1:zsize));

Hy(2:ysize,1:xsize,1:zsize) = Hy(2:ysize,1:xsize,1:zsize) + ...
    Dax(2:ysize,1:xsize,1:zsize).*(Ez(2:ysize,2:xsize+1,1:zsize) - Ez(2:ysize,1:xsize,1:zsize)) + ...
    Day(2:ysize,1:xsize,1:zsize).*(Ex(2:ysize,1:xsize,1:zsize) - Ex(2:ysize,1:xsize,2:zsize+1));

Hz(1:ysize,1:xsize,2:zsize) = Hz(1:ysize,1:xsize,2:zsize) + ...
    Day(1:ysize,1:xsize,2:zsize).*(Ex(2:ysize+1,1:xsize,2:zsize) - Ex(1:ysize,1:xsize,2:zsize)) + ...
    Dax(1:ysize,1:xsize,2:zsize).*(Ey(1:ysize,1:xsize,2:zsize) - Ey(1:ysize,2:xsize+1,2:zsize));

% Current flowing on a microstrip line is calculated from magnetic field
I3D = sum(Hz(dem,57,msz-1:msz+1))*dz + sum(Hx(dem,57:65,msz+1))*dx - ...textcolorcomment
    sum(Hz(dem,64,msz-1:msz+1))*dz - sum(Hx(dem,57:65,msz-2))*dx;

% Finite-difference expressions for current taking the antenna structure
% into account
I(2:Isize) = I(2:Isize) - Ci*(U(2:Usize)-U(1:Usize-1));
% Finite-difference expressions for current caused by incident signal
Iinct(2:Isize) = Iinct(2:Isize) + Ci*(Uinct(1:Usize-1) - Uinct(2:Usize));
% Mur abc
I(1) = I_prev(2) + abcy*(I(2) - I_prev(1));
Iinct(1) = Iinct_prev(2) + abcy*(Iinct(2) - Iinct_prev(1));
% Finite-difference expressions for voltage taking the antenna structure
% into account
U(1:Usize-1) = U(1:Usize-1) + Cu*(I(1:Isize-1) - I(2:Isize));
% Finite-difference expressions for voltage caused by incident signal

```



```

Uinct(1:Usize-1) = Uinct(1:Usize-1) + Cu*(Iinct(1:Isize-1) - Iinct(2:Isize));
% Mur abc
Uinct(Usize) = Uinct_prev(Usize-1) + abc*(Uinct(Usize-1) - Uinct_prev(Usize));
% The last voltage is calculated using the current in 3D-space
U(Usize) = U(Usize) + Cu*(I(Isize) - I3D);
% Sources for simulations
Uinct(srcp) = Uinct(srcp) + source(t);
U(srcp) = U(srcp) + source(t);
% Fourier transforms of reflected and incident voltages for spectral
% analysis
Uref = Uref + (U(srcp-5)-Uinct(srcp-5))/(2*pi)*exp(-i*2*pi*f*t*dt)*dt;
Uinc = Uinc + Uinct(srcp-5)/(2*pi)*exp(-i*2*pi*f*t*dt)*dt;

% Finite-difference expressions for electric field components

Ex(2:ysize,1:xsize,2:zsize) = Ex(2:ysize,1:xsize,2:zsize) + ...
    Cay(2:ysize,1:xsize,2:zsize).*(Hz(2:ysize,1:xsize,2:zsize)-Hz(1:ysize-1,1:xsize,2:zsize)) + ...
    Caz(2:ysize,1:xsize,2:zsize).*(Hy(2:ysize,1:xsize,1:zsize-1)-Hy(2:ysize,1:xsize,2:zsize));

Ey(1:ysize,2:xsize,2:zsize) = Ey(1:ysize,2:xsize,2:zsize) + ...
    Caz(1:ysize,2:xsize,2:zsize).*(Hx(1:ysize,2:xsize,2:zsize)-Hx(1:ysize,2:xsize,1:zsize-1)) + ...
    Cax(1:ysize,2:xsize,2:zsize).*(Hz(1:ysize,1:xsize-1,2:zsize)-Hz(1:ysize,2:xsize,2:zsize));

Ez(2:ysize,2:xsize,1:zsize) = Ez(2:ysize,2:xsize,1:zsize) + ...
    Cax(2:ysize,2:xsize,1:zsize).*(Hy(2:ysize,2:xsize,1:zsize)-Hy(2:ysize,1:xsize-1,1:zsize)) + ...
    Cay(2:ysize,2:xsize,1:zsize).*(Hx(1:ysize-1,2:xsize,1:zsize)-Hx(2:ysize,2:xsize,1:zsize));

% Liao abc
Ey(:,1,:) = 3 * EyL0(:,2,:) - 3 * EyL1(:,3,:) + EyL2(:,4,:);
Ez(:,1,:) = 3 * EzL0(:,2,:) - 3 * EzL1(:,3,:) + EzL2(:,4,:);
Ey(:,xsize+1,:) = 3 * EyR0(:,3,:) - 3 * EyR1(:,2,:) + EyR2(:,1,:);
Ez(:,xsize+1,:) = 3 * EzR0(:,3,:) - 3 * EzR1(:,2,:) + EzR2(:,1,:);
Ex(1,,:) = 3 * ExF0(2,,:) - 3 * ExF1(3,,:) + ExF2(4,,:);
Ez(1,,:) = 3 * EzF0(2,,:) - 3 * EzF1(3,,:) + EzF2(4,,:);
Ex(ysize+1,,:) = 3 * ExB0(3,,:) - 3 * ExB1(2,,:) + ExB2(1,,:);
Ez(ysize+1,,:) = 3 * EzB0(3,,:) - 3 * EzB1(2,,:) + EzB2(1,,:);
Ex(:,zsize+1) = 3 * ExT0(:,zsize) - 3 * ExT1(:,zsize-1) + ExT2(:,zsize-2);
Ey(:,zsize+1) = 3 * EyT0(:,zsize) - 3 * EyT1(:,zsize-1) + EyT2(:,zsize-2);
Ex(:,1) = 3 * ExBo0(:,1) - 3 * ExBo1(:,2) + ExBo2(:,3);
Ey(:,1) = 3 * EyBo0(:,1) - 3 * EyBo1(:,2) + EyBo2(:,3);

% Metal parts are thought as PEC. PEC boundary condition requires the
% tangential electric field components to vanish at the edge of the PEC.
% Electric field is zero inside the PEC.
% Antenna element
Ex(mLF:mLB+1,mLL:mLR,antz) = 0;
Ey(mLF:mLB,mLL:mLR+1,antz) = 0;
% Microstrip line
Ex(1:26,58:63,msz) = 0;
Ey(1:25,58:64,msz) = 0;
% Ground plane, aperture left open
Ex(:,1:49,gndz) = 0;
Ex(:,72:end,gndz) = 0;
Ex(1:20,.,gndz) = 0;
Ex(23:end,.,gndz) = 0;
Ex(1:21,54:67,gndz) = 0;
Ex(22:end,54:67,gndz) = 0;
Ey(:,1:50,gndz) = 0;
Ey(:,72:end,gndz) = 0;
Ey(1:19,.,gndz) = 0;
Ey(23:end,.,gndz) = 0;
Ey(1:20,54:68,gndz) = 0;

```

```

Ey(22:end,54:68,gndz) = 0;
% Inner conductor of a coaxial waveguide
Ex(dem, 58:63, msz-1:msz+1) = 0;
Ez(dem, 58:64, msz-1:msz) = 0;
% Outer conductor of a coaxial waveguide
Ex(dem, 57:64, msz-2) = 0;
Ex(dem, 57:64, msz+2) = 0;
Ez(dem, 57, msz-2:msz+1) = 0;
Ez(dem, 65, msz-2:msz+1) = 0;

% Illustration of coaxial waveguide to microstrip line transition
% ic = inner conductor, oc = outer conductor
%
% gndz -----
%      |  -----  |
% msz  |  |--ms--|  |
%      |  -----ic |
%      |  -----oc |
%
% -- = PEC

% Electric field in 3D is excited by last voltage component in 1D
% Field is directed from inner to outer conductor
Ex(dem,64,msz) = U(Usiz)/dx;
Ez(dem,61,msz+1) = U(Usiz)/dz;
Ex(dem,57,msz) = -U(Usiz)/dx;
Ez(dem,61,msz-2) = -U(Usiz)/dz;

%%%%%%%%%%%%%%%%%%%%%%%%%%%%%%%%%%%%%%%%%%%%%%%%%%%%%%%%%%%%%%%%%%%%%%%%

if mod(t,5) == 0,
    % S11-parameters are stored in a matrix:
    s_param = [(f./1e9)' (20*log10(abs(Uref./Uinc)))' ...
              (angle(Uref./Uinc)*180/pi)'];
    plot(f/1e9,s_param(:,2));
    fprintf(' Time: %d\n ', t);
    pause(0.5);
end
end

% ----- Time-stepping-loop ends -----%

% Antennas impedance
Z_ant = (((1 + Uref./Uinc)./(1 - Uref./Uinc)) * Z0)';

save ms_fed_patch s_param Z_ant;
clear;

```